DOI: 10.1002/ ((please add manuscript number))
Article type: (Review)

Recent Progress and Challenges Towards Highly Stable Nonfullerene Acceptor-Based Organic Solar Cells

Yiwen Wang, Jinho Lee, Xueyan Hou, Chiara Labanti, Jun Yan, Eva Mazzolini, Amber Parhar, Jenny Nelson, Ji-Seon Kim and Zhe Li**

Dr. Yiwen Wang, Dr. Xueyan Hou, Eva Mazzolini, Dr. Zhe Li
School of Engineering and Materials Science,
Queen Mary University of London, E1 4NS, London, United Kingdom.
E-mail: zhe.li@qmul.ac.uk

Dr. Jinho Lee
Max-Planck-Institut für Kohlenforschung,
Kaiser-Wilhelm-Platz 1, 45470, Mülheim an der Ruhr, Germany

Dr. Jinho Lee, Chiara Labanti, Amber Parhar, Prof. Ji-Seon Kim
Department of Physics and Center for Processable Electronics,
Imperial College London, London, SW7 2AZ, London, United Kingdom
E-mail: ji-seon.kim@imperial.ac.uk

Dr. Jun Yan and Prof. Jenny Nelson
Department of Physics and Center for Processable Electronics,
Imperial College London, SW7 2AZ, London, United Kingdom.

Keywords: Nonfullerene solar cells, organic photovoltaics, stability, molecular design, device engineering, ISOS standards

Organic solar cells (OSCs) based on nonfullerene acceptors (NFAs) have made significant breakthrough in their device performance, now achieving a power conversion efficiency of ~18% for single junction devices, driven by the rapid development in their molecular design and device engineering in recent years. However, achieving long-term stability remains a major challenge to overcome for their commercialization, due significantly to the current lack of understanding of their degradation mechanisms as well as the design rules for enhancing their stability. In this review, we focus specifically on the recent progress on understanding the degradation mechanisms and enhancing the stability of high performance NFA-based OSCs. We first provide an overview of the recent advances in the molecular design and device engineering of several classes of high performance NFA-based OSCs for various targeted applications, before presenting a critical review of the different degradation mechanisms identified through photochemical-, photo-, and morphological degradation pathways. Potential strategies to address these degradation mechanisms for further stability enhancement, from molecular design, interfacial engineering and morphology control perspectives, are also discussed. Finally, an outlook will be given highlighting the remaining key challenges toward achieving the long-term stability of NFA-OSCs.

1. Introduction

As one of the most promising next generation photovoltaic (PV) technologies, organic solar cells (OSCs) have attracted enormous attention over the past two decades. OSCs, which are based on organic molecular semiconductors, possess a number of key advantages compared to their inorganic counterparts (e.g. silicon, GaAs), including good band-gap tunability, ease of processing, low-cost, lightweight and mechanical flexibility[1–3]. These advantages have established OSCs as a highly versatile photovoltaic technology, enabling a range of new target applications such as building integrated PV, vehicle integrated PV, power-generating windows and self-powered electronics.

Compared to their inorganic counterparts, organic semiconductors often possess low dielectric constant (~4), resulting in tightly bound excitons with a strong coulomb binding energy of ~0.5-1eV[4]. To overcome this problem, efficient OSCs often utilize the so-called bulk heterojunction (BHJ) configuration in their photoactive layers[5] that contains a mixture of electron-donating (donor) and electron-accepting (acceptor) molecules to form a nanoscale blend morphology, which not only provides a sufficient driving force for excitons dissociation, but also percolated pathways for efficient charge transport and extraction while avoiding excessive charge recombination.

Fullerenes and their derivatives have been widely used as electron acceptors and played an important role in development of OSCs in the past 20 years. Their three-dimensional molecular structures make them suitable materials for BHJ structures, while their delocalized lowest unoccupied molecular orbital (LUMO) electronic structure leads to high electron mobility. Upon blending with donor molecules such as compatible conjugated polymers, they can form effective percolation critical for high-efficiency OSC devices.[6–8] However, fullerene acceptor-based organic solar cells encounter a limited efficiency due to a number of limitations of fullerene acceptors. Fullerene acceptors have a weak absorption especially in the ultraviolet visible and near-infrared spectrum due to their highly symmetrical chemical structure and poor synthetic flexibility, which greatly limits the photocurrent generation of fullerene acceptor-OSCs. Moreover, the energy levels of fullerenes are relatively fixed and difficult to alter, reducing their potential to operate well with energetically different donor polymers. In addition, some studies have shown that a number of degradation mechanisms of fullerene acceptor-OSCs under various environmental conditions are related to the high sensitivity of fullerene acceptors to light and oxygen, as well as their tendency to form detrimental macroscopic aggregates under thermal stress[9,10]. Therefore, there has been a strong need for alternative electron acceptor materials to improve OSC performance (efficiency and stability) further and hence to exploit the commercialization potential of OSCs.

Organic nonfullerene acceptors (NFA), in the form of small molecules, have recently been developed to overcome these limitations of fullerene acceptors. The greater synthetic flexibility allows for excellent tunability of their electron affinity and bandgap, offering great potential in the design of efficient OSCs for different targeted applications such as high-performance indoor organic photovoltaic[11–13] and semitransparent devices with high transmission[14,15] through optimization of their absorption spectra. This new molecular energy level engineering also promotes vigorous research efforts in the development of matching polymer donors for NFAs, which is an equally important consideration towards high performance nonfullerene OSCs.[16–

18] For example, complementary absorption and morphology control are both crucial for achieving efficient charge generation and separation processes, while adjustment of their molecular orbital energetics enables the development of OSCs with high open-circuit voltages and minimal voltage losses.[19,20] Due to the rapid development in their molecular design and device engineering over the past few years, NFA-based OSCs have made a breakthrough in achieving high power conversion efficiency (PCE) currently exceeding almost ~18% in single junction NFA-based OSCs, [21] already significantly surpassing those based on fullerene acceptors.

The emergence of new NFA materials is exciting, however most of the synthetic efforts have been made on achieving high device efficiency, with relatively little attention being paid to understanding their degradation mechanisms and enhancing their stability, thereby still limiting their commercialization potential. In this review, we focus specifically on the recent progress on understanding the degradation mechanisms and enhancing the stability of NFA-OSCs. We first provide a summary of the recent advances in the molecular design of NFA, in particular three main families (ITIC, IDTBR, and Y6) showing high OSC performance, followed by summarizing the recent development of new device structures including interfacial engineering, and the development of NFA for other targeted applications; We then provide a critical review of the different degradation mechanisms identified for NFA-based OSCs, including photochemical-, photo-, and morphological-stability, followed by in-depth discussions on the potential strategies to address these degradation mechanisms for further stability enhancement, from of molecular design, interfacial engineering and morphology control perspectives. In the end, we provide an outlook of the remaining key challenges toward achieving the long-term stability of NFA-OSCs.

2. Recent Progress in Device Performance

In this section, we summarize the recent progress in the development of high performance NFA-based OSCs for various targeted applications. We stress in particular the extensive research activities dedicated to the optimization of their materials and device design resulting in rapid advances in the performance of several classes of NFA-based OSC systems, thus highlighting the urgent need to understand their degradation mechanisms and improve their long-term stability, on the other hand, in order to substantially enhance their commercialization potential.

2.1. Molecular design of nonfullerene acceptors for high-performing OSCs

The molecular design of NFA have played a critical role in driving the rapid efficiency enhancement of NFA-based OSCs. Compared to fullerenes, the synthetic flexibility of NFAs offers a greater potential in further optimization of their optical (optical bandgap, absorption strength and spectral range), energetic (LUMO and HOMO energy levels) and structural properties (tendency to crystallise, molecular packing) for various target applications through further adjustment of their molecular structures. Sections 2.1.1-2.1.3 recapitulate the recent development in the molecular design of three classes of NFA, namely ITIC, IDTBR and Y6 families.

2.1.1. ITIC family

In 2015, Lin et al. reported high performance OSCs based on a nonfullerene electron acceptor ITIC (**Figure 1**), achieving power conversion efficiencies rivalling those based on fullerenes acceptors. This acceptor-donor-acceptor (A-D-A) structured nonfullerene acceptor (NFA) has a rigid center indacenodithieno[3,2-b]thiophene (IDTT) as electron-donating unit, end-capped with two electron-deficient 2-(3-oxo-2,3-dihydroinden-1-ylidene)malononitrile (INCN) groups. The push-pull structure of ITIC facilitates intramolecular charge transfer (ICT) between IDTT and INCN, resulting in a broad and strong absorption of ITIC in the region of 500-800 nm, peaking at 702 nm. The highest occupied molecular orbital (HOMO) and lowest unoccupied molecular orbital (LUMO) energy levels of ITIC films were estimated to be -5.48 and -3.83 eV respectively, with a narrow optical bandgap (E_g^{opt}) of 1.59 eV. The ideal energetic, optical and electrical properties of ITIC result in a device PCE of 6.58% in blend with poly[4,8-bis(5-(2-ethylhexyl)thiophen-2-yl)benzo[1,2-b;4,5-b']dithiophene-2,6-diyl-alt-(4-(2-ethylhexyl)-3-fluorothieno[3,4-b]thiophene-)-2-carboxylate-2-6-diyl)] (PTB7-Th) as the donor polymer, comparable to its fullerene based counterpart (7.29%).[22] After that, several high performance OSCs based on the ITIC NFA have been reported. Gao et al. reported an ITIC-based OSC using benzodithiophene–alt–fluorobenzotriazole copolymer (J51) as an electron donor, which exhibits an improved PCE of 9.07% with a V_{OC} of 0.81 V, a J_{SC} of 16.33 mA/cm^2 and FF of 68%. Such improved device performance was attributed to the complementary absorption of the donor and acceptor, suitable energy levels, optimal nanoscale-phase-separated interpenetrating network and balanced electron and hole mobilities of the photoactive layer.[23] Qin et al. demonstrated a poly[(4,4'-bis(2-butyloctoxycarbonyl-[2,2'-bithiophene]-5,5-diyl)-alt-(2,2'-bithiophene-5,5'-diyl)] (PDCBT):ITIC-based OSC obtaining a PCE of 10.05% with a V_{OC} of 0.94 V, J_{SC} of 16.50 mA/cm^2 and FF of 65.57%.[24], owing to the complementary absorption of PDCBT in the short-wavelength region (400-650 nm) with a deep HOMO energy level of -5.31 eV, in conjunction with an optimized nanoscale morphology of photoactive layer. Zhao et al. demonstrated a poly[(2,6-(4,8-bis(5-(2-ethylhexyl)thiophen-2-yl)-benzo[1,2-b:4,5-b']dithiophene))-alt-(5,5-(1',3'-di-2-thienyl-5',7'-bis(2-ethylhexyl)benzo[1',2'-c:4',5'-c']dithiophene-4,8-dione))] (PBDB-T): ITIC-based OSC achieving an average PCE of 10.68%, with a V_{OC} of 0.90V, J_{SC} of 16.73 mA/cm^2 and FF of 70.8%, attributing to the broad absorption and well matched energy levels of the PBDB-T:ITIC blend.[25] To further increase the V_{OC} of nonfullerene OSCs, Bin et al. decreased the HOMO energy levels of the NFA by introducing trialkylsilyl substituents on the bithienyl-benzodithiophene (BDTT) unit of the 2D- conjugated D-A copolymer based on the BDTT donor unit and fluorine-substituted benzotriazole (FBTA) acceptor unit. The HOMO energy level of the synthesized donor J71 was decreased to -5.40 eV and its absorption extinction coefficient was enhanced due to the interaction between σ* (Si)–π*(C) bond and the trialkylsilyl substitution, resulting in a higher V_{OC} of 0.94 V with a J_{SC} of 17.40 mA/cm^2, achieving a PCE of 11.2% for J71:ITIC-based OSCs.[26] Xu et al. developed a wide-bandgap (over 2.07 eV) donor poly(2-(5-(4,8-bis(5-((2-butyloctyl)thio)thiophen-2-yl)benzo[1,2-b:4,5-b']dithiophen-2-yl)-4-octylthiophen-2-yl)-5-(4-octylthiophen-2-yl)-1,3,4-thiadiazole) (PBDTS-TDZ) with a HOMO energy level of -5.39 eV, which matches well with the narrow-bandgap ITIC acceptor, resulting in strongly complementary light absorption of the donor and acceptor in the region of 300-800 nm. The resulting PBDTS-TDZ:ITIC-based OSCs exhibit a high V_{OC} of 1.10 V and a small energy loss (E_{loss}) of 0.48 eV, with a J_{SC} of 17.78 mA/cm^2 and a device PCE of 12.35%.[27]

The HOMO and LUMO energy levels and the absorption spectra of the ITIC-based NFA can be effectively adjusted through alterations of their molecular structure. ITIC has a high HOMO energy level of -5.48 eV, which does not match well with wide-bandgap donors with HOMO energy levels deeper than -5.4 eV such as PDBT-T1 due to a small HOMO energy offset. Besides, the electron mobility of ITIC (2.6×10^{-4} cm^2 V^{-1} s^{-1}) is still lower than that of fullerene acceptors (10^{-3} cm^2 V^{-1} s^{-1}), which requires further improvement.[28] Lin et al. developed the ITIC-Th (**Figure 1**) NFA by replacing the phenyl side chains with thienyl side chains. ITIC-Th exhibits lower LUMO (-3.93 eV) and HOMO (-5.66) energy levels compared to ITIC, which match well both with the narrow-bandgap donor PTB7-Th (E_g=1.58 eV) and wide-bandgap donor PDBT-T1(E_g^{opt}=1.85 eV), resulting in a PCE of 8.5% and 9.3% respectively. The introduction of phenyl side chains increases the intramolecular interaction, results in an enhanced electron mobility of 6.1×10^{-4} cm^2 V^{-1} s^{-1} and facilitates the π-π stacking and charge transport in ITIC-Th.[28] Yang et al. synthesized the m-ITIC (**Figure 1**) NFA through further manipulation of the side chains of ITIC with meta-alkyl-phenyl substitution. The change of side-chain position results in little effect on the HOMO (-3.82 eV) and LUMO (-5.52 eV) energy levels but improves the self-organization and crystallinity, resulting in enhanced electron mobility and stronger light absorption than ITIC. As a result, a higher PCE of 11.49% was obtained for the 2D-conjugated benzodithiophenealt-fluorobenzotriazole copolymer with alkylthio side-chain (J61):m-ITIC-based OSCs with a V_{OC} of 0.902 V, J_{SC} of 18.31 mA/cm^2 and FF of 69.55%, compared to a PCE of 10.57% of corresponding J61:ITIC-based OSCs.[29] ITIC has an A-D-A molecular structure, where the electron transport property is determined by the stacking of electron-deficient end groups which provide the main electron transport channels.[30] It was also found that the electron density of the LUMO energy level is distributed throughout the end groups, while the electron density distribution of the HOMO is mainly located on the central donor unit.[30,31] Therefore, many research groups have focused on the end group engineering of the ITIC molecular structure in order to further adjust its LUMO energy level and therefore enhance device efficiency. Yao et al. developed a new NFA, namely ITCC (**Figure 1**), by introducing thienyl-fused indanone as end groups on ITIC. The LUMO energy level of ITCC is elevated to -3.76 eV, resulting in a high V_{OC} of 1.01 V. Besides, ITCC shows a closer π–π stacking distance and a higher electron mobility (9.26×10^{-4} cm^2 V^{-1} s^{-1}) compared to ITIC, and a PCE of 11.0% was obtained by blending with the PBDB-T donor polymer.[30] Li et al. developed a new NFA, namely IT-M, by introducing one methyl group to the end group of ITIC **(Figure 1)**, lifting the LUMO energy level (-3.35) by 0.06 eV than ITIC (-3.41). PBDB-T:IT-M-based OSCs exhibit a PCE of 11.48% with a V_{OC} of 0.94 V, J_{SC} of 16.75 mA/cm^2 and an FF of 73.5%, compared to PBDB-T:ITIC-based OSCs which have a PCE of 10.68% with a V_{OC} of 0.90 V.[31] Apart from the modification of the molecular energy levels, the adjustment of intramolecular electron push-pull effect by introducing electron pushing or drawing groups into the end groups of ITIC can also enhance the photovoltaic performance. Li et al. synthesized a new NFA, namely IT-4F (**Figure 1**), by introducing fluorine atoms into the end groups of ITIC, which results in enhanced intramolecular electron effect in IT-4F compared to ITIC. IT-4F exhibits an optimal miscibility with the donor polymer poly[(2,6-(4,8-bis(5-(2-ethylhexyl-3-fluoro)thiophen-2-yl)-benzo[1,2-b:4,5-b']dithiophene))-alt-(5,5-(1',3'-di-2-thienyl-5',7'-bis(2-ethylhexyl)benzo[1',2'-c:4',5'-c']dithiophene-4,8-dione)] (PBDB-TF/PM6), resulting in a high FF of 75% in PM6:IT-4F OSCs due to a high domain purity. The enhanced ICT effect causes red-shifted absorption spectrum of IT-4F with a low E_{gap}=1.50 eV, achieving a PCE of 13.3% in conjunction with a high J_{SC} (20.39 mA/cm^2) of PM6:IT-4F-based OSC.[32]

2.1.2. IDTBR family

In 2016, Holliday et al [33]reported a new family of A-D-A structured nonfullerene acceptors based on the previously developed 5,5′-[(9,9-Dioctyl-9H-fluorene-2,7-diyl)bis(2,1,3-benzothiadiazole-7,4-diylmethylidyne)]bis[3-ethyl-2-thioxo-4-thiazolidinone] (FBR) NFA[34]. Despite the promising PCE achieved by the poly(3-hexylthiophene) (P3HT):FBR blend system, the spectral overlap of FBR with P3HT, as well as the high recombination rates due to its suboptimal blend morphology, has significantly limited photocurrent. The IDTBR family NFA were designed to be spectrally complementary to P3HT with an A2=A1-D-A1=A2 molecular structure with two different acceptor units (A1, benzothiaziadole and A2, rhodanine), and an indacenodithiophene core, replacing the fluorene core of FBR. Two of the widely established IDTBR family NFA, named EH-IDTBR and O-IDTBR (**Figure 2**), were developed using branched 2-ethylhexyl chains and n-octyl chains in the alkylated core respectively. Compared to FBR, IDTBR has a planar molecular structure, which results in increased conjugation. This effect, in conjunction with the electron-rich thiophene core, leads to a raised HOMO energy level with a red-shift in the absorption spectrum of IDTBR. The HOMO/LUMO levels for O-IDTBR and EH-IDTBR are -5.51/-3.88 eV and -5.58/-3.90 eV respectively, both exhibiting significantly enhanced light absorption than PCBM, with absorption maxima at 650 nm. The n-octyl chains allow for a more crystalline structure in O-IDTBR with a red shift in the absorption spectrum than EH-IDTBR, further reflected by the EQE spectra of the devices presented in this study[33]. Promising PCE values of 6.3% and 6% were obtained for lab-scale OSCs based on P3HT:O-IDTBR and P3HT:EH-IDTBR respectively. Recently, An et al [35] reported a PCE of 7.1%, with a V_{OC} of 0.73 V, J_{SC} of 12.91 mA/cm^{2}and FF of 75.09% for P3HT:O-IDTBR devices using the non-halogenated solvent o-MA/1-MN. Badgujar et al. [36] reported a device PCE of 7.09%, with a V_{OC} of 1.06 V, J_{SC} of 12.1 mA/cm^2 and FF of 55% based on the BDT3TR:O-IDTBR blend system, comparable to the BDT3TR:$PC_{70}BM$ blend system with a PCE of 7.14%, V_{OC} of 0.9 V, J_{SC} of 10.98 mA/cm^2 and FF of 70%. Cha et al.[37] performed a comparative study of the performance and stability of OSCs based on the PffBT4T-2OD:$PC_{71}BM$ and PffBT4T-2OD:EH-IDTBR blend systems, and found that the PffBT4T-2OD:EH-IDTBR device exhibit a comparable PCE of 9.5% to its fullerene counterpart (PCE~10.9%). Hu et al.[38] investigated the effect of low boiling point solvent additive processing upon the performance of OSCs based on the PTB7-Th:EH-IDTBR blend system, and achieved an efficiency of 10.81% and 11.36% using 1,1-dimethoxyethylbenzene (DMB) and 6-mercapto-1-hexanol (MHA) respectively.

2.1.3. Y6 family

In 2019, Yuan et al. reported a new class of NFA acceptor, namely Y6 (**Figure 3**), achieving a PCE of 15.7%. Different from ITIC and IDTBR family, the Y6 family of NFA acceptor has a A-DA′D-A structure, which is composed of a 2, 1, 3-benzothiadiazole (BT)-core-based central unit dithienothiophen[3.2-b]-pyrrolobenzothiadiazole (TPBT) and 2-(5,6-difluoro-3-oxo-2,3-dihydro-1H-inden-1-ylidene)malononitrile (2FIC) end units. The stronger electron-deficient BT is used as the central core and thienothiophene (TT) is used as the end group of the central fused ring in order to enhance the electron mobility and broaden the light absorption. Alkyl side chains on the nitrogen atoms in the central core of Y6 at the same side are used to prevent over aggregation of molecules and maintain intramolecular contact for efficient charge transport. The use of 2FIC flanking units enhances absorption and promotes intermolecular interactions and thereby facilitates charge transport. The absorption spectrum of Y6 films reaches maximum at around 810 nm, which further extends to 1100 nm corresponding to the near infrared region with a low optical E_{gap} of 1.33 eV. The HOMO and LUMO energy levels of Y6 were estimated to be–5.65 eV and –4.10 eV respectively. By blending with the medium-bandgap (E_g^{opt}=1.81 eV) polymer donor PM6, which has a complementary absorption with Y6, a PCE of 15.6% have been achieved with a V_{OC} of 0.83 V, J_{SC} of 25.3 mA/cm^2 and FF of 74.8%.[39] Jiang et al. and Luo et al. optimized the branching position of the alkyl chains on the pyrrole motif in Y6 by replacing the 2nd-position branched alkyl chain with a 3rd-position branched alkyl chains on the pyrrole motif and synthesized the N3 or Y6-C2 acceptor (**Figure 3**). The change in branching position of the alkyl-side-chain has little effect on the optical and electrochemical properties of the acceptor with similar absorption spectra and energy levels, but results in better packing, improved crystallinity and therefore better charge transport property with an enhanced electron mobility of 3.94×10^{-4} cm^2 V^{-1} s^{-1} of N3 compared to Y6 (3.12×10^{-4} cm^2 V^{-1} s^{-1}). As a result, PM6:N3 based OSCs achieved a higher PCE of 15.79% compared to PM6:Y6 (15.04%), with the highly ordered structure, better crystallization characteristics, longer carrier drift length and a more balanced electron/hole mobility (μ_e/μ_h=1) in the PM6:N3 blend system.[40,41]

Halogenation of the electron accepting units can further enhance the ICT effects and reduce the bandgap of NFA.[42,43] Cui et al. reported a chlorinated low bandgap acceptor BTP-4Cl (**Figure 3**) by replacing the fluorine atoms in Y6 with chlorine atoms. The HOMO and LUMO energy levels of BTP-4Cl are downshifted from −5.60 to −5.65 eV and −3.55 to −3.63 eV respectively, resulting in a redshift of 20 nm in optical absorption of BTP-4Cl compared to Y6. Although the BTP-4Cl shows a lower LUMO level, a PCE of 16.1% with a higher V_{OC} of 0.87 V was obtained for PM6:BTP-4Cl-based OSCs compared to their Y6-based counterpart (0.83 V), which is attributed to a low non-radiation energy loss (0.206 eV) in PM6:BTP-4Cl based OSCs.[19] Cui et al. further conducted side-chain engineering of the BTP-4Cl NFA, replacing the alkyl side chains (2-ethylhexyl) with the longer side chain 2-butyloctyl, forming a new NFA BTP-4Cl-12 (**Figure 3**). BTP-4Cl-12 exhibit balanced solution processability and aggregation, resulting in a PCE of 16.6% based on Y6:BTP-4Cl-12 OSCs due to an optimal blend morphology favoring efficient transport of the charge carriers.[44] In addition to the central alkyl chains on nitrogen atoms, there are also two alkyl chains with electron carbon atoms on the edge of the bithiophene units. Cui et al. shortened the n-undecyl (C11) to n-nonyl (C9) on the edge of BTP-4Cl-BO where the alkyl chains of EH on the pyrrole rings was replaced with 2-bultyloctyl (BO), forming the BTP-eC9 (**Figure 3**) NFA which exhibits suitable solubility and enhanced intermolecular ordering. The resulting PM6:BTP-eC9-based device yielded an out-performing PCE of 17.4%, due to an optimal blend morphology which favors efficient transport and suppressed recombination of charge carriers.[45] Despite the outstanding device performance achieved for Y6-based OSCs, there is only a limited range of donor polymers matching the low-bandgap Y6 and its derivatives. Recently, Liu et al. reported a wide bandgap polymer D18, which has a deep HOMO energy level (-5.51 eV) with strong electron-withdrawing capability and large molecular planes. D18 exhibits an enhanced hole mobility of 1.59×10^{-3} cm^2 V^{-1} s^{-1} and a balanced charge carrier transport (μ_e/μ_h=1.06) in blend with Y6, resulting a record PCE of 17.67% with a V_{OC} of 0.97 V, J_{SC} of 27.31mA/$cm^2$and FF of 75.5%.[21]

2.2. NFA for unconventional targeted applications

2.2.1. High-performance indoor organic photovoltaics

Recently, indoor organic photovoltaics have attracted much attention due to their capability in powering small electronic devices and sensors, especially driven by the rapid development of the Internet of Things (IoT), whose components such as indoor sensors, micro-controllers and communication modules usually require self-sustained power suppliers. The absorption spectra of organic semiconductors can be facilely adjusted by altering their molecular structure, offering great potential in matching their absorption with the emission spectra of various indoor light sources such as light-emitting diodes (LEDs) and fluorescent lamps (FL) in a typical range of 400 ~ 750 nm. Compared with fullerene acceptors with limited light absorption in the visible region, the synthetic flexibility of NFA offers outstanding potential in modulating optical bandgap and molecular energy levels to maximize light absorption and V_{OC}, which is necessary to achieve high-performing indoor organic photovoltaics.[46,47] Dayneko et al. developed a twisted N-annulated perylene diimide dimer (tPDI$_2$N-EH) (**Figure 4**), which exhibits enhanced optical absorption in the region of 400 ~ 600 nm. When blended with a polymer donor (PPDT2FBT), whose absorption is strongly complementary to that of tPDI$_2$N-EH, the resulting organic photovoltaics exhibited a PCE of 10.2% under warm white LED illumination at 10000 lx, with an absorption range from 400 to 700 nm that overlaps well with the spectrum of the indoor light source.[48] Ding et al. demonstrated an all-polymer organic photovoltaics containing a polymer acceptor PBN-10 (**Figure 4**) with E_g^{opt} of 1.95 eV and a polymer donor CD1 with E_g^{opt} of 1.93 eV. The boron–nitrogen coordination bonds (B←N) in PBN-10 facilitate a medium bandgap with tunable LUMO and HOMO energy levels, resulting in a high V_{OC} of 1.14V and an average PCE of 25.2% under FL at 1000 lx .[49] Cui et al. fabricated an organic photovoltaics with a wide-bandgap NFA ITCC and donor polymer PM6 in order to maximize the overlap between the absorption spectra of the device with the emission spectrum of the indoor light source while still maintaining a high V_{OC}. The resulting PM6:ITCC-based device achieved an PCE of 22.0% with a V_{OC} of 0.962 V under 1000 lx LED illumination.[12] Later, Cui et al. designed an A-D-A structured NFA IO-4Cl (**Figure 4**) with E_g^{opt} of 1.80 eV, with a strong absorption spectrum ranging from 450 to 700 nm. A 1 cm^2 PM6:IO-4Cl-based device was fabricated, achieving an outstanding PCE of 26.1% with a high V_{OC} of 1.10 V under a white LED lamp at 1000 lx, owing to well-matched absorption spectrum with the indoor light source in conjunction with a low energy loss of less than below 0.6 eV. [11]

2.2.2 High-performance semitransparent OSCs

Another unique characteristic of OSCs is their potential to achieve semitransparency, which has significant prospects in Building Integrated Photovoltaics (BIPV) applications, such as power-generating windows, curtains, architectural and fashion applications. A major challenge for semitransparent OSCs (ST-OSCs) is to simultaneously achieve high device performance and high average visible transmittance (AVT). It was proposed that an ideal active layer for high-performance ST-OSCs should exhibit strong near infrared (NIR) absorption but weak absorption of visible light.[15] NFA can achieve an extended absorption in the NIR region compared to fullerene acceptors due to the ICT effect from the electron-donating moiety to the electron-deficient groups~~, and it has been demonstrated that the enhanced ICT can significantly extend the absorption spectra of the materials in the NIR region~~,[14] thereby possessing great potential in obtaining semitransparent OSCs with high performance. Wang et al. designed a NIR NFA, namely IHIC (**Figure 4**), which has a A-D-A molecular structure based on the strong electron-donating group dithienocyclopentathieno[3,2-b]thiophene end-capped with the strong electron-withdrawing unit INCN to enhance the ICT effect, resulting in a high extinction coefficient of $1.6 \times 10^5 \mathrm{M}^{-1}\mathrm{cm}^{-1}$ in the absorption range of 600–900 nm with a narrow $\mathrm{E_g^{opt}}$ of 1.38 eV. ~~By blending with the narrow-bandgap donor PTB7-Th which has a strong absorption in 500-800 nm, the active layer shows an absorption peak at 710 nm with a weak absorption in the region of 400–600 nm, which is most sensitive to human eyes.~~ The resulting IHIC-based ST-OSCs achieved a relatively high PCE of 9.77% with a high AVT of 36%.[15] Cui et al. incorporated chlorination into the IEICO NFA to enhance the ICT effect and obtained an ultranarrow-bandgap (E_g^{opt}=1.23 eV) NFA IEICO-4Cl (**Figure 4**), which mains absorption in the range of 745–945 nm with very weak absorption in the region of 370–740 nm. ~~The color of IEICO-4Cl-based active layer can be tuned to cyan, blue and purple by using different donors such as PTB7-Th, PBDB-T and J52.~~ A ST-OSC based on PTB7-Th:IEICO-4Cl was fabricated, reaching a PCE of 8.38% with AVT of 25.6%.[50] Li et al. demonstrated a NFA BT-CIC (**Figure 4**) by introducing chlorine atoms into BT-IC at 5,6-positions of the 2-(3-oxo-2,3-dihydroinden-1-ylidene)-malononitrile. The introduction of Cl atoms effectively lowers the energy gap by enhancing the ICT effect, leading to a red-shift of 60 nm in absorption spectrum compared to BT-IC. The PTB7-Th:BT-CIC-based ST-OSCs show a PCE of 7.1% with AVT of around 43% from 400 to 650 nm.[51] Besides, many ultranarrow-bandgap NFA with E_g^{opt} of around 1.32 eV have been reported, such as FOIC,[52] ATT-2,[53] and ACS8[54] (**Figure 4**), which show strong absorption in the range of 600-950 nm. The FOIC, ATT-2 and ACS8-based ST-OSCs exhibit PCEs of 10.3%, 7.7% and 10.4% respectively in blend with the PTB7-Th donor polymer, with AVT of around 37%.

2.3. Device Engineering of NFA OSCs

In this section, we summarize the recent progress in the optimization of device design to enable the demonstration of high performance NFA-based OSCs. We cover in particular the recent development of novel device interlayers and structures with good compatibility with NFA-based OSC systems, including several classes of emerging interlayers, as well as new device structures including ternary blend, tandem, integrated and printed large area devices.

2.3.1. Interlayers

In addition to the molecular design of photoactive materials, the development of interlayer has been considered as a significant research area to achieve high device performance and stability in OSCs.[55–57] Interface engineering – the means of optimizing interfacial properties – is typically implemented by introducing interlayers between the photoactive layer and electrodes in OSC devices in which the photoactive layer is sandwiched between the anode and cathode.[58–60] The materials with electron transport (hole blocking) capability can be used as electron transport layer (ETL) whereas the materials with hole transport (electron blocking) capability can be used as hole transport layer (HTL). While the primary role of the interlayer is to endow the devices with charge selectivity, the chemical (or electrochemical) properties associated with the degradation induced by the external sources (e.g., oxygen and water) and chemical interaction with NFAs are also important prerequisites for stable OSCs.

Polyelectrolytes are polymers equipped with ionic functional groups at the side chain, which can be classified according to their backbone structure – nonconjugated and conjugated polyelectrolyte.[61,62] Due to the presence of polar ionic functionality, polyelectrolytes are soluble in polar solvents, such as alcohol and water, and insoluble in common organic solvents, thereby endowing orthogonal solubility with a photoactive layer. In addition, ionic pairs (i.e., cation and anion) of polyelectrolytes are self-assembled on electronic materials to form interfacial dipoles, which significantly modify the surface work function (WF) through vacuum level shift.[63,64] Such advantages together with room-temperature solution processability create opportunities for broad applications of polyelectrolytes as interlayers in organic electronics.

The amine-containing nonconjugated polyelectrolytes, polyethyleneimine (PEI) and ethoxylated PEI (PEIE) have been intensively investigated as ETLs due to their very high density of amine groups in its molecular structure, enabling a large degree of energy level tuning.[65,66] Notably, Zhou et al. first reported both PEI and PEIE providing a universal method to produce low surface WFs of various electronic materials, such as ITO, Au, Ag, Al, PEDOT:PSS, and graphene.[65] Due to the favorable energetic alignment for electron collection, the PEI and PEIE performed very well in the fullerene acceptor-based OSCs; however, these amine-based polyelectrolytes can chemically interact with NFA, which degrades the intramolecular charge transfer processes of the NFA molecules. A recent study reported that chemical reaction can occur between PEI (also PEIE) and ITIC molecules, which is also likely in part to be linked to the interfacial reaction caused by the PEDOT:PSS.[67–69] When PEI makes contact with ITIC, PEI can act as a nucleophile with the carbonyl (C=O) groups in INCN, causing the structural change of ITIC and breaking intramolecular π-electron overlap within the molecule (**Figure 5a**). The bleaching of the absorption peak and concomitant color change reflects the degradation of the electronic structure of ITIC. As a result, the devices with PEI ETL exhibited a PCE of 7.06%, which is inferior to the devices with zinc oxide (ZnO) ETL (9.71%).

To tackle this problem, a new approach to mitigating chemical reaction has been proposed, which is implemented by dissolving PEIE in aqueous solution.[70] The PEIE in aqueous solution showed a higher degree of protonation which tends to deactivate the chemical reaction between PEIE and IEICO-4F. In contrast, protic alcohol solvents such as isopropanol, ethanol, and methanol promote less protonation of PEIE, which might be attributed to their dielectric constants of 17.9 (isopropanol), 24.5 (ethanol), 32.7 (methanol), and 80.1 (water). The PTB7-Th:2,2'-[[4,4,9,9-Tetrakis(4-hexylphenyl)-4,9-dihydro-s-indaceno[1,2-b:5,6-b']dithiophene-2,7-diyl]bis[[4-[(2-ethylhexyl)oxy]-5,2-thiophenediyl]methylidyne(5,6-difluoro-3-oxo-1H-indene-2,1(3H)-diylidene)]]bis[propanedinitrile] (IEICO-4F) devices with isopropanol processed PEIE showed a PCE of 9.4% with a V_{OC} of 0.69 V, J_{SC} of 25.6 mA cm^{-2} and FF of 0.53. Interestingly, PEIE processed from aqueous solution enables high device performance, generating a PCE of 13.2% with a V_{OC} of 0.70, J_{SC} of 27.2 mA cm^{-2} and FF of 0.69. On the other hand, different from the simple polyelectrolyte approach, Huang et al. developed a cross-linkable block copolymer consisting of hydrophobic poly(n-butyl acrylate) block-hydrophilic poly(N-vinyl-1,2,4-triazole), which offers not only interfacial dipoles but also solvent/photo/thermal resistance.[71] The devices with block copolymer ETL produced a PCE of 8.03% and retained 80% of their performances under thermal stress of 60 °C of 1000 h or continuous 1 sun illumination for 1000 h, outperforming the devices with conventional ETL. Overall, these results suggest that cross-linked block copolymer can be used as a new ETL for realizing efficient and stable OSCs.

With respect to ease of processing, a major bottleneck in adopting polyelectrolyte-based interlayers for printable OSCs lies in the extremely high sensitivity of device performance to interlayer thickness.[72–86] In general, the optimal interlayer thickness is less than 10 nm, beyond which device performance will significantly deteriorate as the interlayer thickness is further increased, which is attributed to the insulating nature of nonconjugated polyelectrolytes. In contrast, conjugated polyelectrolytes (CPEs) are relatively free from this problem by providing good electron transporting capabilities. Indeed, depending on how the molecular structure is controlled, the electron mobility of CPEs can be greatly adjusted, which is beneficial for improving the compatibility with the printing process.

In 2014, Zhang et al. first demonstrated thickness-insensitive small-molecule-based ETLs.[73] The PDINO, which has a perylene diimides (PDI) central core and amino N-oxide terminal substituent, can be used as an ETL for efficient OSCs, as PDINO possesses high conductivity of ~10^{-5} S cm^{-1} and fine work function tuning capability. As a result, PTB7:$PC_{71}BM$ BHJ coupled with the PDINO ETL showed prominent PCEs as high as 8.05–8.24% within a wide range of the PDI-interlayer thickness (10–25 nm). The molecular structure of PDINO was further modified by performing amine group functionalization to the PDI derivative, namely PDINN, for use as an electron transport layer.[87] Compared to the PDINO, the secondary amine in the side chain of PDINN can provide enhanced dipole moment to generate lower WF and form hydrogen bonding with the photoactive materials, which helps to establish better electrical and physical contact between PDINN and photoactive layer. The introduction of PDINN into OSCs with PM6:Y6 supports a high PCE level of 17.23%. Recently, Sun et al. have developed a naphthalene diimide (NDI)-based water/alcohol soluble CPE (PFN-2TNDI) as a ETL.[76] Different from conventional polyelectrolyte ETLs such as poly[(9,9-bis(30-(N,N-dimethylamino)-propyl)-2,7-fluorene)-alt-2,7-(9,9-dioctylfluorene)] (PFN), PFN-2TNDI offered electron accepting capability, in which photoinduced electron transfer occurs at donor/PFN-2TNDI interfaces, confirmed by photoluminescence (PL) and charge modulated electro absorption spectroscopy. This is attributed to the electronic properties of NDI moiety. More importantly, the favorable energy level and self-doping effect of PFN-2TNDI facilitate efficient electron transport, enabling high device performance even with thick PFN-2TNDI ETL **(Figure 5b)**. First, PFN-2TNDI possesses deep LUMO levels that are deeper than those of NFA, which is beneficial for electron transport. However, the shallow LUMO level of PFN leads to a substantial energy barrier between PFN and NFA, which makes the PFN ETL more susceptible to thickness. Second, the self-doping effect of PFN-2TNDI greatly improves conductivity, reducing the sensitivity of OSC performance to thickness. As a result, using PBDB-T:ITIC, PCEs of 11.1% and 9.8% with 5 nm and 33 nm of PFN-2TNDI were achieved respectively, which is higher than that of PFN-based devices with a PCE of 8.6%. Given that NDI yields improved electron transport mobility, Kang et al. synthesized NDI-based small molecular electrolytes such as (N,N-dimethylamino) propyl NDI (NDI-N) and (N,N-dimethyl-N-ethylammonium)propyl NDI (NDI-Br), which exhibits additional advantage of high crystallinity, endowing ETL with enhanced electron transporting properties (**Figure 5c**).[77] The OSC performances with PM6:IT-4F blend were in turn significantly improved from 10.1% (methanol treatment) to 13.9% (NDI-N ETL) and 11.5% (NDI-Br ETL). Interestingly, with the incorporation of an NDI-N, the devices showed an excellent tolerance to thickness variation, producing 11.6% and 10.2% with 30 nm and 50 nm of NDI-N layers respectively. Further, by using a blade-coating method, large-area OSCs (1 cm^2) were successfully fabricated yielding a high PCE of 13.2%. OSCs whose performance is relatively insensitive to the ETL thickness offer higher compatibility with continuous printing processes, further allowing for more reliable device fabrication.

As another major field of ETL, important research progress has been made in the stability of OSCs using metal oxides. Jiang et al. suggested that the ZnO ETL can deteriorate the photoactive layer by causing a photocatalytic reaction under UV illumination, and showed that the use of SnO_2 can mitigate this problem.[88] When ZnO/IT-4F film was exposed to the AM 1.5 light, IT-4F molecule was decomposed by photocatalytic activity of ZnO, as evident from the observation of disappearance of the intramolecular charge transfer absorption band, whereas IT-4F with SnO_2 showed no distinguishable change in absorption spectra under same environmental conditions. This is because SnO_2 has a wider bandgap than that of ZnO, rendering it optically inactive to general solar irradiation.

In contrast to the ETL for electron selective contacts, electrolytes with hole selectivity (i.e., HTL) have also been developed.[89–97] The conducting polymer PEDOT:PSS is the most commonly used HTL due to its excellent hole selective and transporting properties. However, the inherent acidic and hygroscopic nature of PEDOT:PSS severely challenges the long-term stability of the devices. Motivated from the PEDOT:PSS, it was recently revealed that some weakly doped CPEs can be used as stable HTL in NFA OSCs. The partial oxidation of conjugated backbone induces the alteration of electronic structure and the formation of the molecular dipole that follows opposite direction to the n-type (pristine) counterparts, which brings about upward vacuum level shift, thereby affording p-type characteristics. The notable features of this system are broad WF tunability, orthogonal solvent processability, pH-neutrality, and homogeneous electrical conductivity, promoting their applications as an HTL for OSCs. Although many important studies have been reported on the use of CPE-based HTL in OSCs with fullerene acceptors, it is rare to find the cases where p-type CPE is applied to an NFA OSC. This is because recent donor polymers are designed to have a deep HOMO level to achieve high V_{OC}, which makes forming Ohmic contact for hole carriers more difficult. To address this issue, Cui et al. proposed a new approach to modulate the molecular energy level of anionic CPEs, PCP-x (x = H, Li, Na, K, Cs).[98] The WF tunability of PCP-x was determined by the type of the counter-ions: the self-doping effect can be enhanced as the size of counter-ion is decreased (**Figure 5d**). As a result, PCP-x CPEs shift the WF of the ITO from 4.78 to 5.11 eV by changing counter-ion from Cs to H, and the OSCs with PCP-H-modified anode exhibited the highest PCE of 12.8%, where a ploy[4-(5-(4,8-bis(5-(2-ethylhexyl)-4-fluorothiophen-2-yl)benzo[1,2-b:4,5-b′]dithiophen-2-yl)thiophen-2-yl)-5,6-difluoro-2-(2-hexyldecyl)-7-(thiophen-2-yl)-2H-benzo[d][1,2,3]triazole] (J52−2F):IT-4F functions as a photoactive layer. In addition to the side chain engineering on ionic groups, fluorination and ionic substitution on the PCP-Na produced PCP-2F-Li that further increased the WF of ITO from 4.86 to 5.0 eV, as compared to PCP-Na. Furthermore, fluorination reduces the absorption tails from 550 to 900 nm, where the photoactive layer main absorbs, which is beneficial for better photocurrent generation. As an extension of their research, using PCP-2F-Li and PBDB-TF:IT-4F as pH-neutral HTL and photoactive layer, respectively, highly efficient OSCs were demonstrated in both small and large-area (1 cm^2), yielding 12.7% and 10.6% respectively.[99] To achieve high efficiency in OSCs with p-type CPE-based HTL, synthetic strategies for the preparation of doped-polyelectrolytes with deeper HOMO levels and concurrently high hole transport capability were found to be important.

Recently, in addition to metal oxides, 2D materials have been actively studied as alternatives to overcome the disadvantages of PEDOT:PSS. Lin et al. proved for the first time that 2D transition metal disulfide, such as WS_2 and MoS_2, can be used as HTL of organic solar cells.[100] By adopting simple and cost-effective liquid exfoliation method, monolayer/bilayer flakes of WS_2 were formed, which provides good surface coverage of the ITO electrode. As a result, PEDOT:PSS-free OSCs of ITO/WS_2/PM6:Y6:$PC_{71}BM$/PFN-Br/Al exhibited a PCE of 17%. Analysis of the optical and recombination characteristics revealed that enhanced performance is most likely ascribed to the photonic structure and reduced bimolecular recombination losses in WS_2-based devices. These results suggest that 2D materials could be potential HTL for efficient and stable OSC applications.

2.3.2. Ternary OSCs with enhanced performance and stability

The OSCs beyond one pair of a donor-acceptor binary blend – so-called ternary blend – have emerged as a promising strategy to simultaneously improve device efficiency and stability. By integrating multiple donor or acceptor materials, light absorption bandwidth can be broadened, which is particularly important in OSCs because typical organic semiconductors exhibited intrinsically narrow absorption window. Although the construction of multi-junction type OSCs by stacking sub-cells with complementary absorption is an effective way to harvest broad solar spectrum, difficulties in processing of complicated structures have been a major obstacle that increases the complexity of device fabrication. On the other hand, complementary electronic energy levels (i.e., HOMO and LUMO) of additional component facilitates charge transport via the formation of favorable cascade energetic alignment. As illustrated in **Figure 6**, depending on the operational mechanism, the origins of performance enhancement in the ternary blend can be elucidated as follows: i) charge transfer: additional donor or acceptor are introduced as a third component that provides complimentary energy level to form cascade energetic alignment, which improves light harvesting and photocurrent generation via the charge transfer mechanism; (ii) energy transfer: the energy of the third component can be transferred to or from the binary system as the emission of energy donor and the absorption of energy acceptor are spectrally overlapped, which means that this mechanism is unlikely to participate in the direct charge generation; (iii) parallel linkage: the third component forms its own binary BHJ blend network with the dominant acceptor, which likely acts as an independent cell and is connected in parallel with an original binary blend; (iv) alloy type: the donor or acceptor with good miscibility and compatibility could be electronically coupled, leading to a new intermediate energy state with average values of frontier orbital (i.e., HOMO and LUMO) levels. In accordance with the fundamental mechanisms, controlling the microstructure/nanomorphology is critical for determining the charge transport/recombination dynamics and is even more challenging because of the increased complexity in the system. Although many important contributions have been made in the development of ternary OSCs,[101] recent NFA-based ternary OSCs that achieve simultaneously enhanced efficiency and stability will be mainly introduced in this section. [102–113]

Baran et al. reported ternary blend OSCs with enhanced efficiency and stability by combining donor polymers, P3HT or PTB-Th, with two NFA, IDTBR and 5,5'-[(6,12-dihydro-6, 6,12,12-tetraoctylindeno[1,2-b]fluorene-2,8-diyl)bis(2,1,3-benzothiadiazole-7,4-diylmethylidyne)]bis[3-ethyl-2-thioxo-4-thiazolidinone (IDFBR).[102] The ternary blend of P3HT:IDTBR:IDFBR (1:0.7:0.3) presented a PCE of 7.7 ± 0.1%, thus outperforming both binary counterparts, P3HT:IDTBR and P3HT:IDFBR, which exhibited a PCE of 6.3 ± 0.1% and 4.5 ± 0.1% respectively. By replacing P3HT with PTB7-Th, the ternary OSC produced an impressive PCE of 11.0%. The introduction of 30% IDFBR changes the microstructure, mitigating IDTBR aggregation and creating an optimal phase separation in the ternary blend networks. Moreover, the ternary blend OSC exhibited enhanced operational stability, with the ternary P3HT:IDTBR:IDFBR (1:0.7:0.3) blend device maintained 80% of its PCE during the air stability test for 1200 h, whereas the binary P3HT:IDTBR (1:1) blend showed more pronounced degradation, retaining 70%. In contrast, the reference P3HT:$PC_{61}BM$ blend lost more than half of its efficiency after stability test. For the photostability test under standard illumination condition of 100 mW cm^{-2} without encapsulation, P3HT:IDTBR:IDFBR device retained 85% of its initial PCE for 90 h, whereas P3HT:IDTBR and P3HT:IDFBR devices rapidly degraded, losing more than half of their PCEs. In addition to IDTBR, ITIC is one of the most widely used NFA.[103,106,107] Perylene diimides (PDIs) NFA that yields large π-aggregation in solid state due to their high molecular planarity could enhance the efficiency and stability of PTB7-Th:ITIC devices.[103] In terms of photon harvest, ITIC and PDI display complementary absorption. More importantly, such molecules also have a complementary relationship in morphology formation; the existence of PDI molecules affects the intermolecular interaction between PTB7-Th and ITIC and help to form desirable interpenetrating networks to facilitate charge transport, while ITIC makes PDI more miscible with PTB-Th by inhibiting PDI aggregation. With the optimized PDI/ITIC ratio of 3:7 (w/w), PTB7-Th:ITIC:PDI ternary blend OSCs yielded a PCE of 8.64%, higher than that of PTB7-Th:ITIC (7.51%) and PTB7-Th:PDI (3.70%) binary blends. Remarkably, devices fabricated under ambient condition showed comparable efficiency of 7.09%, suggesting excellent air stability of this ternary blend.

It was further found that two compatible polymer donors can also lead to a simultaneous enhancement in both efficiency and stability in ternary NFA OSCs.[106] By introducing PCDTBT as a third component into PBDTTT-EF-T:ITIC, the device performance was improved from 7.90% to 9.53%. Interestingly, Förster resonance energy transfer (FRET) from PCDTBT to PBDTTT-EF-T can be a possible origin for photocurrent increase, which is evidenced by the monotonous increase in PL intensity of PBDTTT-EF-T host polymer with increasing PCDTBT loading. The ternary blend also showed comprehensive enhancement in stability against air, thermal and photo induced degradations, which is mainly attributed to the interlocked morphology in the ternary films. The positive effect of the addition of a polymer acceptor as a third component was reported by An et al.[107] When N2200 was incorporated into the PBDB-T:ITIC system, the photon harvest and nanomorphology of the photoactive layer was enhanced, which was reflected by the EQE spectra and recombination kinetics.

It is interesting to note that fullerene acceptor additives also offer the potential for better performance in terms of efficiency and stability in NFA OSCs.[108–113] Doumon et al. demonstrated efficient and photostable D:A_1:A_2 type ternary blend OSCs by incorporating $PC_{71}BM$ as the third component in PBDB-T:ITIC.[109] By carefully tuning the A_1:A_2 (ITIC:$PC_{71}BM$) blend ratio, it was found that a small amount of PCBM (from 10% to 30%) significantly improves the photostability without compromising device efficiency. The resilience of the ternary blend to photodegradation is ascribed to its high durability of crystalline and molecular packing structure, which is reflected in AFM, GIWAXS and charge transport studies. Further, $PC_{71}BM$ was successfully incorporated as the guest acceptor into the host binary blend of PBT1-C and IT-4F (**Figure 7a**).[110] As a result, PCE is significantly increased from 11.0% for PBDT1-C:IT-4F to 12.2% for PBT1-C:IT-4F:$PC_{71}BM$ (1:1:0.2), resulting from the combined benefits of improved charge separation/transport and suppressed trap-assisted recombination. More importantly, due to the good compatibility of $PC_{71}BM$ with the host materials (PBT1-C and IT-4F), this ternary system exhibited excellent tolerance to the loading of the $PC_{71}BM$ component, maintaining high PCEs over 11.2% through the whole blend ratios. Recently, the narrow bandgap IEICO-4F have been widely applied in ternary blend OSC research due to its capability in absorbing the near-infrared region, which occupies a large portion of sunlight.[111–113] Despite this advantage, OSCs based on IEICO-4F NFA generally show a shortcoming of poor device stability. Several pioneering studies have been devoted to resolving such degradation problem using the ternary blend approach. Shi et al. reported considerable enhancements in both PCE and stability of J52:IEICO-4F OSCs by adding the $PC_{71}BM$ acceptor.[111] The high electron mobility of $PC_{71}BM$ contributed simultaneously to the suppressed recombination, balanced electron/hole mobilities and improved charge collection, which substantially increases the PCE from 9.21% for J52:IEICO-4F (1:1.5) binary blends to 10.68% for J52:IEICO-4F:$PC_{71}BM$ (1:0.9:0.6) ternary blends. Notably, it was observed that this approach provided another merit of better photostability. The PCE of the J52:IEICO-4F device reduced by about 50% after 100 h of white light exposure, while the J52:IEICO-4F:$PC_{71}BM$ device retained more than 80% of its initial PCE. Based on optical engineering, ternary OSCs with wavelength-selective harvesting properties were applied to greenhouse applications; for example, chlorophyll of green plants has a localized absorption for red and blue lights. Zhu et al. investigated the origin of the morphological degradation of PTB7-Th:IEICO-4F OSCs,[112] attributing the instability of PTB7-Th:IEICO-4F devices and stabilization in PTB7-Th:IEICO-4F:$PC_{71}BM$ devices to morphological changes , which can be interpreted in terms of thermodynamics. It was revealed that the hypomiscibility of IEICO-4F with PTB7-Th induces spontaneous phase segregation of IEICO-4F upon device aging, leading to isolated morphological traps and eventually percolation failure in the mixed region (**Figure 7b**). Such morphological instability can be largely restrained by the introduction of a third component; for example, $PC_{71}BM$ not only possesses a hypermiscibility of 48 vol% in the PTB7-Th donor polymer matrix at or beyond the percolation threshold, but is also partly miscible with aggregated IEICO-4F NFA molecules, which is beneficial for achieving efficient and stable OSCs. More recently, Lee et al. further enhanced the device stability of PTB7-Th:IEICO-4F:$PC_{71}BM$ ternary blend OSCs by adding less $PC_{71}BM$ than previously used.[113] Although the PCE of OSCs with a conventional PTB7-Th:IEICO-4F binary blend dropped to less than half of its original value after less than 50 h of exposure to light, the ternary PTB7-Th:IEICO-4F:$PC_{71}BM$ device remained approximately 80% of the original value after 500 h under the same condition, implying that ternary blend with $PC_{71}BM$ as the third component is more photostable than the binary counterpart.

On the other hand, studies on simultaneous improvement of efficiency and stability through a combination of two nonfullerene acceptors have been reported by Xue et al.[104] Using the narrow bandgap F8IC and mid-bandgap IDT-2BR together with PTB7-Th donor, complementary absorption with a broad photoresponse beyond 1000 nm was achieved in ternary OSCs. It was found that ternary OSCs employing a 20% IDT-2BR content provided the highest PCE of 12.1%, resulting from the combined effects of reduced voltage loss, enhanced light absorption in the short-wavelength region and energy transfer from IDT-2BR to F8IC (**Figure 7c**). Moreover, both F8IC and IDT-2BR exhibited favorable face-on molecular packing, which is beneficial for vertical charge transport, thereby leading to higher carrier mobilities and balanced charge transport. The ternary blend device showed a prolonged lifetime under air-stability and thermal stability tests compared to the binary blend device. As a fundamentally different approach, Du et al. presented an effective method through adjustments of the charge transfer state exciton dynamics, such as exciton diffusion, dissociation and charge recombination processes, achieved by the introduction of a delayed fluorescence emitter 3,4-bis(4-(diphenylamino)phenyl) acenaphtho[1,2-b]pyrazine-8,9-dicarbonitrile (APDC-TPDA) in PM6:Y6 OSCs.[105] Due to the large overlap between the PL of APDC-TPDA and absorption of PM6, the long lifetime singlet excitons of APDC-TPDA can be transferred to the donors via Förster resonance process, endowing the ternary OSC with better exciton utilization (diffusion and dissociation) and therefore enhanced J_{sc} value (**Figure 7d**). As a result, the ternary OSC based on PM6:Y6:10% APDC-TPDA yielded a high PCE of 16.96%, which is superior to that of the control device (15.24%). Furthermore, the ternary device retains about 96% of its initial PCE after 55 days of storage in ambient condition (T of 25 °C, RH of 25%, room light), compared to 82% of the initial PCE remained in the control device. It was suggested that the improved stability in the ternary OSC is likely related to the morphology and charge thermodynamic process: APDC-TPDA molecules are located at the donor/acceptor, which improves the film morphology, while delayed fluorescence is beneficial to enhance the exciton utilization.

2.3.3. Tandem and integrated NFA OSCs

Constructing a tandem structure is one of the most obvious ways of advancing the efficiency of solar cells by mitigating losses that come from photon transmission and thermalization.[114–122] Typically, tandem solar cells are made by stacking the multiple absorbers with complementary absorption spectra and by introducing so-called a recombination layer that comprises of the combined bilayer of p-type and n-type electronic materials between the sub-cells. Recently, the highest efficiency of 17.3% has been reported in tandem OSCs using PBDB-T:F-M and PTB7-Th:O6T-4F:$PC_{71}BM$ as front sub-cell and back sub-cell photoactive layers, respectively, and it is theoretically predicted that efficiency of over 18% can be achieved through a combination of existing materials.[123,124] The efficiency of tandem OSCs has been stagnant at ~10-11% for several years[125–129] but has recently started to rise sharply with the advent of NFA.[130–133] Since there are several review articles on tandem solar cells with fullerene acceptor, we will more focus on the recently reported NFA-related tandem OSCs.

Compared with fullerene acceptors, synthetic diversity of NFA enables a rational molecular design to control the electronic and optical properties, allowing sophisticated optical engineering on tandem OSCs. In 2017, Cui et al. reported over 13% efficiency tandem OSCs based on a new NFA, 3,9-bis((Z)-1-(6-(dicyanomethylene)-2-methyl-5,6-dihydro-6H-cyclopenta[b]thiophen-6-one-5-yl)ethylene)-5,5,11,11-tetrakis(4-hexylphenyl)dithieno[2,3-d:2′,3′-d′]-sindaceno[1,2-b:5,6-b′]dithiophene (ITCC-M) with an optical bandgap (E_g^{opt}) of 1.68 eV for the front cells and IEICO with an E_g^{opt} of 1.36 to fabricate the back cells (**Figure 8a**).[133] The individual sub-cells showed low energy loss and complementary photoresponse spectra. In addition, a recombination layer comprised of ZnO nanoparticle and pH-neutral self-doped conductive polymer, PCP-Na, further reduce the voltage loss in tandem OSCs, resulting in a low voltage loss of less than 0.02 V. Two NFA named F-M with an E_g^{opt} of 1.65 eV and NOBDT with an E_g^{opt} of 1.39 eV were designed by Zhang et al., covering a whole absorption range from 300 to 900 nm when blended with PBDB-T and PTB7-Th, respectively.[134] With the guidance of optical simulation and following systematic optimization of the thickness of each layer, an outstanding PCE of 14.11% was achieved. Liu et al. reported efficient tandem OSCs by adopting a new wide-bandgap NFA, TfIF-4FIC that has an E_g^{opt} of 1.61 eV.[135] The TfIF-4FIC offered a PCE of 13.1% with a high V_{OC} of 0.98 V and a J_{SC} of 17.6 mA cm^{-2} when PBDB-TF is selected as the donor. By using PTB7-Th:PCDTBT:IEICO-4F as the back sub-cell, a PCE of 15% was obtained (**Figure 8b**). More recently, Firdaus et al. synthesized two new NFA, namely IDTA and IDTTA, with E_g^{opt} of 1.90 and 1.75 eV, respectively.[136] With the aid of optical-electrical modelling, the best performing tandem OSCs with PBDB-T:IDTTA as the front cell and PTB7-Th:IEIC-4F as the back cell produced a high PCE of 15%, with a V_{OC} of 1.65 V, a J_{SC} of 13.6 mA cm^{-2}, and a FF of 0.67 (**Figure 8c**).

Perovskite/BHJ integrated solar cells are being investigated as another promising application area of OSCs.[137–140] Different from the conventional tandem cells that are comprised of physically separated sub-cells, perovskite and BHJ layers are monolithically stacked without any recombination layers to establish the integrated structure. Despite the theoretical predictions of ideal bandgap with a 33% efficiency limit,[141–143] most perovskite solar cells showed their best performances with an E_g^{opt} of 1.5-1.6 eV, which causes a significant transmission loss in the near-infrared region. The approach of expanding the absorption region utilizing a near-infrared-absorbing BHJ can improve the efficiency of perovskite solar cell by maintaining the V_{OC} and FF values but selectively increasing the photocurrent of the devices.[144,145] For proper device operation, both perovskite and BHJ layers should allow ambipolar transport with high electron and hole mobilities. Initially, integrated solar cell research has been devoted to extending the light absorption bandwidth via incorporation of narrow bandgap polymer:fullerene acceptor-based photoactive layer.[121-123,128,129] However, EQE of perovskite/BHJ integrated solar cells is still limited due to the relatively small amount of donor loading in BHJ and therefore resultant low gain in the near-infrared region, as reflected in the EQE of the OSC itself. Recently, several researchers have turned to their attention to the NFA-based OSCs to address this issue.

By integrating a narrow bandgap NFA, IEICO, along with PBDTTT-E-T on a methylammonium lead iodide ($MAPbI_3$) perovskite layer, the photoresponse of the EQE was extended to 930 nm and enhanced over 50% in the near-infrared region, leading to an impressive J_{sc} over 24 mA cm^{-2}.[146] Further, Wang and co-workers focused on the vertical component distribution within PBDB-T:IEICO layer to produce a bi-continuous interpenetrating network by simply optimizing their donor:acceptor blend ratio.[147] The PCE of $MAPbI_3$/PBDB-T:IEICO (1:0.7) is 15.47%, surpassing the reference cell of $MAPbI_3$/PBDB-

T:IEICO (1:1) with a PCE of 12.63%. Chen et al. reported a record J_{sc} value of 28.06 mA cm^{-2} in a perovskite/BHJ solar cells by integrating a ternary organic blend of S1:Y6:PCBM.[148] The perovskite has an E_g^{opt} of 1.6 eV, which is corresponding to the onset of EQE at ~775 nm, while absorption of the BHJ film extends up to ~980 nm (**Figure 8d**). Although distinct photoresponse was observed in perovskite with Y6:PCBM layer, overall improvement in the J_{sc} is negligible, which is attributed to the inefficient charge transfer between Y6 and PCBM. Such a problem was solved by adding p-type polymer S1, endowing the BHJ photoactive layer with enough driving force for charge separation and hole transport. Finally, a high PCE of 20.61% together with a V_{OC} of 1.09 V and a FF of 0.673 was achieved, which is among the highest values reported for perovskite/BHJ integrated solar cells.

2.3.4. Printed large-area NFA-based OSCs

A final step towards the ultimate goal of NFA technology would be the fabrication of highly efficient large-area OSCs via printing techniques that are compatible with high-throughput continuous roll-to-roll process.[149–155] A wide range of solution-based methods have been implemented for the deposition of organic BHJ layer, with spin coating as the most commonly used technique in lab-scale devices. Despite its availability and simplicity, spin coating is inevitably wasteful, cost-prohibitive, and not scalable for the mass production. Accordingly, many research efforts have been continuously paid to developing the optimal printing process that minimizes the efficiency losses when transitioning from high efficiency small area to printed large-area by understanding the solvent drying dynamics and resultant morphology evolution mechanism.[156] Based on the studies to date, it seems that the device optimization process through the printing process needs to be finely adjusted according to the molecular structure and the properties of the photoactive blends.[157–161]

In 2018, Ye and co-workers reported blade-coated OSCs using new photoactive blend of FTAZ with IT-M and halogen-free solvent without processing additive.[162] From the comparative study of different hydrocarbon solvent system, toluene, o-xylene, and 1,2,4-trimethylbenzene, quantified morphological parameters, including π–π coherence length, face-on orientation, and domain purity were altered, which correlates well with the performance of the printed devices (**Figure 9a**). As a result of the identification of the solvent-morphology-performance relations, a PCE of 9.8% was achieved in large-area (0.56 cm^2) OSCs fabricated by blade-coating method. The blade-printed NFA OSCs was further investigated using PTB7-Th:ITIC system by Lin and co-workers.[163] It was found that the addition of 0.6 vol% of high boiling point additive 1,8-diiodooctane endows the doctor-bladed photoactive layer with slow morphological evolution that contributes to the facile migration of ITIC molecules, leading to a favorable nanoscale phase separation (**Figure 9b**). The PCEs of 9.5% and 7.6% were realized in printed conventional devices and in flexible large-area (2.03 cm^2) ITO-free OSCs, respectively. Recently, a low-cost processing method, soft porous blade printing, was developed for printable NFA OSCs.[164] Interestingly, filter paper was able to perform as printing blade that possesses inherent porous microstructure which offers high shear rates and thereby facilitates the molecular orientation of photoactive materials. The resulting printed devices exhibited high PCEs of 11.85% and 14.75% for PTQ10:IDIC and PM6:Y6, respectively. On the other hand, the blade-coating method has a drawback; the slow solidification gives a higher chance to cause phase aggregation. When Dong et al. added a polymer additive N2200 to PM6:Y6 BHJ, excessive aggregation of NFA in the printed photoactive layer was effectively suppressed, achieving a high PCE of 15.1% in large-area OSCs (1.0 cm^2).[165]

The research results presented in the above section addressed the development of blade technique for BHJ layer coatings. The solution processing of BHJ organic photoactive material blends is an efficient way to produce a phase-separated nanoscale morphology, but this method still has some disadvantages; BHJ morphology is difficult to control and is highly sensitive to various factors, such as material properties and processing condition, which makes this approach only applicable to individual photoactive systems. In addition, optimized BHJ morphology is typically in a metastable state and therefore prone to maintain a thermodynamic equilibrium, resulting in phase aggregation. Recently, Sun et al. developed a layer-by-layer (LbL) coating technique to deposit an organic photoactive layer to address this issue.[166] In-depth, comprehensive analyses revealed that LbL-bladed blend exhibited not only thermodynamically favourable nanomorphology with appropriate domain size, but also desired hierarchical morphology with a vertical phase segregation. In addition, the devices with LbL-constructed photoactive layer exhibited improved photo- and thermal stability compared with those of bladed-BHJ counterparts.

3. Toward Superior stability of NFA-based OSCs

3.1 Stability and degradation mechanisms under various stress conditions

Although NFA have undergone rapid advance in their molecular design resulting in significant breakthroughs in the performance of OSCs, long-term stability remains a critical consideration for the commercialization of NFA OSCs. While promising lifetime have been demonstrated for some NFA based OSC systems under certain environment stress conditions,[37,167,168] the origin of such improvement often remains unclear and, more importantly, there remains a lack of concrete molecular design rules to enhance the stability of NFA-based OSCs. In this section, an up-to-date overview of the recent research progress on the stability studies of NFA OSCs is summarized, highlighting the degradation mechanisms of different NFA-based OSC systems under illumination in air (photochemical), illumination in inert atmosphere (photostability) and thermal (morphological) stress conditions. It is worth to note that although not specifically introduced in this section, electrochemical stability dealing with the structural stability of molecules under electric field stress, is important in terms of operational stability. However, the hint is that electrochemical stability is known to be related to the backbone planarity of the molecule, which has a profound effect on photochemical stability.[169,170] In this respect, it will also be interesting to study the link between photochemical stability and electrochemical stability.

3.1.1 Photochemical stability

The rapid degradation of device performance under combined exposure to illumination, oxygen and humidity has been widely recognized as a long-standing challenge for OSCs, which can hinder the long term device stability in several ways initiated by the ingress of oxygen and water into the device as illustrated in **Figure 10a**. Chemical corrosion of ITO and low work function Al/Ca will create an insulating metal oxide layer between the electrode and the photoactive layer, eventually leading to S-shape J-V curve of the device.[171] Molecular oxygen that penetrates into the active layer can cause photo-oxidation reactions of the donor and acceptor segments, which may further deteriorate charge carrier kinetics and device performance.[172] Employing encapsulation is an effective strategy to block the oxygen and water permeating pathways and therefore increase the photochemical stability of OSCs. However, in addition to significantly increased fabrication cost, commonly used encapsulation materials such as epoxy resin and glass usually introduce harmful solvents and create additional mechanical stress, and rigid glass has poor compatibility with flexible devices.[173] While the limited chemical stability of device electrodes could effective mitigated through the adoption of more stable electrode materials, suitable hydrophobic buffer layers and inverted device architecture,[68,174] enhancing the intrinsic photochemical stability of the photoactive materials, on which only limited progress has been made to date, is a key strategy to mitigate the photochemical degradation of OSCs.

Photooxidation of the acceptor molecules induced by the exposure to light and oxygen has been identified as a major photochemical degradation pathway for OSCs, with oxygen atoms occupying the C=C bonds in the acceptor molecule leading to a change in the molecular structure and energy levels. Such reaction has been well investigated for fullerene molecules, with the formation of epoxides and carbonyls on the C_{60} cage both identified as the photochemical degradation products.[9,10] The photooxidation of NFA molecules is relatively less understood, which requires further analysis. Taking ITIC for example, photo-oxidation reaction may occur at multiple sites of the molecular structure (**Figure 10b**), including the double bonds between the donor and acceptor units, on the thiophene or bithiophene outlying central building blocks and side chains. Upon exposure to light and oxygen, oxygen atoms can be chemically attached to the ITIC molecule by forming new hydroxyl and carbonyl groups, thereby causing an increase in C-O bonding as well as scissoring of the macromolecular chain bond and destruction of the π-conjugated system of the ITIC backbone, resulting in a dramatic change in its molecular structure upon photooxidation.[175] Such photooxidation of ITIC is found to have a significant impact on the device performance (blended with J71), with a PCE loss of 70% - 100% upon only 30 minutes of exposure to light and air depending on the choice of device structure and interlayers.[175] Luke et al. performed a comparative study of the photochemical stability of two structurally similar NFA molecules, namely O-IDTBR, which has a planar molecular structure and O-IDFBR, which has a non-planar molecular structure with a dihedral angle of 33°. It was found that the photo-oxidation of NFA molecules involves three phases:[176] i) A photoinduced conformational change first occurs (i.e. torsion about the core-benzothiadiazole dihedral), induced by noncovalent interactions with molecular oxygen, followed by ii) photo-oxidation or fragmentation of the molecular backbone, leading to bleaching of the chromophore. Finally, iii) the chromophores of the NFA molecules are completely bleached.

It is found that the photo-oxidation process can be mediated by the triplet exciton kinetics with the formation of singlet oxygen, which has been well studied for fullerene and polymer donors.[177][178] For example, the PCBM triplets can be formed via intersystem crossing from the PCBM singlet state after the absorption of photons, and these triplet states can be quenched by molecular oxygen to generate highly reactive singlet oxygen.[179] While the triplet-mediated photo-oxidation study of NFA is limited, Y6 is found to be a triplet acceptor and therefore may suffer from severe photo-oxidation process in air.[171] Another photochemical degradation pathway is through the formation of superoxide (O_2^-) radical ions via photoinduced transfer of electrons from the acceptor to molecular oxygen, which in turn react with both the donor and acceptor in the active layer resulting in severe photochemical degradation.[180] Speller et al. reported that the photochemical degradation of OSCs through the pathway of superoxide formation is strongly dependent upon the energetics of the acceptor. Specifically, it was found that (see **Figure 10 c-d**) a shallow LUMO level of the acceptor (e.g. IDTBR family) above a threshold (3.75 eV) facilitates the transfer of electrons to molecular oxygen to form superoxide, which further reacts with both the electron donors and acceptors. For electron acceptors with deeper LUMO levels (e.g. PCBM), this process is energetically less favorable and is therefore suppressed. This process appears to be general and is independent of whether fullerene acceptors or NFA are used. In addition, electrons at the LUMO level of the acceptor can also originate from direct photoexcitation of the acceptor and is therefore more likely to occur in NFA blend films due to their typically stronger optical absorption than that of fullerene acceptors.[181]

3.1.2 Photostability in inert atmosphere

Under constant illumination in inert atmosphere, OSCs usually exhibit a steep decrease in PCE within the initial degradation period (typically within several tens to hundreds of hours), followed by a more gradual degradation over the longer period. This initial fast degradation is typically referred to as “burn-in”. The origin of burn-in degradation of fullerene based OSCs has been widely investigated, with photoinduced fullerene dimerization, blend demixing and disorder-induced losses identified as potential degradation mechanisms.[37,182,183] Recently, there have been increasing studies of the photostability and burn-in degradation behaviour

NFA-based OSCs. Du et al. investigated the photostability of OSCs based on blends of PBDB-T with several ITIC NFA, namely ITIC, IT-4F, ITIC-M, ITIC-DM and ITIC-Th, in comparison with OSCs based on with PBDB-T:PCBM blend. It is found that subtle changes in the molecular side chain and end groups of ITIC family NFA can induce significant impact upon the photostability of the resultant OSCs, primarily linked to the breaking of conjugation leading to increased energetic traps. Interestingly, fluorination of the end-group was found to stabilise the NFA molecule against photodegradation, while adding methyl groups displayed an opposite trend, although the origin of which requires further investigation. The authors further observed a change in the molecular orientation of ITIC orientation in the blend from face-on to edge-on upon illumination, suggesting that morphological change may also be linked with the photodegradation of ITIC-based NFA OSCs.[184]

In addition to the light-induced molecular change, recent studies indicate that the interlayer can introduce additional degradation pathways to NFA through photocatalytic reactions.[185–191] It was found that the vinyl group of enone in ITIC can undergo a radical addition reaction with the hydroxyl radicals on the ZnO surface (typical defects under UV light irradiation for low-temperature and solution processed ZnO), and this ITIC radical intermediate can further decompose to other fragments or attack the enone group of another ITIC molecule to form dimerized ITIC (see evidence in **Figure 11a**). Such photocatalytic reaction can retard electron transport and lead to significant local charge accumulation and recombination at the ZnO interface, resulting in reduced FF and V_{OC} and severe burn-in degradation under 1 sun light soaking with the PCE of encapsulated PBDB-T:ITIC OSCs losing more than 30% of their initial value within the first 50 h.[192] This ZnO assisted photocatalytic reaction appears to be a general cause for the severe burn-in degradation of NFA OSCs, since cutting off the ZnO/active layer contact can rectify the overall device stability. [68,193] Wang et al. reported that such interfacial reaction resulted burn-in degradation can be aggravated by the change of the blend morphology. A vertical phase stratification between PBDB-T and ITIC was obseved in the BHJ photoactive layer of PBDB-T:ITIC OSCs during photo degradation, revealed by depth profiling XPS measurement of the vertical distribution of the PBDB-T and ITIC components.[68] The relative amount of ITIC and PBDB-T can be indicated by the ratio of the N_{1S} XPS peak area to the S_{2P} XPS peak area (N_{1S}/S_{2P}), since N_{1S} core level in XPS is unique to the ITIC film, and S_{2P} exists in ITIC and PBDB-T film. As shown in **Figure 11b**, the N_{1S}/S_{2P} ratio of the bottom surfaces increases along the degradation time, while the ratio of the top surfaces decreases, implying the exisitence of a PBDB-T-rich region toward the upper surface and an ITIC-rich region near the vicinity of the bottom surface of the OSC (inset of **Figure 11b**). Such vertical phase stratefication is found to cause reduced charge percolation pathways and increased bimolecular recombination losses, thereby resulting in deteriorated device performance upon photodegradation.

Notably, recent advances in the molecular design of NFA have resulted in the demonstration of a number of burn-in free OSC systems achieving superior long-term stability (e.g. estimated liftimes > 10 years), thereby representing a significant technological breakthrough in overcoming the stability challenges of OSCs.[37,167,184] These progress will be further discussed in the following sections.

3.1.3 Morphological stability

Morphological stability of the photoactive layer is a crucial consideration to ensure the stable operation of OSCs under illumination or thermal stress. While thermally induced aggregation/crystallization, phase demixing and vertical stratification have been identified as potential degradation pathways of fullerene-based OSCs through the detrimental effects on charge separation and transport, morphological degradation of NFA based OSCs under illumination or thermal stress has received relatively little attention to date. It has been reported that miscibility of the donor and the acceptor, as well as the crystallinity of the NFA, play a decisive role in the morphological stability of NFA-based OSCs, which will be discussed in detail below.

Miscibility: Xiao et al. reported that NFA OSCs based on the PTB7-Th donor and EH-IDT acceptor possess high efficiency of 9.17% and excellent photostability with a lifetime T_{80} of 2132 h, while the devices based on ITIC and IDIC acceptors exhibit both lower performance (PCE of 7.28% and 6.12%, respectively) and poorer photostability (T_{80} of 221 h and 558 h, respectively). Since no chemical change was identified, morphology change after illumination was considered the main origin for the severe burn-in degradation of ITIC and IDIC based devices. Investigation of the degradation mechanisms indicate that the morphological degradation is strongly linked with the miscibility between the donor and acceptor, which can be described by the Flory-Huggins interaction parameters as shown in **Table 4**. With less positive Flory-Huggins interaction parameters, the donor:acceptor blends show better miscibility, consistent with the higher morphological stability and device photostability of PTB7-Th:EH-IDT devices than the PTB7-Th:ITIC and PTB7-Th:IDIC devices. It was further found that the poorer miscibility between PTB7-Th and ITIC/IDIC also affects the exciton generation and dissociation kinetics as shown in **Table 4**, where the PCE10:ITIC and PCE10:IDIC devices show smaller maximum exciton generation rate (G_{max}) and exciton dissociation probability (P(E,T)) than PTB7-Th:EH-IDT devices before and after 500 h of photoaging, which further lead to poorer device performance.[194]

Crystallinity: It is found that casting PBDB-T:INPIC-4F under solvent vapor can prolong the molecular organization time, causing the polycrystals of INPIC-4F molecules to grow into pronounced spherulites, resulting in enlarged phase separation. Reducing the molecular organization time by casting the films on a hot substrate can suppress the polycrystalline structure and enhance the face-on π-π stacking of INPIC-4F, leading to fine nanoscale morphology.[195] As shown in **Figure 12a**, ITIC crystallizes in a profoundly different way with fullerenes and it undergoes a glass-crystal transition considerably below its T_g, i.e. forming low-temperature polymorph I nanocrystals through a diffusion-limited crystallization process in the regime of $0.8T_g < T_{ann} < T_g$. The resulting fine-grained nanostructure does not evolve further with time and hence is characterized by a high degree of thermal stability. Instead, above T_g and below T_m, the low temperature polymorph melts, and micrometer-sized crystals of a high-temperature polymorph II crystals develop, enabled by more rapid diffusion and hence long-range mass transport. This leads to a detrimental decrease in photovoltaic performance.[196] The different crystal growth situation under low and high temperatures are further confirmed by the polarized optical microscopy images (**Figure 12b**), which indicates that below T_g (~180 °C) only nanometer-sized crystallites can be observed, while above T_g micro spherulites corresponding to polymorph II are discerned. These two types polymorphs lead to different OSC device performance and stability as indicated in **Figure 12c-d**. When the annealing temperature is close to or above 180 °C, the device PCEs gradually deteriorate. With increasing annealing time, PCE of the 210 °C annealed devices drops from ~7% to ~5% in 10 min, while PCE of the 160°C annealed devices drops to similar value in 1000 min showing a higher thermal stability. The above results indicate that diffusion-limited crystallization of nonfullerene acceptors below T_g is an effective method to improve the long-term stability of OSCs.[196]

The miscibility of donor/acceptor and crystallinity of the acceptors should synergistically affect the thermal stability of the photoactive layer. Schematics of the possible scenarios of morphology evolution in an upper critical solution temperature (UCST) polymer: small molecular acceptors (SMA) blend with an amorphous donor and crystallizable NFA with a low and an optimal miscibility are illustrated in **Figure 13**. Severe burn-in degradation can be expected when the optimal morphology is quenched near the percolation threshold and is far from the miscibility gap, referred to as a ‘‘low-’’ or ‘‘hypo-miscibility’’ system. On the other hand, a device with a miscibility gap close to the percolation threshold (**Figure 13b**) during the normal device operation conditions is referred to as ‘optimal miscibility’’ and is expected to exhibit a relatively stable morphology and thus lower or slower burn-in degradation. It is known that thermal annealing can boost the efficiency of many OSCs; however, heating may accelerate the transition of the morphology from the meta-stable miscibility gap to the liquidus or directly and simultaneously lead to crystallization failure as a result of nucleation or growth of SMA crystals. The propensity for this transition to occur will depend on T_g, which is an indicator of the degree of vitrification at room temperature. Conceptually, there are three main classes of systems for crystallizable NFA: class I systems that are unstable as a result of demixing and crystallization (low T_g case in **Figure 13a**), class II systems that have meta-stable mixed domains but can crystallize (low T_g case in **Figure 13b**), and class III systems that are kinetically stabilized irrespective of whether they are meta-stable or not (high T_g cases). Class III can be subdivided into class IIIa when a hypo-miscibility system is vitrified and class IIIb when an optimal miscibility, meta-stable system is vitrified.[197]

3.1.4 Deterioration of charge carrier kinetics

In the view of device physics, the formation of trap states caused by structural defects, trapped oxygen, local disorder, and organic/inorganic impurities is one of the major possible origins responsible for the degradation of OSCs.[198–201] Such trap states are usually energetically located in the bandgap and play a negative role in affecting the device operational stability in the following ways: 1) lower the charge carrier mobility due to the charge trapping/detrapping processes; 2) influence the field distribution inside the device and 3) act as recombination centers. In particular, it was proposed that FF losses observed in many photodegraded NFA OSCs can be linked to increased trap state density and concomitant charge trapping into the intra-bandgap tail states, assigning the non-ideal behavior with reaction rate greater than an ideal 2nd order bimolecular recombination.[202] Moreover, tail-state profile broadening arising from structural defects or disorders may increase the population of deep-trapped charges, in which immobile charge carriers in the localized states require thermal excitation to reach the mobility edge to become mobile.[200,203–205]

The trap state density and energetic distribution of tail states can be assessed by the transient photovoltage (TPV) and charge extraction (CE) measurements. The energetic distribution of tail states is driven by the slope of charge carrier density n versus V_{OC}. Cha et al. investigated the charge carrier density and recombination dynamics of OSC devices using representative fullerene acceptor and NFA BHJ systems based on PffBT4T-2OD:$PC_{71}BM$ and PffBT4T-2OD:EH-IDTBR.[37] It was found that the PffBT4T-2OD:$PC_{71}BM$ OSC undergo photodegradation upon exposure to illumination 60 h, in conjunction with a 50% increase in charge carrier density as compared with fresh devices, implying an increase in the density of electronic trap states, considering that the charge carrier density is mainly presented in the shallow trap states. Furthermore, this result is coincident with the observation of extended carrier lifetime, resulting from increased charge trapping. For PffBT4T-2OD:EH-IDTBR, however, there was little variation in both CE and TPV results between fresh and aged devices. Gasparini et al. also explored the photoinduced loss mechanisms of P3HT:IDTBR and P3HT:PCBM systems using TPV measurement to derive the charge carrier density lifetime τ and charge carrier density n.[167] The aim of this approach is to explore the change in recombination order R between fresh and aged devices. The relationship between τ and n, $\tau = \tau_0(n_0/n)^{\lambda}$, where λ is a recombination exponent, can determine the recombination order R ($R = \lambda + 1$). The fresh and photoaged P3HT:PCBM devices exhibited an R value of 2.3 and 3.0 respectively, compared to 2.1 and 2.7 for fresh and photoaged P3HT:IDTBR, in which a deviation of the recombination behavior from an ideal 2nd order recombination (R = 2) can be assigned to the trap state formation in photoaged OSCs. However, more disordered charge transport is evident from the higher recombination order observed in P3HT:PCBM, which is considered as responsible for the subtle drop in V_{OC} during light soaking. In contrast to P3HT:PCBM where the miscible PCBM diffuses into polymer phase to decrease the crystallinity of P3HT, P3HT:IDTBR formed purer domains with higher polymer crystallinity, leading to lower susceptibility to light-induced trap formation. Interestingly, Xiao et al. found that some NFA such as ITIC, IDIC and EH-IDT follow the opposite trend – that is, inferior stability with poor donor-acceptor miscibility.[194] PTB7-Th:EH-IDT OSCs have an excellent morphological durability against photodegradation, which is attributed to the good miscibility of PTB7-Th and EH-IDT. However, because of the poor miscibility of ITIC and IDIC with PTB7-Th, their BHJ photoactive layers underwent severe morphological degradation, resulting in severe recombination losses with increased trap states. In addition to the donor-acceptor miscibility, significance of end-group/side-chain engineering of the NFA on the photostability of OSCs has also been reported.[184] The fluorination of the end-group is beneficial for stabilizing the NFA molecular orientation during photoaging, whereas NFA with methyl group are vulnerable to photo-induced chemical degradation, resulting in increased energetic traps and therefore accelerated device degradation.

3.1.5 Stability under low light condition

One of the most important markets for indoor organic photovoltaics is to replace small batteries that power sensors to reduce the maintenance of wireless devices. To replace the battery market of the IoT, such as the replacement of small batteries powering sensors, the PCE of the indoor organic photovoltaics device should be higher than 20% under 500 lx and generate a power output of about 30μW/cm^2, and indoor organic photovoltaics devices must be stable enough to maintain at least 80% of its initial efficiency for more than 10 years.[206]

An important point to consider for indoor energy harvesting is that indoor light sources (e.g. incandescent bulb, FL, and LED) usually lack the UV portion[13,207,208] that have been identified as a factor of deterioration of OSCs. It has been revealed that the UV light exposure appears to change the molecular[209–212] and micro-structure[209] of organic BHJ blends which can cause the formation of defect/trap states and initiate the degradation of device performance. On the other hand, Patel et al. argued that the deterioration of device interlayer, induced by UV light, is the main cause of degradation, rather than a change in the BHJ photoactive layer.[213] Therefore, studies on the stability of indoor organic photovoltaics are likely to be less relevant to UV-induced degradation mechanisms. Nevertheless, owing to the generally complicated indoor environments, the effect of various stress factors such as oxygen, illumination, temperature, and humidity on the stability of indoor organic photovoltaics should be investigated and mitigated. Cui et al. investigated the photostability of indoor organic photovoltaics based on the PM6:IO-4Cl nonfullerene blend system under continuous indoor illumination at a temperature of 25-30 °C with a relative humidity of 40–60% as shown in **Figure 14a**. It was found that encapsulated IO-4Cl-based organic photovoltaics devices remain their original PCE after 1000 hours, showing an excellent photostability.[11] The authors further fabricated indoor organic photovoltaics based on three different blend systems PM6:$PC_{71}BM$, PM6:IT-4F and PM6:ITCC, obtaining a PCE of 17.2%, 19.6% and 21.2% with an output power of 26.0 $\mu W/cm^2$, 29.6 $\mu W/cm^2$ and 32.0 $\mu W/cm^2$ respectively.[214] Furthermore, their stability was tested under both continuous weak (2700 K LED) and strong (white LED) illumination (**Figure 14b)**, with all three devices undergoing minimal degradation under weak illumination with less than 10% reduction in PCE after 500 hours. However, all devices exhibited dramatic degradation under strong illumination, retaining less than 15% of their initial PCEs after 160 hours. Since a mild thermal stress was present at ~ 45 °C during degradation due to the strong illumination, dark thermal stability test of the devices under 45 °C was undertaken as a control experiment as shown in **Figure 14c**. It was found that after 160 hours of thermal ageing, all indoor organic photovoltaics devices suffered a drop of PCE, with a PCE loss of around 60%, 40% and 20% for the PM6:$PC_{71}BM$, PM6:IT-4F and PM6:ITCC devices respectively.[214] The findings suggest that both the strong illumination and thermal stress can contribute to the degradation of the indoor organic photovoltaics devices,[12] with fullerene-based indoor organic photovoltaics (such as PM6:$PC_{71}BM$) suffering a more severe degradation compared to NFA-based devices (such as PM6:ITCC and PM6:IT-4F). Park et al. studied the thermal stability of PM6:IT-4F and PBDB-TSCl:IT-4F-based indoor organic photovoltaics at 100 °C under an inert atmosphere. As shown in **Figure 14d**, a PCE loss of 25% was observed for PM6:IT-4F devices, in comparison to a PCE loss of only 5% for PBDB-TSCl:IT-4F devices. The better thermal stability of PBDB-TSCl:IT-4F organic photovoltaics was attributed to a more stable blend morphology of the photoactive layer, with no significant change in the blend morphology upon thermal degradation.[215] The findings therefore suggest that ensuring good intrinsic photostability of the photoactive materials, in addition to a stable blend morphology of the photoactive layer, particularly under thermal stress conditions relevant to various indoor environments, are both critical considerations in order to achieve long term stability of indoor organic photovoltaics.

Indoor organic photovoltaics may operate under high-humidity environments, and device degradation caused by moisture could be another major degradation pathway of indoor organic photovoltaics, especially for unencapsulated devices. It has been widely established that certain moisture sensitive electrode and interlayer materials such as PEDOT:PSS and calcium can cause rapid degradation or failure of organic photovoltaics. Such degradation pathway can be effectively alleviated by encapsulation or use of more moisture-stable electrode and interlayer materials.[216] While it is reasonable to expect that indoor organic photovoltaics may share some similar degradation mechanisms to those for outdoor applications, additional degradation mechanisms may exist resulting from the different requirements of materials and device design, as well as the different operating environments. Further research is needed to fully understand the stability and degradation mechanisms of indoor organic photovoltaics.

3.2 Methods toward stable NFA devices

One of the main scientific questions in the current research landscape of NFA is about understanding and meeting the requirements to achieve highly stable OSC performances in devices and controlling degradation mechanisms related to various operating environments. Even if the requirements for long OSC lifetime still need to be fully understood, recent works have investigated these aspects and pinpointed some favorable characteristics in terms of NFA molecular design, BHJ morphology and device architecture to ensure stable device operations. Before addressing specific examples, it is relevant to give an overview of the most common and useful experimental techniques to assess OSCs stability and to investigate the origin of degradation mechanisms. **Table 5** summarizes a large number of them with an explanation of the type of information about the samples provided by each. In the most frequent measurement protocol for all these techniques, the samples are probed before and after a period of aging (e.g. dark, light, thermal…) to identify the changes in materials properties or device behavior due to the degradation processes involved. Another option is the continuous measurement at regular intervals during the aging time, for example commonly used to monitor the evolution of photovoltaic parameters.

Summarizing the most relevant literature produced with the help of these experimental tools, the current landscape of the understanding of the key parameters for achieving long lifetime in NFA-based OSC is presented in this section. This takes into account the requirements for molecular structure and energetics of the molecules, interfacial properties in the device and BHJ optimal morphology.

3.2.1. Molecular structures

Energy level: The triggering of oxygen-induced chemical reactions, widely studied as common route for OSC degradation as described above, is closely related to NFA molecular properties, in particular to energetics. To overcome the electrochemical oxidation, NFA should own low-lying LUMO energy level below -4.0 eV.[217] For instance, two NFA materials IDT(TCV)$_2$ and IDTT(TCV)$_2$ and polymer PTB7-Th based OSC devices exhibited superior stability of more than 1000 h under dark ambient conditions without encapsulation, in which IDT(TCV)$_2$ and

IDTT(TCV)$_2$ own LUMO levels of -4.18 eV and -4.06 eV, respectively. While the devices only exhibit PCEs of around 3% due to a big voltage loss, [218] a redesign of the NFA with deeper LUMO energy levels, as well as their matching donor polymers with deepened HOMO levels to compensate the V_{OC} loss, might be a promising route toward the development of both efficient and environmentally stable NFA OSCs.[181]

Chemical structure: Chemical structure of NFA is a key parameter to control the different mechanisms of degradation. For example, in a work by Guo et al. comparing different NFA molecules, a series of films were found to photo-bleach at substantially different rates varying from minutes to days. **Figure 15a** provides the photo-bleaching rates of NFA and fullerene derivatives films during continuous illumination with a xenon arc lamp exposed to an ambient atmosphere.[175] It is found that the photo-bleaching rates of the investigated NFA with the exception of IDIC-4F, IDIC-4Cl, O-IDTBR and l-IDTBTRh are slower than those of PCBM and PC$_{71}$BM. A large variety of NFA have been developed over the last years by different routes of molecular engineering focusing on the key constituent components of typical NFA chemical structure. These includes tailoring of donor units, acceptor units, conjugated bridges or side chains and heteroatom substitutions, developed to tune the blend morphology and improve the optoelectronic properties. Based on this view, the differences of photo-bleaching rates in these NFA presented in **Figure 15a** can provide some promising inspiration for NFA design:[175] 1) the NFA based on chlorine-substituted end groups are much more stable than fluorine-substituted acceptor units in fused-ring electron acceptor (FREA); 2) end-capping groups methyl-INCN, dimethyl-INCN, and CPTCN as well as methyl-CPTCN and Cl-CPTCN may not be able to enhance the photo-oxidation stability of FREAs; 3) O-IDTBR based on two dual acceptor units is more stable than IDIC based on INCN as the end group; 4) in the donor units, replacing common central building blocks with other units with stronger electron-donating ability is an useful way to suppress photo-bleaching of FREAs; 5) ITIC based on alkylbenzene units as side chains is more stable than the alkylthiophene-substituted ITIC-Th molecule.

In addition to the structural design of NFA, the pure chemical role of end groups and side chains in ITIC derivatives is also crucial for OSC stability, with reports from Du et al. of much longer lifetime of IT-4F and ITIC-Th in comparison to methylated ITIC-M and ITIC-DM.[184] The device stability tests (**Figure 15b**) under continuous illumination in dry N_2 atmosphere show that the OSCs based on IT-4F and ITIC-Th achieve an excellent extrapolated T_{80} lifetime of up to 11000 h and 9500 h, respectively (corresponding to an operational lifetime around 10 years). Conversely, for solar cells based on ITIC, ITIC-M and ITIC-DM, increased energetic traps lead to higher recombination order and thus decreased J_{sc} and FF. Fluorination of the end-group stabilizes molecules against light soaking, while adding methyl groups shows a clear opposite trend. The ITIC-DM molecule with four methyl groups exhibits the worst photostability due to combined effect of chemical and morphological change during light illumination.[184] However, on a shorter timescale Doumon et al.[219] show the opposite results, with fluorinated ITIC less stable than methylated counterpart due to imbalanced electron-hole mobilities. Interestingly, this is only verified in conventional device structure, suggesting that OSC architecture and interfaces play an important role on photo-stability. It is concluded that in order to achieve high device stability as well as good performance, organic photoactive materials require stable aromatic structures and the absence of chemically vulnerable functional groups. The photoactivity of the molecule can also be limited by specific localized modifications onto the NFA structure. Examples include end-group chlorination – more than fluorination –, the presence of two contiguous acceptor blocks such as in O-IDTBR and the increase of electron-donating character of the central unit.[175] Interestingly, both shortening and elongation of the seven-fused-ring core structure of ITIC are found to decrease the photo-oxidation rate, respectively in six-unit-core IHIC and eight-ring F8IC, C8IC and T8IC.

Molecular conformation: Research attention has also been focused on the conformation of the molecular structure to effectively improve NFA photo-oxidation stability. As shown in **Figure**

15a, a-IDTBTRh based on angular a-IDT subunit exhibits an extraordinarily high photo-bleaching rate of 287%, while the l-IDTBTRh based on linear l-IDT only show a small photo-bleaching rate of 0.04%, about four orders of magnitude difference.[175] Another demonstration of the importance of molecular conformation for stability is shown by the comparison of two isomers of ITIC-based acceptor with fluorine atoms at the ortho-alkyl (oF-ITIC) and meta-alkyl (mF-ITIC) positions. The two of them show different device thermal stability when blended with polymer PBTIBDTT. The mF-ITIC shows the best thermal stability, retaining 92% of its initial PCE after thermal annealing for 96 h at 150 °C, while ITIC and oF-ITIC based devices only preserve 82% and 67% of their initial efficiencies, respectively.[220] This is due to that the crystallinity of oF-ITIC and mF-ITIC was weakened due to side-chain fluorinations with mF-ITIC showing the least crystallinity. The reduction of crystallinity is beneficial for improving the thermal stability due to the weak driving force to form large aggregations in both pure film and blend film. Both ITIC and oF-ITIC pure films indeed showed numerous aggregations. The findings also provide an important insight and a possible avenue for improving the photostability of NFA by enhancing the molecular conformation stability. For example, the in-situ accelerated photo-irradiation study of the Y6, ITIC and O-IDTBR materials under N_2 exhibited that both IDTBR and ITIC showed significant changes in their molecular vibrational spectra, while no major changes in the vibrational spectra of Y6 indicating its superior photochemical stability.[221] The global potential energy minimum for Y6 molecule from DFT calculation appears only at dihedral angle of 0°, strongly favorable with respect to the local minimum at 180°, which is higher in energy by 0.4 eV (**Figure 16**). Conversely, for ITIC and IDTBR the potential energy for 0° and 180° configurations are equivalent. This indicates the conformational uniformity and rigidity specific of Y6 in comparison to other A-D-A NFAs. The origin of Y6 conformational rigidity, and therefore high chemical stability, is the presence of its alkyl side chain on the outer core that restricts end-group rotation by acting as a conformation locker. Different synthetic routes are available to optimize NFA design to ensure molecular rigidity, since a planar and rigid backbone prone to form highly crystalline films is a key to extend OSC lifetime. For example, this can be achieved by conformational lockers[222–224] and avoiding steric hindrances between A-D building blocks. In fact, photo-induced distortion is found to be accelerated by an initially twisted backbone (e.g. IDFBR versus IDTBR).[176] These examples also suggest that BT unit in A-A-D-A-A calamitic acceptors can be a possible trigger of photochemical reactions.

Antioxidizing processing: The use of stabilizers such as antioxidizing agents to regulate the detrimental chemical reactions and inhibit the photo-oxidation of the photoactive materials may be a promising strategy to enhance the stability of NFA OSCs, considering the successful application of several stabilizers in biology, perovskite solar cells (PSCs) and polymer:fullerene OSCs.[178,225–228] For example, the inexpensive natural antioxidants uric acid,[229] tea polyphenol[230] and ascorbic acid[231] have been used in tin-based PSCs to prevent the oxidation Sn^{2+}, thereby resulting in significantly improved device stability. It has been found that a set of structurally varied hindered phenols can stabilize the lifetime of P3HT:PCBM devices without compromising their performance, owing to the hydrogen donation and radical scavenging properties of hindered phenols which can significantly reduce the radicals within the photoactive layer.[232] Although there are only limited studies in the application of natural antioxidants in NFA, employing a suitable antioxidant can be a general and efficient method to improve OSC photochemical stability, as indicated by its reaction mechanism as shown in **Figure 17a**. For polymers or NFA, there are mainly three reactive sites: alkene-based units, cyclopentadiene based units (e.g. thiophene) and alkyl chain based units. The quenchers or stabilizers can effectively inhibit the presence of reactive oxygen species (ROS), thereby avoiding the decomposition of pristine polymers or NFA (RH). In addition, under illumination, free RH radicals are formed. R* (carbon centered radical formed by H-abstraction) will quickly react with ground state molecular oxygen, O_2, forming chain-initiating, oxygen-centered radicals, which further react to form hydroperoxides by hydrogen abstraction and thus open a second cycle. Antioxidants can be introduced to induce termination steps for autoxidation, forming stable radicals that suppress the autoxidation cycles.[175,233,234] Guo et al. reported the positive effects of several common stabilizers on the environmental stability of NFA films and OSCs. Selected stabilizers S1-S6 (see **Figure 17b** for molecular structures) were firstly added to ITIC pristine films with a concentration of 2 wt%, followed by continuous irradiation of the NFA films under light in air. As shown by the bleaching of the absorbance spectra over degradation time (**Figure 17c**), all the additive doped ITIC films exhibited improved stability than the pristine film, with S6 (a nickel chelate) the best quencher of ROS among these six stabilizers. Then S6 was introduced to a wider range of NFA as a stabilizer, including IDIC, IT-4F and O-IDTBR, at the same concentration of 2 wt% as ITIC. Photo-oxidation studies of these S6-doped NFA films reveal the beneficial role of S6 in protecting all the investigated NFA films against photochemical degradation (**Figure 17d**), suggesting the use of stabilizers as a general strategy for the stability enhancement of NFA OSCs. The role of S6 in improving the photochemical stability of NFA OSCs was further demonstrated by the degradation studies of the unencapsulated J71:ITIC OSCs (employing 2wt% of S6) under one sun illumination in air. While the introduction of S6 induced a slight decrease of initial PCE together with lower J_{sc} and FF due to increased trap-assisted recombination, the normalized PCE (**Figure 17e**) shows that the S6 doped devices exhibit higher stability under light and oxygen compared to the ones without S6. The findings further indicate that additional research efforts are needed to further optimize the choice and processing conditions of stabilizers in order to overcome the challenge in enhancing the stability of NFA OSCs without compromising their performance.[175]

3.2.2. Interfacial stability

As discussed above, the reaction between NFA materials and commonly used interlayers such as PEDOT:PSS and ZnO aggravated the device degradation. To address such problems, several research attempts have been made to avoid the direct reaction of the interactional layers. For example, in addition to the commonly used MoO_3 interlayer,[68] the ZnO/polymer bilayer ETL concept was proposed for an efficient and stable inverted structure of NFA OSC by Park et al.[235] Two types of quarterthiophene-containing polyimides (PIs) were synthesized based on the different moieties of pyromellitic dianhydride (PMDA) and cyclobutane-1,2,3,4-tetracarboxylic dianhydride (CTCDA), which were used as an additional layer on ZnO. Interestingly, improved efficiency and stability were found to be dependent on the conformation of polyimides; the performance was enhanced by the PMDA-PI with a stretched chain structure but degraded by the CTCDA-PI with a bended chain structure. Surface modification of ZnO with self-assembled monolayers (SAMs) is also a good strategy to promote interfacial stability in inverted NFA OSCs. Liu et al. developed SAMs with different functionalized end groups.[236] The self-assembly of the SAM molecules on ZnO induces the molecular dipole at the surface and thereby allows the effective modulation of energy levels, which brings the advantage of performance improvement. In addition, ZnO/SAM hybrid ETL supports the prolonged photostability of NFA OSCs, which is attributed to the passivation of photocatalytic activities of ZnO by SAM. In a further effort to stabilize ZnO/BHJ heterointerfaces, a fullerene functionalized SAM (C_{60}-SAM) has also been utilized by Xu et al. to passivate ZnO surface.[193] The C_{60}-SAM has a dual function; it not only suppresses the charge recombination via surface trap passivation, but also stabilizes the BHJ morphology by reducing the surface energy of ZnO for better wetting of the active layer. Notably, under one sun illumination condition, an extrapolated T_{80} lifetime of 34,000 hours was achieved for the OSCs with inverted device structure of ITO/ZnO/C_{60}-SAM/PTB7-Th:IEICO-4F/MoO_3/Ag. Given an estimated solar irradiance of 1500 kWh/(m^2 year), this is equivalent to 22 years of estimated lifetime. Another important method is modifying ZnO with doping elements. The PTB7-Th:IT-4F device maintained more than 80% of their initial efficiency after 1000 h storage in the dark upon using the lithium modified ZnO electron transport layer. Li atoms replace zinc interstitials (Zn_i)

defects, thereby passivating them, prohibiting the adsorption of corrosive agents and boosting the stability of the Li-modified ZnO-based OSCs.[237] It is further found that the interfacial chemical reaction is found to be more severe in OSCs with a conventional device structure of glass/ITO/PEDOT:PSS/active-layer/ZnO/Ag than that with an inverted device structure of (glass/ITO/ZnO/active layer/MoO_3/Ag) owing to the high sensitivity of the INCN moieties in the ITIC molecule to acidic environment as well as the acidic nature of PEDOT:PSS.[68][238] Such interfacial chemical reaction can be effectively mitigated through the use of alternative interlayer materials to PEDOT:PSS, development of neutral analogues and introduction of barrier layers.[238] These findings highlight that careful engineering of the whole device architecture, not only limited to the BHJ, is required for addressing the degradation mechanisms and achieving superior long-term stability of NFA OSCs.

In contrast to the other intrinsic degradation mechanisms, interfacial instability is also associated with external sources, which are possibly originated from the degradation of interlayer and/or interfacial contact properties at the interfaces between constituent layers.[239–244] Seo et al. demonstrated hybrid ETL by mixing poly(2-ethyl-2-oxazoline) (PEOz) into the ZnO precursor solution.[245] Importantly, ZnO:PEOz film with a nano-crater morphology at the surface enables the formation of mechanically interlocking interfaces, which enhances adhesion with PBDB-T:ITIC BHJ layer and thereby prolongs device lifetime under continuous illumination. Recently, the same group developed sulfur/nitrogen-enriched polyimide as a stable interlayer for inverted NFA OSCs.[246] The presence of interlayer could effectively compensate the oxygen deficiency in ZnO to protect the organic molecules from reactive oxygen, stabilizing the ZnO/BHJ heterointerfaces. Based on this view, replacing and modifying the electrode with more stable materials can be valid methods toward stable OSCs, such as the PEDOT:PSS:S-silver nanowires (AgNMs) electrode, Cu grid/graphene hybrid electrode and Al/Ag double-layer electrode.[174,247]

3.2.3. Morphology

The thermal and light induced morphology instability is another important factor that leads to OSC device degradation. Different strategies can be adopted in order to stabilize the active layer, with examples like thermal annealing, solvent annealing and additive loading or fabrication of ternary OCSs, which will be illustrated in detail in this section.

Thermal treatments: One of the most readily available strategies to tune and stabilize BHJ morphology is through thermal annealing of the D-A blend. In particular, the boundary amorphous region between D and A domains seems to be the main target to control for better OSCs stability, as analyzed by Du et al.[248] In fact, in the process of light-induced phase segregation of BHJ, the relatively large size of ITIC-like acceptors determines low molecular diffusivity and slow migration dynamics. In the amorphous mixed D-A interfacial region, this results in the formation of small isolated NFA nano-aggregates during polymer reorganization, which don't contribute to percolation pathways for charge extraction. This is brought forward as the main origin of FF and J_{SC} losses in PM6:IT-4F solar cells. The mechanisms is intrinsically different from light-induced segregation in fullerene counterparts, in which the small PCBM molecules move out of the polymer matrix in larger clusters, affecting mostly photocurrent generation but without creation of morphological traps. In this context, the initial improvement of photoactive layer quality by processing optimization is crucial to achieve a robust blend morphology towards these processes. For example, thermal annealing over 150°C or using solvent additive processing can aid the formation of more ordered and neater boundary regions less sensitive to photo-induced reorganization. This specific regime of diffusion-limited crystallization typical for calamitic NFA,[196] possibly further assisted by the mutual π-π interactions, is also the key origin for the superior thermal stability of fullerene-free OSCs. In fact, PBDB-T:ITIC blends below ≈180°C only show local morphological reorganization with the formation of nanometric clusters not deteriorating OSC operation, as opposed to the formation of detrimental large-scale fullerene aggregates.[249] Upama et al. reported that PBDB-T:ITIC blend films thermally treated at 80 °C can form an optimum blend morphology with nano-fibril pattern, which not only favors a higher dielectric constant for efficient exciton dissociation, but also superior shelf-life stability. [250]

Additive processing: Solvent additives such as 1,8-diiodooctane (DIO) is usually used to adjust the nanomorphology of active layer and further to improve the charge generation, transport and recombination. However, this method has been shown to be unfavorable for the device stability because the residual DIO, which has a slow evaporation rate, can lead to large aggregation of the photoactive layer under thermal annealing (**Figure 18a**).[251] Ye et al. demonstrated a method of removing the residual DIO additives in PBDTTT-C-T:PCBM blend system with low boiling point 'inert' solvent-methanol. After spin-coating inert solvents for the PBDTTT-C-T/PCBM system, the morphological stability is enhanced and efficiency reproducibility is increased obviously from 7.07 ±0.27% to 7.53 ± 0.12%.[252] Yu et al. developed a series of volatilizable solid additives (SAs) for NFA OSCs, which own a similar chemical structure to that of the end-groups of the A-D-A acceptor IT-4F and can be well mixed with IT-4F acting as small bridges to enhance the π-stacking between the two IT-4F molecules. More importantly (taking one of the synthesized SA-1 for example, structure see inset of **Figure 18b**), SA-1 is volatile under thermal annealing and it can vanish from the blend upon thermal treatment at 140 °C for 10 min, leaving more room for the self-assembly of IT-4F and forming a more condensed and ordered molecular arrangement. The strong π–π interaction among IT-4F molecules enable better charge transport, improving the electron mobility of IT-4F films by approximately one order of magnitude from 2.0×10^{-4} cm^2/Vs to 1.4×10^{-3} cm^2/Vs . This further simultaneously enhances J_{sc} and FF of PM6:IT-4F OSC devices, leading to an increased PCE of 13.8%, which is comparable to those using DIO as an additive (12.2%). According to the photostability study of the encapsulated devices in air under AM 1.5 illumination for 130 h (**Figure 18b**), the devices processed with SA-1 show enhanced stability in comparison to those with DIO additive. In addition, they exhibit tolerance to thickness variation of the active layer and good reproducibility. More attractively, the synthesized SAs can be used as a universal additive for a broad range of OSC blend systems based on A-D-A structured NFA, such as ITIC, ITCC, IT-2F, IT-M and IEICO, with an improvement in active layer morphology and device performance and stability analogous to that of PBDB-T:IT-4F devices observed in all of these A-D-A acceptor based OSC devices.[253] Other alternative additives to replace DIO have also been developed, with numerous materials including lower boiling point additives, polymer additives and small molecule additives.[247,254]

Among them, the non-volatile additives can both enhance the morphological stability and mechanical stability by constructing structural stabilization in the active layer,[255] even though the morphological stability and device ductility are usually anticorrelated, and more stretchable device is likely to be less stable.[197] For example, Han et al. proposed a universal method through the construction of insulating poly(aryl ether) (PAE) matrices in the active layer. Typical PAE resins, such as poly(aryl ether ketone) containing furan moiety (PAEF) and poly(aryl ether nitrile) (PAEN), possess a highly twisted stiff backbone without any side chains (see **Figure 19a**) to simultaneously obtain high T_g, thermal stability and heat-resistant properties.[255] When a controlled amount of PAEF resin (0 to 30%) is introduced to benchmark PM6/Y6 OSCs, charge transfer can occur across the PAEF matrices in the active layer by the tunneling effect without changing the charge transport channels. The resulting devices with 5 wt% PAEF exhibit a higher PCE of 16.13% compared to15.44% of pristine devices. Since the PAE resins own highly twisted and stiff backbone without any soft side chains, it can restrain the migration of molecular chains in the active layer and therefore result in improved device thermal stability. After heating at 85 °C in N_2-filled glovebox for 24 h without encapsulation, the PCEs of the devices with 5 wt% PAEF resin retain at 54% of its initial value, significantly higher than that for the devices without PAEF resin (PCEs drop to 33% of their initial value). In addition, the twisted polymer chains of PAE resins give a strong chain entanglement effect, preventing the chain-sliding effect of donor/acceptor molecules. Introducing the PAEF matrices into the BHJ layer can enhance the mechanical property with greatly enhanced elongation at a break strain of 25.07% (with 30 wt% PAEF), which is 4.4-fold higher than the pristine PM6/Y6 film (**Figure 19b**). The devices with 30 wt% PAEF resin also exhibit superior flexibility remaining ~73% of its initial value after bending for 500 cycles at a radius of 10 mm, while the control device only retains at ~39% of its initial value after the same bending cycle, with deep cracks observed on the film surface. To demonstrate the universality of the PAE insulting matrices, stability of the OSCs with different PAEF and PAEN resins are further investigated at 85 °C for 100 h or at room temperature for 24 days in N_2 filled glovebox. As shown in **Figure 19c-d**, the devices processed with PAE matrices also exhibit superior stability to the ones without PAE. These results demonstrate that heat-resistant PAE resins serve as supporting matrices with a tunneling effect into OSCs, thereby capable of simultaneously achieving improved device flexibility and stability without sacrificing photovoltaic performance, which may play an important role in the development of stable and flexible electronics.[255] It is found that the poly-(pentafluorostyrene) (PPFS) polymer, which possesses a high dielectric constant, can also act as a morphological locking-in agent in the PBDB-TT5:ITIC active layer, contributing to a more stable morphology. As a result, the PPFS processed device showed both enhanced thermal stability and storage stability compared to DIO processed device.[256]

D-A compatibility and ternary OCSs: Another crucial requirement to preserve a stable BHJ morphology to extend OSCs lifetime is the careful selection of compatible donor and acceptor blend components. It is shown in numerous works[176,184] that light-induced segregation of D and A domains is a typical mechanism triggered by light and heat, with major consequences on J_{sc} and FF. The selection of well-matched polymer:SM pairs is therefore determinant to maintain original device performances under light and thermal stresses. For example, the burn-in free aging pattern with only 10% PCE loss over 2000 hr for P3HT:IDTBR devices[167] is not merely due to the intrinsic chemical stability of the materials, but especially to the preservation of crystalline quality of both components upon blending with the creation of neat interfaces. This mitigates the formation of light-induced interfacial traps which negatively affect the FF. The superior chemical stability in conjunction with robustness towards trap formation and phase segregation for IDTBR derivatives is also observed for other systems, such as PffBT4T-2OD:EH-IDTBR, which shows excellent light and thermal stability with burn-in free behavior.[37] In this context, it is important to clarify the difficulty to disentangle thermal and photo-degradation on morphology, since the exposure to light would inevitably lead to a local temperature increase causing D-A domain reorganization. This is evident from recent research by Yin and collaborators,[257] showing how the introduction of a third polymeric component is crucial to control FF losses. In particular, both electron transport and heat diffusion in PBDB-T:ITIC-M and PBDB-TF:IT-4F systems are found to be improved upon addition of a secondary N2200 acceptor moiety through its long polymeric chains, limiting energetic traps and local temperature increase at the same time. N2200 is known as beneficial for thermal and light stability also in other ternary blends,[258] due to morphology optimization with fibril-like texture providing a good channel for electron transport. In general, the ternary approach is often reported as highly robust towards photodegradation, under the condition that the third component is carefully chosen to match the other two. A pioneering work from Baran et al.[102] shows that the addition of small amount of IDFBR in P3HT:IDTBR photoactive layers can penetrate in both components so that intermixed P3HT:IDFBR and IDTBR:IDFBR regions co-exist with crystalline P3HT and IDTBR domains **(Figure 20a)**. This morphological configuration and its influence on energetics not only enhance exciton lifetime and optimize the cascade effect in the ternary system, but also determine better dark and light stability with respect to the binary counterpart. However, the third moiety should not be too miscible with the host D:A blend but rather able to partially segregate, to preserve pure domains and an optimum degree of crystallinity. This crucial trade-off is demonstrated by comparing F-IXIC and Cl-IXIC embedded in J101:MeIC matrix.[259] In a process governed by the relative surface energy of the three components, Cl-IXIC is highly miscible with both J101 and MeIC, while F-IXIC mostly localizes at J101:MeIC interfaces in small pure aggregates, creating efficient pathways for exciton dissociation and transport **(Figure 20b)**. This leads to superior morphological stability, with almost 100% of PCE retained after hundreds of hours in light or at 85°C. Another recent demonstration of the beneficial effect of a third component comes from a study by Gasparini and co-workers,[260] where the addition of O-IDTBR in PM6:Y6 OSCs is not only found to result in an improvement in FF and J_{SC} of fresh devices, but also reduce the PCE loss from 40% to almost zero across more than 200 h under 1 sun illumination in nitrogen atmosphere. In this case the highly crystalline O-IDTBR is selectively mixing with Y6, which is capable of extracting the trapped carriers from both blend components.

In standard binary D-A systems, the delicate trade-off between initial intermixing and aggregation is crucial for a stable BHJ morphology. While a too finely mixed blend negatively affects stability of donor polymer, for example accelerating photo-oxidation in P3HT-based systems,[176] a high degree of segregation is detrimental to the mechanical properties of BHJ OSCs due to the scarce ductility of highly crystalline domains.[261] A ternary approach combining the polymer:NFA host with a $PC_{71}BM$ third component[261] is found to be an effective strategy to achieve balanced phase intermixing and aggregation, since small fullerene molecules can easily mix and render the blend more amorphous while preserving good carrier transport thanks to their excellent electron mobility, thereby resulting in superior robustness to bending and compressing cycles for applications in stretchable OSCs.

Other strategies for morphology stabilization: In addition to morphology optimization that is strongly dependent on the choice of NFA acceptors and their matching donors and processing conditions, several other factors are reported to have a strong impact upon the light, dark and thermal stability of NFA OSCs. For example, the donor polymer moiety is found to play a crucial rule in tuning the blend molecular packing. Recent studies show that regiorandom copolymers with lower crystallinity is beneficial for the exciton dissociation and charge carrier mobility with respect to their regioregular counterparts, resulting in significantly reduced burn-in degradation.[262] Donor polymers based on benzodifuran (BDF) units instead of the widely-explored benzodithiophene (BDT) units can also improve BHJ morphology thanks to their greater rigidity and stronger intermolecular interactions, with 90% PCE preserved after 1800h of storage in air (42% humidity) for L2:TTPT-T-4F.[263] Selective solubility and crystallization through the choice of appropriate solvents is also important to tune the blend nanomorphology through the formation of purer domains for reduced recombination and enhanced thermal stability, as is shown by An et al. for P3HT:O-IDTBR NFA OSCs that employed non-halogenated solvents (2-methylanisole) rather than chlorobenzene as the processing solvent.[35]

3.3. Lab-scale vs large-area module stability testing standards (ISOS)

To transfer OSCs technology in real-world applications, an appropriate assessment of solar cell stability in relevant degradation conditions is a paramount requirement. Whereas a general agreement on testing protocols was set in 2011 by the International Summit on Organic solar cell Stability (ISOS), the lifetime extrapolation of NFA OSCs still relies on small-scale lab-based experiments in very specific conditions so that a co-ordination within the NFA research community is urgently needed. ISOS standard[264] defines four regimes of testing conditions, namely dark storage, outdoor, indoor weathering, and thermal or solar/thermal/humidity cycling, with dark storage and indoor weathering accounting for most of the published data. To allow the largest possible number of research groups to carry out stability tests according to comparable and repeatable standards, each category is differentiated into three stages of increasing sophistication in temperature and humidity control. From basic level, requiring very little technology for environment control and measurements, to intermediate, needing source measure units, calibrated solar simulators, and further equipment available in average laboratories, up to advanced level with a thorough control of testing conditions and measuring procedures only accessible to certified labs. To allow for result reproducibility it is important to report all experimental parameters that can influence the ageing process, in particular temperature, humidity, environment, electrical load and light source. The latter can be chosen among different options, but only xenon arc or metal halide lamps with filters are recommended as able to reproduce the daylight spectrum. Fluorescence lamps with 200-1000 lx illuminance are suggested for low light stability tests to reproduce common conditions of indoor lighting. However, in the current landscape of OSCs fields every research group chooses freely the most suitable or readily available light source for their aims. To faithfully represent the effect of sunlight exposure in terms of photochemical, electrical and thermal processes, it is paramount to include all spectral components of sunlight-UV, visible and IR. Moreover, consensus should be established in the definition of reported OSCs lifetime. ISOS criteria advise to report at least the performances at four notable times: T_0, soon after fabrication, T_S, an arbitrary time marking the end of stabilization, T_{80} and T_{S80}, when 20% of initial performance is lost respectively from T_0 and T_S (see scheme in **Figure 21**). Usually T_S is considered the turning point between exponential and linear decays at the end of burn-in phase, but more rigorous consensus should be established on its definition, since its identification is currently highly qualitative. Other determinant testing conditions that need to be included in any stability report and target for further standardization are device encapsulation, contacts, active area and masking, substrate and electrode characteristics and any meaningful handling condition. In this context, the standards emerging from ISOS are quite broad and the most rigorous requirements in terms of degradation and measurement protocol are just put forward as suggestions, so that in practice every research group applies specific conditions which are still far from being comparable. In terms of light sources for lab weathering, AM1.5G spectra from xenon arc or metal halide lamps according to ISOS indications are largely used,[102,112,175,176,181,260] but also visible-only LED arrays[167,184,248,257] and UV filters[37,192,219] are commonly reported. Degradation can be performed in air[102,176] or in dry nitrogen atmosphere,[37,112,167,219,248,260,265] but also controlled amount of oxygen can be introduced[184] or a comparison between dark in air and inert in light conditions can be made to identify the main degradation process.[175] The temperature is usually reported as a range, referring to it as stable if it is kept below a threshold of "ambient" conditions – usually 30-50°C.[37,175,176,184,219,265] The testing time also depends on the specific focus of the experiment, from the scale of minutes to investigate photochemical reactions[175,181] to thousands of hours for extended lifetime studies.[112,167,184,192,248] Nevertheless, for highly stable systems T_{80} is seldom measured but rather extrapolated from the efficiency evolution.[184,193] Hereby, it should be noticed that the ISOS standardization mostly aims at assessing device lifetime (e.g. T_{80}) for industrial and commercial application, defining the reliability of photovoltaic performance. On the other hand, research on OSCs is also interested in understanding the origin of degradation mechanisms and their characteristics in different NFA-based systems, so that the use of specific light sources or environmental conditions, even if not complying with ISOS standards, can be important to investigate relevant phenomena.

In a recent work from Madsen group, stability tests with different ISOS protocols are compared[266], namely ISOS-L-2 and ISOS-O-1. The former (lab weathering) is typically employed in lab-scale experiments to elucidate photostability of promising high-efficiency blends in controlled temperature and illumination conditions, while the latter (outdoor) is mainly useful to assess robustness of large area devices suitable for scalable applications even without impressive PCE. In this study, sheet-to-sheet slot-die fabricated PBDB-T:ITIC cells with conventional architecture (typically utilized in industrial manufacturing) are tested outdoor, while spin-coated inverted-structure counterparts are degraded indoor under a solar simulator mimicking outdoor light cycle. Interestingly, it is found that ISOS-O-1 conditions result in reversible degradation mostly affecting V_{OC} and J_{SC}, while for ISOS-L-2 permanent performance decay is observed especially from FF, linearly dependent on light intensity. The authors suggest this strictly links to device architecture, with the PEDOT:PSS top layer (conventional) possibly more stable towards the light-induced interactions with the active layer occurring for MoO_3 (inverted). These interactions could result in interfacial trap state formation for inverted architecture, which negatively affect device stability. The study encourages the awareness of the connection between OSCs lifetime and experimental conditions and underlines that a poor stability in lab-designed set-ups is not in contrast with robustness of large-area devices for commercial applications.

Another crucial topic to face for extraction of meaningful stability data from experiments is the assessment of how closely the controlled conditions defined by ISOS standards mirror the on-field ageing processes in practical applications. In a review of the state-of-art on OSCs outdoor testing protocols,[267] Zhang et al. give an overview of the main points to sort out in terms of testing method to achieve a reproducible stability assessment and a clear comparison to real-world conditions. Whereas dark storage simulates quite closely the phenomena happening outdoor with main degradation mechanisms from oxygen and water penetration into devices, the extrapolation of photo-induced aging is less straightforward. Few attempts have been made to create a conversion system between different ISOS standards (like the so-called "o-diagram")[268] and to understand how they speed up real-world degradation through extreme lab conditions (defining specific "acceleration factors"),[269] but the wide variety of climate situations found in different countries makes a consistent reference frame extremely challenging, so that even outdoor testing can be not representative of general processes. The main factors to consider for lifetime extrapolation are mainly the impossibility to control the exact radiation characteristics, temperature and moisture, as well as their daily and seasonal variations in real-world conditions. Even though NFA are generally less affected by humidity and heat than fullerene counterparts, these factors modify stability patterns.[267] At the same time the increasing power density of solar radiation strongly influences J_{SC} in OSCs, from a trade-off between trap-state filling and carrier density increase.[267,270,271] In particular, outside the 800-1100 W/m^2 power density range around AM1.5G reference non-linear dependence between irradiance and performance is reported.

4. Key Challenges

In this final section, we aim to discuss the key challenges on enhancing the stability of nonfullerene acceptor based solar cells. We first discuss the origin of degradation of OCSs, and secondly show how molecular properties and device performance are fundamentally linked, then move on to discussing the key challenges.

4.1 Identifying molecular origin of degradation

The photon-to-electricity conversion process in organic molecular solar cells undergoes a few steps: (a) absorption; (b) exciton diffusion; (c) charge transfer; (d) CT state separation; (e) charge transport; (f) charge collection (see Figure 22).[3,272] The photon absorption of organic molecules depends on the size of pi-conjugation, planarity, persistence length, molecular packing, and crystallinity.[273–275] The efficiency of exciton diffusion relies on the size of donor-acceptor domain and the exciton diffusion length.[2,3] D-A domain size is mostly determined by the morphology, while the diffusion length is controlled by the lifetime of excitons hence the coupling between excited and ground states as well as by the relative probability of non-radiative decay. The rate of charge transfer, if we are under weak coupling limit, is determined by the coupling between local excited (LE) state and CT state, energetic offset between LE and CT state, and reorganization energies, according to Marcus theory.[276] The efficiency of CT exciton separation depends on the CT state lifetime,[277–279] coupling between CT state and charge separated (CS) state, delocalization of electron in acceptor or hole in donor[280] and relative availability of states. The charge transport process is determined by coupling between adjacent molecules,[281] degree of trapping and de-trapping,[282,283] and free charge carrier lifetime. Charge collection efficiency relies on the degree of interfacial defects, the size of extraction barrier, and the surface velocity.[284] In a simpler picture, we can describe those operation processes as the competition between charge transfer (or transport after free charges are generated) and recombination after photo-absorption. Charge transfer process, on one hand, involves the charge transfer from local excited state to charge transfer state (often called exciton diffusion), charge transfer from CT state to charge separated state (often called charge separation), and the charge transfer within the same molecule clusters (often called free charge carrier transport), and finally charge transfer from active materials to electrodes (often called collection). Recombination, on the other hand, undergoes the decay of local excitons (failure of forming CT states), decay of CT state excitons, and finally the decay of free charge carriers both inside the devices and at the contact interfaces.

Fundamentally, those rates of recombination and charge transfer could be determined by the molecular structure of donor and acceptor and their orientations and interactions with each other and with the environment, although accurate determination of those rates remain challenging[274]. Therefore, the change of molecular properties over time is a primary factor controlling changes in device operation, therefore the stability of organic molecular solar cells, and a link between molecular properties and device level properties is expected in the order of consequential influences: molecular properties[9,10] (photochemical stability) → morphological properties[195–197,220] (morphological stability) → device properties[198–201] (electrical stability). Here, we aim to discuss the key challenges from three main aspects: molecular design, morphology, and device physics. We also briefly comment on the practical challenges in the end.

4.2 Designing NFA molecular design structure towards improved OSCs stability

The first step towards superior stability is the intrinsic stability of molecule. In this context, the routes worth being explored are numerous, with various aspects to be taken into account such as NFA chemical structure (e.g. heteroatom substitution), molecular conformation, structural rigidity, symmetry and energetics. Even if the record-performing NFA of Y6 family still do not provide exceptional operational stability in devices,[260] recent evidences demonstrate its highly rigid structure controlled by outer core alkyl chains conformational locking.[221] This suggests an outlook of further tuning of the A-D-A-D-A molecular structure, for a thorough understanding of the role of side chains not only in boosting efficiency,[41] but also in ensuring long device lifetime. Since the alkene linkage between the donor-acceptor building blocks present in the most relevant NFA structures (IDTBR, ITIC, Y6) has been pointed out as the starting point of chemical degradation,[176] an important challenge for molecular engineering is the development of new synthetic strategies for conjugated NFA structures possibly free from this weak linkage or with powerful non-covalent bonds to stabilize it. In this context, Y6 molecular design is also interesting for 3D design opening up pathways for charge transport in multiple directions influenced by packing motifs.[285] This characteristic is particularly evident in the emerging families of 3D conjugated NFA such as the star-shaped oligomers,[286–288] where the molecular geometry can be finely tailored by the choice of specific conjugated arms to control twisting[288] and with several examples showing promising thermal stability.[286] In this aspect, a promising direction for investigation is the role of 3D transport in enhancing charge separation and making OSCs more robust towards degradation processes.

Another complementary aspect to work on for extending device lifetime is the accurate tuning of NFA energy levels through molecular structure modification. Particular attention is deserved by the LUMO, given its role in controlling degradation processes such as photo-oxidation.[181] The design of NFA with a deep LUMO is a viable way to reduce the impact of this mechanism. This can be realized without compromising charge separation thanks to the small D-A energy offset sufficient for exciton dissociation in numerous NFA-polymer blends,[279] even though donor energy levels need to be tuned accordingly to preserve a high V_{OC}.

As the organic molecules in the photoactive layer of OSCs inevitably contact the interlayer, contribution of interfacial stability may become increasingly important for determining the device lifetime. It has been found that interlayer with ionic characteristics, such as PEI and PEDOT:PSS, can react with NFA and cause chemical reaction, which eventually gives rise to the degradation of electronic properties of NFA. Based on the studies for the identification of the possible undesirable reaction, it can be suggested that interlayers should possess higher chemical inertness to passivate their chemical reactivities by substituting reactive ionic groups (mostly proton) with less reactive counterparts while maintaining charge selective functionality. From the viewpoint of NFA molecular design, the chemical stability has ample room for further improvement. Most of the state-of-the-art NFA have adopted an electron-pushing and electron-pulling alternating structural design to induce strong intramolecular charge transfer effects; A-D-A type for ITIC and IDTBR family, and A-DA′D-A type for Y6 family. The vinylene group, particularly in these molecular structures, play an important role in not only endowing the molecule with conformational flexibility, but also connecting the central core unit with electron-deficient end-group to preserve conjugation along the entire NFA molecule. However, such a bridging vinyl linkers are prone to chemical reactions and can be a trigger for degradation following exposure to reactive species. Unravelling the nature of these chemical interaction and following structural modification would be the first important step towards a realization of the chemically stable NFA.

4.3 Optimizing BHJ morphology

Another significant challenge lies in morphological stability, which is widely known to have a strong influence on the charge carrier kinetics of OSCs, including exciton dissociation, charge transport and recombination (see **Figure 22d**). It has been reported that some fullerene-based OSC systems, such as PffBT4T-2OD:PCBM, can suffer from severe burn-in degradation due to spinodal demixing of the donor and acceptor phases even under modest thermal stress, primarily caused by the low miscibility between the donor and acceptor resulting in a metastable blend morphology.[183] While such degradation may be less likely to occur at least in some NFA-based OSCs owing to their improved morphological stability than their fullerene-based counterparts,[34,168] further investigation is needed in order to establish the relationship between the morphological stability (e.g. the demixing behaviour) of NFA-based OSCs and their molecular and device design.[25]

It is established that the blend nanomorphology of OSCs is metastable and readily moves toward a thermodynamic equilibrium state, which is strongly mediated by the miscibility of the donor and acceptor.[289] There is still a lack of understanding of thermodynamic factors affecting morphology degradation of NFA-based OSCs. It should be noted that post-treatments such as thermal annealing, additive and solvent vapor annealing, may also cause the nucleation of crystallizable SMA in the initial blends. Because of the additional chemical potential of the SMA crystals, this nucleation will promote the growth of crystals, thereby forming large crystals by depleting the mixed domain over time.[224] This happens more often in photovoltaic systems where high crystallization and phase separation had occurred during the solution casting process, with further activation of the materials towards structural rearrangements going beyond the optimal morphology for charge generation and collection. Although some burn-in free NFA-based OSCs with a higher thermal and oxidative stability than the widely studied fullerene acceptors have been reported,[135][134] it is not clear whether a longer lifetime can be achieved, and whether any new hypo miscible nonfullerene SMA-based blend systems may suffer from thermodynamics driven morphology instability. Therefore, it is urgently needed to explore some strategies, together with NFA molecular design, to avoid the long-term device instability caused by the thermodynamically unstable bulk heterojunction morphology of NFA-based blend systems.

4.4 Understanding fundamental device physics

Molecular and morphological changes during a degradation process cause the reduction of device performance, which is most commonly characterized using the knowledge from device physics, for example, nonradiative voltage loss[290] (**Figure 22b**), trap states[198–201], trapping and de-trapping behavior[200,204] (**Figure 22c**). The knowledge on the device-physics level of the degradation is useful but not enough to identify the origin of the losses, since fundamentally molecular property is the origin as we discussed above. This brings up another big challenge for future stability studies, that is to develop understanding and reasoning connecting molecular properties to device properties, which would possibly serve as the key to identify major degradation mechanisms and develop the guidelines for achieving simultaneously superior efficiency and stability. For example, how much nonradiative voltage loss is caused by free charge collection relative to CT state recombination, how to quantify the density and depth of trap states by the changes of molecular property and by morphological change, and how to distinguish the loss by morphological change from molecular property changes, how to distinguish disorder of charge separated states from CT states, and other related scientific questions. With the emergence of Y-family NFA acceptors,[21,291,292] a special focus on the structure-stability relationship should be considered as one of the design rules for novel NFA acceptors. It will be a combined effort by theoretical/experimental chemists and physicist to answer these questions.

4.5 Manufacturing cost and fabrication process

Having discussed the fundamental challenges towards highly efficient and stable OSCs, here we go on to briefly discuss the practical challenges related to the fabrication of OSCs at an industrial level, and a more comprehensive discussion on this topic can be found in the recent reviews by Ma et al.[293] and Brabec et al.[294] To ensure a smooth transition from laboratory devices to industry modules, capability in the large scale synthesis of low cost materials (including active materials, substrates, interlayers, electrodes) and rapid production of large area organic thin films with good tolerance to thickness variations is required. The cost of materials remains a major hurdle to overcome on the research and development of nonfullerene OSCs toward a truly low-cost technology. For example, PM6 is currently sold at a cost ~2687 US dollars per gram, and the materials cost related to the fabrication of nonfullerene OSCs (e.g.

ITO) remains rather high.[293] Furthermore, state of the art nonfullerene OSCs usually require the addition of processing additives and/or post/pre-treatment (such as thermal annealing and solvent vapor annealing), thereby significantly compromising their compatibility with low cost and large scale industrial manufacturing. The development of low-cost materials, device architectures and processing routes is therefore urgently required before any mass production at an industrial level is carried out and should be considered equally important as the stability and efficiency of OSCs. However, the chemical versatility of NFA provides great potential for multi-objective optimization and makes NFA possible to be a class of auxiliary materials to solve the internal performance, cost and stability of a material. [294]

5. Conclusion

In this review, we have discussed the recent progress on the NFA OSCs based on critical research achievements in the stability of the devices. It has been revealed that many important factors that greatly influence the performance of the OSCs, such as NFA molecular design, BHJ morphology, and device engineering, are also found to be important in determining the device stability. In the last section, we finally suggested key challenging points to overcome for realizing highly stable OSCs. Although many challenges still remain to be resolved before widespread adoption of NFA OSCs in photovoltaics is feasible, gradual progress will bring a bright future. We hope that this review proves useful in fostering the development of the stable NFA OSCs.

Supporting Information

Supporting Information is available from the Wiley Online Library or from the author.

Acknowledgements

Y.W. and J.L. contributed equally to this work. Authors acknowledge the funding of UK Engineering and Physical Sciences Research Council (EPSRC) EP/S020748/1, Plastic Electronics Doctoral Training Center (EP/L016702/1) and the Global Research Laboratory Program of the Korean National Research Foundation (NRF) by the Ministry of Science, ICT & Future Planning (NRF-2017K1A1A2013153). J.N. and J.Y. thank the European Research Council for support under the European Union's Horizon 2020 research and innovation program (Grant Agreement No. 742708)

Conflict of Interest

The authors declare no conflict of interest.

References

[1] O. Inganäs, *Adv. Mater.* **2018**, *30*, 1800388.

[2] A. J. Heeger, *Adv. Mater.* **2014**, *26*, 10.

[3] J. Nelson, *Mater. Today* **2011**, *14*, 462.

[4] A. Köhler, H. Bässler, *Electron. Process. Org. Semicond. An Introd.* **2015**, 307.

[5] G. Yu, J. Gao, J. C. Hummelen, F. Wudl, A. J. Heeger, *Science (80-.).* **1995**, *270*, 1789.

[6] Y. Liang, Z. Xu, J. Xia, S. T. Tsai, Y. Wu, G. Li, C. Ray, L. Yu, *Adv. Mater.* **2010**, *22*, 135.

[7] S. H. Liao, H. J. Jhuo, Y. S. Cheng, S. A. Chen, *Adv. Mater.* **2013**, *25*, 4766.

[8] S. H. Park, A. Roy, S. Beaupré, S. Cho, N. Coates, J. S. Moon, D. Moses, M. Leclerc, K. Lee, A. J. Heeger, *Nat. Photonics* **2009**, *3*, 297.

[9] H. K. H. Lee, A. M. Telford, J. A. Röhr, M. F. Wyatt, B. Rice, J. Wu, A. De Castro Maciel, S. M. Tuladhar, E. Speller, J. McGettrick, J. R. Searle, S. Pont, T. Watson, T. Kirchartz, J. R. Durrant, W. C. Tsoi, J. Nelson, Z. Li, *Energy Environ. Sci.* **2018**, *11*, 417.

[10] I. E. Brumboiu, L. Ericsson, R. Hansson, E. Moons, O. Eriksson, B. Brena, *J. Chem. Phys.* **2015**, *142*, 054306.

[11] Y. Cui, Y. Wang, J. Bergqvist, H. Yao, Y. Xu, B. Gao, C. Yang, S. Zhang, O. Inganäs, F. Gao, J. Hou, *Nat. Energy* **2019**, *4*, 768.

[12] Y. Cui, H. Yao, T. Zhang, L. Hong, B. Gao, K. Xian, J. Qin, J. Hou, *Adv. Mater.* **2019**, *31*, 1904512.

[13] B. P. Lechêne, M. Cowell, A. Pierre, J. W. Evans, P. K. Wright, A. C. Arias, *Nano Energy* **2016**, *26*, 631.

[14] V. V. Brus, J. Lee, B. R. Luginbuhl, S. J. Ko, G. C. Bazan, T. Q. Nguyen, *Adv. Mater.* **2019**, *31*, 1900904.

[15] W. Wang, C. Yan, T. K. Lau, J. Wang, K. Liu, Y. Fan, X. Lu, X. Zhan, *Adv. Mater.* **2017**, *29*, 1701308.

[16] S. Holliday, Y. Li, C. K. Luscombe, **2017**, *70*, 34.

[17] H. Fu, Z. Wang, Y. Sun, *Angew. Chem. Int. Ed.* **2019**, *58*, 4442.

[18] Z. Zheng, H. Yao, L. Ye, Y. Xu, S. Zhang, J. Hou, *Mater. Today* **2020**, *35*, 115.

[19] Y. Cui, H. Yao, J. Zhang, T. Zhang, Y. Wang, L. Hong, K. Xian, B. Xu, S. Zhang, J. Peng, Z. Wei, F. Gao, J. Hou, *Nat. Commun.* **2019**, *10*, 2515.

[20] D. Qian, Z. Zheng, H. Yao, W. Tress, T. R. Hopper, S. Chen, S. Li, J. Liu, S. Chen, J. Zhang, X. K. Liu, B. Gao, L. Ouyang, Y. Jin, G. Pozina, I. A. Buyanova, W. M. Chen, O. Inganäs, V. Coropceanu, J. L. Bredas, H. Yan, J. Hou, F. Zhang, A. A. Bakulin, F. Gao, *Nat. Mater.* **2018**, *17*, 703.

[21] Q. Liu, Y. Jiang, K. Jin, J. Qin, J. Xu, W. Li, J. Xiong, J. Liu, Z. Xiao, K. Sun, S. Yang, X. Zhang, L. Ding, *Sci. Bull.* **2020**, *65*, 272.

[22] Y. Lin, J. Wang, Z. G. Zhang, H. Bai, Y. Li, D. Zhu, X. Zhan, *Adv. Mater.* **2015**, *27*, 1170.

[23] L. Gao, Z. G. Zhang, H. Bin, L. Xue, Y. Yang, C. Wang, F. Liu, T. P. Russell, Y. Li, *Adv. Mater.* **2016**, *28*, 8288.

[24] Y. Qin, M. A. Uddin, Y. Chen, B. Jang, K. Zhao, Z. Zheng, R. Yu, T. J. Shin, H. Y. Woo, J. Hou, *Adv. Mater.* **2016**, *28*, 9416.

[25] W. Zhao, D. Qian, S. Zhang, S. Li, O. Inganäs, F. Gao, J. Hou, *Adv. Mater.* **2016**, 4734.

[26] H. Bin, L. Gao, Z. G. Zhang, Y. Yang, Y. Zhang, C. Zhang, S. Chen, L. Xue, C. Yang, M. Xiao, Y. Li, *Nat. Commun.* **2016**, *7*, 13651.

[27] X. Xu, T. Yu, Z. Bi, W. Ma, Y. Li, Q. Peng, *Adv. Mater.* **2018**, *30*, 1703973.

[28] Y. Lin, F. Zhao, Q. He, L. Huo, Y. Wu, T. C. Parker, W. Ma, Y. Sun, C. Wang, D. Zhu, A. J. Heeger, S. R. Marder, X. Zhan, *J. Am. Chem. Soc.* **2016**, *138*, 4955.

[29] Y. Yang, Z. G. Zhang, H. Bin, S. Chen, L. Gao, L. Xue, C. Yang, Y. Li, *J. Am. Chem. Soc.* **2016**, *138*, 15011.

[30] H. Yao, L. Ye, J. Hou, B. Jang, G. Han, Y. Cui, G. M. Su, C. Wang, B. Gao, R. Yu, H. Zhang, Y. Yi, H. Y. Woo, H. Ade, J. Hou, *Adv. Mater.* **2017**, *29*, 1700254.

[31] S. Li, L. Ye, W. Zhao, S. Zhang, S. Mukherjee, H. Ade, J. Hou, *Adv. Mater.* **2016**, *28*, 9423.

[32] W. Li, L. Ye, S. Li, H. Yao, H. Ade, J. Hou, *Adv. Mater.* **2018**, *30*, 1707170.

[33] S. Holliday, R. S. Ashraf, A. Wadsworth, D. Baran, S. A. Yousaf, C. B. Nielsen, C. H. Tan, S. D. Dimitrov, Z. Shang, N. Gasparini, M. Alamoudi, F. Laquai, C. J. Brabec, A. Salleo, J. R. Durrant, I. McCulloch, *Nat. Commun.* **2016**, *7*, 11585.

[34] S. Holliday, R. S. Ashraf, C. B. Nielsen, M. Kirkus, J. A. Röhr, C. H. Tan, E. Collado-Fregoso, A. C. Knall, J. R. Durrant, J. Nelson, I. McCulloch, *J. Am. Chem. Soc.* **2015**, *137*, 898.

[35] K. An, W. Zhong, L. Ying, *Org. Electron.* **2020**, *82*, 105701.

[36] S. Badgujar, C. E. Song, S. Oh, W. S. Shin, S. J. Moon, J. C. Lee, I. H. Jung, S. K. Lee, *J. Mater. Chem. A* **2016**, *4*, 16335.

[37] H. Cha, J. Wu, A. Wadsworth, J. Nagitta, S. Limbu, S. Pont, Z. Li, J. Searle, M. F. Wyatt, D. Baran, J. S. Kim, I. McCulloch, J. R. Durrant, *Adv. Mater.* **2017**, *29*, 1701156.

[38] Z. Hu, Q. Wang, Z. Wang, F. Pan, L. Zhang, Y. Cao, J. Chen, *Org. Electron.* **2020**, *83*, 105762.

[39] J. Yuan, Y. Zhang, L. Zhou, G. Zhang, H. L. Yip, T. K. Lau, X. Lu, C. Zhu, H. Peng, P. A. Johnson, M. Leclerc, Y. Cao, J. Ulanski, Y. Li, Y. Zou, *Joule* **2019**, *3*, 1140.

[40] Z. Luo, R. Sun, C. Zhong, T. Liu, G. Zhang, Y. Zou, X. Jiao, J. Min, C. Yang, *Sci. China Chem.* **2020**, *63*, 361.

[41] K. Jiang, Q. Wei, J. Y. L. Lai, Z. Peng, H. K. Kim, J. Yuan, L. Ye, H. Ade, Y. Zou, H. Yan, *Joule* **2019**, *3*, 3020.

[42] B. Kan, H. Feng, H. Yao, M. Chang, X. Wan, C. Li, J. Hou, Y. Chen, *Sci. China Chem.* **2018**, *61*, 1307.

[43] W. Zhao, S. Li, H. Yao, S. Zhang, Y. Zhang, B. Yang, J. Hou, *J. Am. Chem. Soc.* **2017**, *139*, 7148.

[44] Y. Cui, H. Yao, L. Hong, T. Zhang, Y. Tang, B. Lin, K. Xian, B. Gao, C. An, P. Bi, W. Ma, J. Hou, *Natl. Sci. Rev.* **2019**, *7*, 1239.

[45] Y. Cui, H. Yao, J. Zhang, K. Xian, T. Zhang, L. Hong, Y. Wang, Y. Xu, K. Ma, C. An, C. He, Z. Wei, F. Gao, J. Hou, *Adv. Mater.* **2020**, *32*, 1908205.

[46] S. Mori, T. Gotanda, Y. Nakano, M. Saito, K. Todori, M. Hosoya, *Jpn. J. Appl. Phys.* **2015**, *54*, 7.

[47] C. Yan, S. Barlow, Z. Wang, H. Yan, A. K. Y. Jen, S. R. Marder, X. Zhan, *Nat. Rev. Mater.* **2018**, *3*, 18003.

[48] S. V Dayneko, M. Pahlevani, G. C. Welch, *ACS Appl. Mater. Interfaces* **2019**, *11*, 46017.

[49] Z. Ding, R. Zhao, Y. Yu, J. Liu, *J. Mater. Chem. A* **2019**, *7*, 26533.

[50] Y. Cui, C. Yang, H. Yao, J. Zhu, Y. Wang, G. Jia, F. Gao, **2017**, *29*, 1703080.

[51] Y. Li, J. D. Lin, X. Che, Y. Qu, F. Liu, L. S. Liao, S. R. Forrest, *J. Am. Chem. Soc.* **2017**, *139*, 17114.

[52] T. Li, S. Dai, Z. Ke, L. Yang, J. Wang, C. Yan, W. Ma, **2018**, *30*, 1705969.

[53] F. Liu, Z. Zhou, C. Zhang, J. Zhang, Q. Hu, T. Vergote, F. Liu, T. P. Russell, X. Zhu, **2017**, *29*, 1606574.

[54] J. Chen, G. Li, Q. Zhu, X. Guo, Q. Fan, W. Ma, M. Zhang, *J. Mater. Chem. A* **2019**, *7*, 3745.

[55] R. Po, C. Carbonera, A. Bernardi, N. Camaioni, *Energy Environ. Sci.* **2011**, *4*, 285.

[56] M. Graetzel, R. A. J. Janssen, D. B. Mitzi, E. H. Sargent, *Nature* **2012**, *488*, 304.

[57] M. Fahlman, S. Fabiano, V. Gueskine, D. Simon, M. Berggren, X. Crispin, *Nat. Rev. Mater.* **2019**, *4*, 627.

[58] H. Ma, H. L. Yip, F. Huang, A. K. Y. Jen, *Adv. Funct. Mater.* **2010**, *20*, 1371.

[59] H.-L. Yip, A. K.-Y. Jen, *Energy Environ. Sci.* **2012**, *5*, 5994.

[60] C. C. Chueh, C. Z. Li, A. K. Y. Jen, *Energy Environ. Sci.* **2015**, *8*, 1160.

[61] C. V. Hoven, A. Garcia, G. C. Bazan, T. Q. Nguyen, *Adv. Mater.* **2008**, *20*, 3793.

[62] H. Jiang, P. Taranekar, J. R. Reynolds, K. S. Schanze, *Angew. Chemie - Int. Ed.* **2009**, *48*, 4300.

[63] H. Ishii, K. Sugiyama, E. Ito, K. Seki, *Adv. Mater.* **1999**, *11*, 605.

[64] A. Duarte, K. Y. Pu, B. Liu, G. C. Bazan, *Chem. Mater.* **2011**, *23*, 501.

[65] Y. Zhou, C. Fuentes-Hernandez, J. Shim, J. Meyer, A. J. Giordano, H. Li, P. Winget, T. Papadopoulos, H. Cheun, J. Kim, M. Fenoll, A. Dindar, W. Haske, E. Najafabadi, T. M. Khan, H. Sojoudi, S. Barlow, S. Graham, J. L. Brédas, S. R. Marder, A. Kahn, B. Kippelen, *Science (80-.).* **2012**, *336*, 327.

[66] H. Kang, S. Hong, J. Lee, K. Lee, *Adv. Mater.* **2012**, *24*, 3005.

[67] L. Hu, Y. Liu, L. Mao, S. Xiong, L. Sun, N. Zhao, F. Qin, Y. Jiang, Y. Zhou, *J. Mater. Chem. A* **2018**, *6*, 2273.

[68] Y. Wang, W. Lan, N. Li, Z. Lan, Z. Li, J. Jia, F. Zhu, *Adv. Energy Mater.* **2019**, *9*, 1900157.

[69] Y. Wang, J. Han, L. Cai, N. Li, Z. Li, F. Zhu, *J. Mater. Chem. A* **2020**, *8*, 21255.

[70] S. Xiong, L. Hu, L. Hu, L. Sun, F. Qin, X. Liu, M. Fahlman, Y. Zhou, *Adv. Mater.* **2019**, *31*, 1806616.

[71] K. T. Huang, C. C. Shih, H. Y. Liu, D. Murakami, R. Kanto, C. T. Lo, H. Mori, C. C. Chueh, W. C. Chen, *ACS Appl. Mater. Interfaces* **2018**, *10*, 44741.

[72] M. Lv, S. Li, J. J. Jasieniak, J. Hou, J. Zhu, Z. Tan, S. E. Watkins, Y. Li, X. Chen, *Adv. Mater.* **2013**, *25*, 6889.

[73] Z. G. Zhang, B. Qi, Z. Jin, D. Chi, Z. Qi, Y. Li, J. Wang, *Energy Environ. Sci.* **2014**, *7*, 1966.

[74] S. Wang, Z. Li, X. Xu, M. Zhang, G. Zhang, Y. Li, Q. Peng, *J. Mater. Chem. A* **2018**, *6*, 22503.

[75] R. Peng, Z. Liu, Q. Guan, L. Hong, W. Song, Q. Wei, P. Gao, J. Huang, X. Fan, M. Wang, Z. Ge, *J. Mater. Chem. A* **2018**, *6*, 6327.

[76] C. Sun, Z. Wu, Z. Hu, J. Xiao, W. Zhao, H. W. Li, Q. Y. Li, S. W. Tsang, Y. X. Xu, K. Zhang, H. L. Yip, J. Hou, F. Huang, Y. Cao, *Energy Environ. Sci.* **2017**, *10*, 1784.

[77] Q. Kang, L. Ye, B. Xu, C. An, S. J. Stuard, S. Zhang, H. Yao, H. Ade, J. Hou, *Joule* **2019**, *3*, 227.

[78] Y. Liu, M. D. Cole, Y. Jiang, P. Y. Kim, D. Nordlund, T. Emrick, T. P. Russell, *Adv. Mater.* **2018**, *30*, 1705976.

[79] Z. Chen, Z. Hu, Z. Wu, X. Liu, Y. Jin, M. Xiao, F. Huang, Y. Cao, *J. Mater. Chem. A* **2017**, *5*, 19447.

[80] K. Zhao, L. Ye, W. Zhao, S. Zhang, H. Yao, B. Xu, M. Sun, J. Hou, *J. Mater. Chem. C* **2015**, *3*, 9565.

[81] W. Xu, C. Yan, Z. Kan, Y. Wang, W. Y. Lai, W. Huang, *ACS Appl. Mater. Interfaces* **2016**, *8*, 14293.

[82] Z. Wu, C. Sun, S. Dong, X. F. Jiang, S. Wu, H. Wu, H. L. Yip, F. Huang, Y. Cao, *J. Am. Chem. Soc.* **2016**, *138*, 2004.

[83] Z. Hu, Z. Chen, K. Zhang, N. Zheng, R. Xie, X. Liu, X. Yang, F. Huang, Y. Cao, *Sol. RRL* **2017**, *1*, 1700055.

[84] T. Jia, C. Sun, R. Xu, Z. Chen, Q. Yin, Y. Jin, H. L. Yip, F. Huang, Y. Cao, *ACS Appl. Mater. Interfaces* **2017**, *9*, 36070.

[85] Y. Liu, V. V. Duzhko, Z. A. Page, T. Emrick, T. P. Russell, *Acc. Chem. Res.* **2016**, *49*, 2478.

[86] C. Song, X. Liu, X. Li, Y. C. Wang, L. Wan, X. Sun, W. Zhang, J. Fang, *ACS Appl. Mater. Interfaces* **2018**, *10*, 14986.

[87] J. Yao, B. Qiu, Z. G. Zhang, L. Xue, R. Wang, C. Zhang, S. Chen, Q. Zhou, C. Sun, C. Yang, M. Xiao, L. Meng, Y. Li, *Nat. Commun.* **2020**, *11*, 1.

[88] Y. Jiang, L. Sun, F. Jiang, C. Xie, L. Hu, X. Dong, F. Qin, T. Liu, L. Hu, X. Jiang, Y. Zhou, *Mater. Horizons* **2019**, *6*, 1438.

[89] B. Xu, J. Hou, *Adv. Energy Mater.* **2018**, *8*, 1800022.

[90] C. K. Mai, H. Zhou, Y. Zhang, Z. B. Henson, T. Q. Nguyen, A. J. Heeger, G. C. Bazan, *Angew. Chemie - Int. Ed.* **2013**, *52*, 12874.

[91] H. Zhou, Y. Zhang, C. K. Mai, S. D. Collins, T. Q. Nguyen, G. C. Bazan, A. J. Heeger, *Adv. Mater.* **2014**, *26*, 780.

[92] H. Zhou, Y. Zhang, C. K. Mai, J. Seifter, T. Q. Nguyen, G. C. Bazan, A. J. Heeger, *ACS Nano* **2015**, *9*, 371.

[93] B. H. Lee, J. H. Lee, S. Y. Jeong, S. B. Park, S. H. Lee, K. Lee, *Adv. Energy Mater.* **2015**, *5*, 1401653.

[94] J. H. Lee, B. H. Lee, S. Y. Jeong, S. B. Park, G. Kim, S. H. Lee, K. Lee, *Adv. Energy Mater.* **2015**, *5*, 1501292.

[95] Y. Cui, B. Xu, B. Yang, H. Yao, S. Li, J. Hou, *Macromolecules* **2016**, *49*, 8126.

[96] C. G. Tang, M. C. Y. Ang, K. K. Choo, V. Keerthi, J. K. Tan, M. N. Syafiqah, T. Kugler, J. H. Burroughes, R. Q. Png, L. L. Chua, P. K. H. Ho, *Nature* **2016**, *539*, 536.

[97] J. H. Lee, S. Y. Jeong, G. Kim, B. Park, J. Kim, S. Kee, B. Kim, K. Lee, *Adv. Funct. Mater.* **2018**, *28*, 1705079.

[98] Y. Cui, G. Jia, J. Zhu, Q. Kang, H. Yao, L. Lu, B. Xu, J. Hou, *Chem. Mater.* **2018**, *30*, 1078.

[99] L. Lu, Q. Liao, Y. Zu, Y. Xu, B. Xu, J. Hou, *Adv. Energy Mater.* **2019**, *9*, 1803826.

[100] Y. Lin, B. Adilbekova, Y. Firdaus, E. Yengel, H. Faber, M. Sajjad, X. Zheng, E. Yarali, A. Seitkhan, O. M. Bakr, A. El-Labban, U. Schwingenschlögl, V. Tung, I. McCulloch, F. Laquai, T. D. Anthopoulos, *Adv. Mater.* **2019**, *31*, 1902965.

[101] L. M. Kozycz, D. Gao, J. Hollinger, D. S. Seferos, *Macromolecules* **2012**, *45*, 5823.

[102] D. Baran, R. S. Ashraf, D. A. Hanifi, M. Abdelsamie, N. Gasparini, J. A. Röhr, S. Holliday, A. Wadsworth, S. Lockett, M. Neophytou, C. J. M. Emmott, J. Nelson, C. J. Brabec, A. Amassian, A. Salleo, T. Kirchartz, J. R. Durrant, I. McCulloch, *Nat. Mater.* **2017**, *16*, 363.

[103] J. Wang, J. Peng, X. Liu, Z. Liang, *ACS Appl. Mater. Interfaces* **2017**, *9*, 20704.

[104] P. Xue, Y. Xiao, T. Li, S. Dai, B. Jia, K. Liu, J. Wang, X. Lu, R. P. S. Han, X. Zhan, *J. Mater. Chem. A* **2018**, *6*, 24210.

[105] X. Du, Y. Yuan, L. Zhou, H. Lin, C. Zheng, J. Luo, Z. Chen, S. Tao, L. S. Liao, *Adv. Funct. Mater.* **2020**, *30*, 1909837.

[106] M. Xiao, K. Zhang, S. Dong, Q. Yin, Z. Liu, L. Liu, F. Huang, Y. Cao, *ACS Appl. Mater. Interfaces* **2018**, *10*, 25594.

[107] Q. An, F. Zhang, W. Gao, Q. Sun, M. Zhang, C. Yang, J. Zhang, *Nano Energy* **2018**, *45*, 177.

[108] L. Duan, X. Meng, Y. Zhang, H. Yi, K. Jin, F. Haque, C. Xu, Z. Xiao, L. Ding, A. Uddin, *Mater. Chem. Front.* **2019**, *3*, 1085.

[109] N. Y. Doumon, F. V. Houard, J. Dong, P. Christodoulis, M. V. Dryzhov, G. Portale, L. J. A. Koster, *J. Mater. Chem. C* **2019**, *7*, 5104.

[110] H. Fu, C. Li, P. Bi, X. Hao, F. Liu, Y. Li, Z. Wang, Y. Sun, *Adv. Funct. Mater.* **2019**, *29*, 1807006.

[111] H. Shi, R. Xia, G. Zhang, H. L. Yip, Y. Cao, *Adv. Energy Mater.* **2019**, *9*, 1.

[112] Y. Zhu, A. Gadisa, Z. Peng, M. Ghasemi, L. Ye, Z. Xu, S. Zhao, H. Ade, *Adv. Energy Mater.* **2019**, *9*, 1900376.

[113] J. Lee, J. H. Lee, H. Yao, H. Cha, S. Hong, S. Lee, J. Kim, J. R. Durrant, J. Hou, K. Lee, *J. Mater. Chem. A* **2020**, *8*, 6682.

[114] J. Gilot, M. M. Wienk, R. A. J. Janssen, *Adv. Mater.* **2010**, *22*, 67.

[115] L. Dou, J. You, J. Yang, C. C. Chen, Y. He, S. Murase, T. Moriarty, K. Emery, G. Li, Y. Yang, *Nat. Photonics* **2012**, *6*, 180.

[116] T. Ameri, N. Li, C. J. Brabec, *Energy Environ. Sci.* **2013**, *6*, 2390.

[117] I. Etxebarria, J. Ajuria, R. Pacios, *Org. Electron.* **2015**, *19*, 34.

[118] G. Li, W. H. Chang, Y. Yang, *Nat. Rev. Mater.* **2017**, *2*, 17043.

[119] S. Lu, H. Lin, S. Zhang, J. Hou, W. C. H. Choy, *Adv. Energy Mater.* **2017**, *7*, 1701164.

[120] W. Huang, S. Y. Chang, P. Cheng, D. Meng, B. Zhu, S. Nuryyeva, C. Zhu, L. Huo, Z. Wang, M. Wang, Y. Yang, *Nano Lett.* **2018**, *18*, 7977.

[121] B. Guo, W. Li, G. Luo, X. Guo, H. Yao, M. Zhang, J. Hou, Y. Li, W. Y. Wong, *ACS Energy Lett.* **2018**, *3*, 2566.

[122] W. Zeng, C. Xie, W. Wang, S. Li, X. Jiang, S. Xiong, L. Sun, F. Qin, H. Han, Y. Zhou, *Sol. RRL* **2020**, *4*, 1900480.

[123] L. Meng, Y. Zhang, X. Wan, C. Li, X. Zhang, Y. Wang, X. Ke, Z. Xiao, L. Ding, R. Xia, H. L. Yip, Y. Cao, Y. Chen, *Science (80-.).* **2018**, *361*, 1094.

[124] M. B. Salim, R. Nekovei, R. Jeyakumar, *Sol. Energy* **2020**, *198*, 160.

[125] J. You, L. Dou, K. Yoshimura, T. Kato, K. Ohya, T. Moriarty, K. Emery, C. C. Chen, J. Gao, G. Li, Y. Yang, *Nat. Commun.* **2013**, *4*, 1446.

[126] J. Lee, H. Kang, S. Kee, S. H. Lee, S. Y. Jeong, G. Kim, J. Kim, S. Hong, H. Back, K. Lee, *ACS Appl. Mater. Interfaces* **2016**, *8*, 6144.

[127] Z. Zheng, S. Zhang, J. Zhang, Y. Qin, W. Li, R. Yu, Z. Wei, J. Hou, *Adv. Mater.* **2016**, *28*, 5133.

[128] S. C. Chen, Q. Zheng, Z. Yin, D. Cai, Y. Ma, *Org. Electron.* **2017**, *47*, 79.

[129] S. Chen, G. Zhang, J. Liu, H. Yao, J. Zhang, T. Ma, Z. Li, H. Yan, *Adv. Mater.* **2017**, *29*, 1604231.

[130] W. Liu, S. Li, J. Huang, S. Yang, J. Chen, L. Zuo, M. Shi, X. Zhan, C. Z. Li, H. Chen, *Adv. Mater.* **2016**, *28*, 9729.

[131] Y. Qin, Y. Chen, Y. Cui, S. Zhang, H. Yao, J. Huang, W. Li, Z. Zheng, J. Hou, *Adv. Mater.* **2017**, *29*, 1606340.

[132] L. Zuo, J. Yu, X. Shi, F. Lin, W. Tang, A. K. Y. Jen, *Adv. Mater.* **2017**, *29*, 1702547.

[133] Y. Cui, H. Yao, B. Gao, Y. Qin, S. Zhang, B. Yang, C. He, B. Xu, J. Hou, *J. Am. Chem. Soc.* **2017**, *139*, 7302.

[134] Y. Zhang, B. Kan, Y. Sun, Y. Wang, R. Xia, X. Ke, Y. Q. Q. Yi, C. Li, H. L. Yip, X. Wan, Y. Cao, Y. Chen, *Adv. Mater.* **2018**, *30*, 1707508.

[135] G. Liu, J. Jia, K. Zhang, X. Jia, Q. Yin, W. Zhong, L. Li, F. Huang, Y. Cao, *Adv. Energy Mater.* **2019**, *9*, 1803657.

[136] Y. Firdaus, Q. He, Y. Lin, F. A. A. Nugroho, V. M. Le Corre, E. Yengel, A. H. Balawi, A. Seitkhan, F. Laquai, C. Langhammer, F. Liu, M. Heeney, T. D. Anthopoulos, *J. Mater. Chem. A* **2020**, *8*, 1164.

[137] C. Zuo, L. Ding, *J. Mater. Chem. A* **2015**, *3*, 9063.

[138] Y. Liu, Z. Hong, Q. Chen, W. Chang, H. Zhou, T. Bin Song, E. Young, Y. Yang, J. You, G. Li, Y. Yang, *Nano Lett.* **2015**, *15*, 662.

[139] J. Kim, G. Kim, H. Back, J. Kong, I. W. Hwang, T. K. Kim, S. Kwon, J. H. Lee, J. Lee, K. Yu, C. L. Lee, H. Kang, K. Lee, *Adv. Mater.* **2016**, *28*, 3159.

[140] Y. Liu, Y. Chen, *Adv. Mater.* **2020**, *32*, 1805843.

[141] W. Shockley, H. J. Queisser, *J. Appl. Phys.* **1961**, *32*, 510.

[142] Z. Yang, A. Rajagopal, A. K. Y. Jen, *Adv. Mater.* **2017**, *29*, 1704418.

[143] X. Zhou, L. Zhang, X. Wang, C. Liu, S. Chen, M. Zhang, X. Li, W. Yi, B. Xu, *Adv. Mater.* **2020**, *32*, 1908107.

[144] Y. Zhang, W. Yu, W. Qin, Z. Yang, D. Yang, Y. Xing, S. Liu, C. Li, *Nano Energy* **2016**, *20*, 126.

[145] S. Dong, Y. Liu, Z. Hong, E. Yao, P. Sun, L. Meng, Y. Lin, J. Huang, G. Li, Y. Yang, *Nano Lett.* **2017**, *17*, 5140.

[146] Q. Guo, H. Liu, Z. Shi, F. Wang, E. Zhou, X. Bian, B. Zhang, A. Alsaedi, T. Hayat, Z. Tan, *Nanoscale* **2018**, *10*, 3245.

[147] C. Wang, Y. Bai, Q. Guo, C. Zhao, J. Zhang, S. Hu, T. Hayat, A. Alsaedi, Z. Tan, *Nanoscale* **2019**, *11*, 3794.

[148] W. Chen, H. Sun, Q. Hu, A. B. Djurišić, T. P. Russell, X. Guo, Z. He, *ACS Energy Lett.* **2019**, *4*, 2535.

[149] M. Al-Ibrahim, H. K. Roth, U. Zhokhavets, G. Gobsch, S. Sensfuss, *Sol. Energy Mater. Sol. Cells* **2005**, *85*, 13.

[150] C. Lungenschmied, G. Dennler, H. Neugebauer, S. N. Sariciftci, M. Glatthaar, T. Meyer, A. Meyer, *Sol. Energy Mater. Sol. Cells* **2007**, *91*, 379.

[151] T. Aernouts, T. Aleksandrov, C. Girotto, J. Genoe, J. Poortmans, *Appl. Phys. Lett.* **2008**, *92*, 033306.

[152] C. N. Hoth, P. Schilinsky, S. A. Choulis, C. J. Brabec, *Nano Lett.* **2008**, *8*, 2806.

[153] F. C. Krebs, M. Jørgensen, K. Norrman, O. Hagemann, J. Alstrup, T. D. Nielsen, J. Fyenbo, K. Larsen, J. Kristensen, *Sol. Energy Mater. Sol. Cells* **2009**, *93*, 422.

[154] F. C. Krebs, *Sol. Energy Mater. Sol. Cells* **2009**, *93*, 1636.

[155] F. C. Krebs, *Sol. Energy Mater. Sol. Cells* **2009**, *93*, 394.

[156] G. Wang, M. A. Adil, J. Zhang, Z. Wei, *Adv. Mater.* **2019**, *31*, 1805089.

[157] K. S. Wienhold, V. Körstgens, S. Grott, X. Jiang, M. Schwartzkopf, S. V. Roth, P. Müller-Buschbaum, *ACS Appl. Mater. Interfaces* **2019**, *11*, 42313.

[158] D. Corzo, K. Almasabi, E. Bihar, S. Macphee, D. Rosas-Villalva, N. Gasparini, S. Inal, D. Baran, *Adv. Mater. Technol.* **2019**, *4*, 1900040.

[159] K. Chang, K. Chang, Y. Li, G. Du, M. Zhong, M. Zhong, P. Yang, P. Yang, Y. Zhu, F. He, B. Mi, X. Zhao, W. Deng, *ACS Appl. Mater. Interfaces* **2020**, *12*, 27405.

[160] Y. W. Han, S. J. Jeon, H. S. Lee, H. Park, K. S. Kim, H. W. Lee, D. K. Moon, *Adv. Energy Mater.* **2019**, *9*, 1902065.

[161] Q. Wu, J. Guo, R. Sun, J. Guo, S. Jia, Y. Li, J. Wang, J. Min, *Nano Energy* **2019**, *61*, 559.

[162] L. Ye, Y. Xiong, Q. Zhang, S. Li, C. Wang, Z. Jiang, J. Hou, W. You, H. Ade, *Adv. Mater.* **2018**, *30*, 1705485.

[163] Y. Lin, Y. Jin, S. Dong, W. Zheng, J. Yang, A. Liu, F. Liu, Y. Jiang, T. P. Russell, F. Zhang, F. Huang, L. Hou, *Adv. Energy Mater.* **2018**, *8*, 1701942.

[164] M. Zhong, M. Zhong, Y. Li, G. Du, Y. Li, Y. Li, K. Chang, T. K. Lau, X. Lu, H. Sun, X. Guo, Y. F. Guo, X. Zhao, W. Deng, *ACS Appl. Mater. Interfaces* **2020**, *12*, 25843.

[165] S. Dong, K. Zhang, T. Jia, W. Zhong, X. Wang, F. Huang, Y. Cao, *EcoMat* **2019**, *1*, e12006.

[166] R. Sun, J. Guo, Q. Wu, Z. Zhang, W. Yang, J. Guo, M. Shi, Y. Zhang, S. Kahmann, L. Ye, X. Jiao, M. A. Loi, Q. Shen, H. Ade, W. Tang, C. J. Brabec, J. Min, *Energy Environ. Sci.* **2019**, *12*, 3118.

[167] N. Gasparini, M. Salvador, S. Strohm, T. Heumueller, I. Levchuk, A. Wadsworth, J. H. Bannock, J. C. de Mello, H. J. Egelhaaf, D. Baran, I. McCulloch, C. J. Brabec, *Adv. Energy Mater.* **2017**, *7*, 1700770.

[168] W. Zhao, D. Qian, S. Zhang, S. Li, O. Inganäs, F. Gao, J. Hou, *Adv. Mater.* **2016**, *28*, 4734.

[169] J. Wade, S. Wood, D. Beatrup, M. Hurhangee, H. Bronstein, I. McCulloch, J. R. Durrant, J. S. Kim, *J. Chem. Phys.* **2015**, *142*, DOI 10.1063/1.4923197.

[170] D. Beatrup, J. Wade, L. Biniek, H. Bronstein, M. Hurhangee, J. S. Kim, I. McCulloch, J. R. Durrant, *Chem. Commun.* **2014**, *50*, 14425.

[171] L. Qin, X. Liu, X. Zhang, J. Yu, L. Yang, F. Zhao, M. Huang, K. Wang, X. Wu, Y. Li, H. Chen, K. Wang, J. Xia, X. Lu, F. Gao, Y. Yi, H. Huang, *Angew. Chemie - Int. Ed.* **2020**, *59*, 15043.

[172] S. Rafique, S. M. Abdullah, N. Badiei, J. McGettrick, K. T. Lai, N. A. Roslan, H. K. H. Lee, W. C. Tsoi, L. Li, *Org. Electron.* **2020**, *76*, 105456.

[173] A. Uddin, M. B. Upama, H. Yi, L. Duan, *Coatings* **2019**, *9*, 65.

[174] C. N. Weng, H. C. Yang, C. Y. Tsai, S. H. Chen, Y. S. Chen, C. H. Chen, K. M. Huang, H. F. Meng, Y. C. Chao, C. Y. Chang, H. W. Zan, S. F. Horng, P. C. Yu, K. W. Su, *Sol. Energy* **2020**, *199*, 308.

[175] J. Guo, Y. Wu, R. Sun, W. Wang, J. Guo, Q. Wu, X. Tang, C. Sun, Z. Luo, K. Chang, Z. Zhang, J. Yuan, T. Li, W. Tang, E. Zhou, Z. Xiao, L. Ding, Y. Zou, X. Zhan, C. Yang, Z. Li, C. J. Brabec, Y. Li, J. Min, *J. Mater. Chem. A* **2019**, *7*, 25088.

[176] J. Luke, E. M. Speller, A. Wadsworth, M. F. Wyatt, S. Dimitrov, H. K. H. Lee, Z. Li, W. C. Tsoi, I. McCulloch, D. Bagnis, J. R. Durrant, J. S. Kim, *Adv. Energy Mater.* **2019**, *9*, 1803755.

[177] Y. W. Soon, S. Shoaee, R. S. Ashraf, H. Bronstein, B. C. Schroeder, W. Zhang, Z. Fei, M. Heeney, I. McCulloch, J. R. Durrant, *Adv. Funct. Mater.* **2014**, *24*, 1474.

[178] M. Bregnhj, M. Prete, V. Turkovic, A. U. Petersen, M. B. Nielsen, M. Madsen, P. R. Ogilby, *Methods Appl. Fluoresc.* **2019**, *8*, 014001.

[179] M. Glatthaar, M. Riede, N. Keegan, K. Sylvester-Hvid, B. Zimmermann, M. Niggemann, A. Hinsch, A. Gombert, *Sol. Energy Mater. Sol. Cells* **2007**, *91*, 390.

[180] E. T. Hoke, I. T. Sachs-Quintana, M. T. Lloyd, I. Kauvar, W. R. Mateker, A. M. Nardes, C. H. Peters, N. Kopidakis, M. D. McGehee, *Adv. Energy Mater.* **2012**, *2*, 1351.

[181] E. M. Speller, A. J. Clarke, N. Aristidou, M. F. Wyatt, L. Francàs, G. Fish, H. Cha, H. K. H. Lee, J. Luke, A. Wadsworth, A. D. Evans, I. McCulloch, J. S. Kim, S. A. Haque, J. R. Durrant, S. D. Dimitrov, W. C. Tsoi, Z. Li, *ACS Energy Lett.* **2019**, *4*, 846.

[182] S. Pont, S. Osella, A. Smith, A. V. Marsh, Z. Li, D. Beljonne, J. T. Cabral, J. R. Durrant, *Chem. Mater.* **2019**, *31*, 6076.

[183] N. Li, J. D. Perea, T. Kassar, M. Richter, T. Heumueller, G. J. Matt, Y. Hou, N. S. Güldal, H. Chen, S. Chen, S. Langner, M. Berlinghof, T. Unruh, C. J. Brabec, *Nat. Commun.* **2017**, *8*, 14541.

[184] X. Du, T. Heumueller, W. Gruber, A. Classen, T. Unruh, N. Li, C. J. Brabec, *Joule* **2019**, *3*, 215.

[185] X. Cheng, J. Long, R. Wu, L. Huang, L. Tan, L. Chen, Y. Chen, *ACS Omega* **2017**, *2*, 2010.

[186] J. Xiong, Z. He, S. Zhan, B. Yang, X. Zhang, P. Cai, C. Xu, X. Xue, J. Zhang, *Curr. Appl. Phys.* **2017**, *17*, 1021.

[187] X. Zhang, B. Zhang, X. Ouyang, L. Chen, H. Wu, *J. Phys. Chem. C* **2017**, *121*, 18378.

[188] B. Xu, S. A. Gopalan, A. I. Gopalan, N. Muthuchamy, K. P. Lee, J. S. Lee, Y. Jiang, S. W. Lee, S. W. Kim, J. S. Kim, H. M. Jeong, J. B. Kwon, J. H. Bae, S. W. Kang, *Sci. Rep.* **2017**, *7*, 45079.

[189] C. Xu, P. Cai, X. Zhang, Z. Zhang, X. Xue, J. Xiong, J. Zhang, *Sol. Energy Mater. Sol. Cells* **2017**, *159*, 136.

[190] Y. Li, H. Yu, X. Huang, Z. Wu, H. Xu, *Sol. Energy Mater. Sol. Cells* **2017**, *171*, 72.

[191] M. Y. Ameen, P. Shamjid, T. Abhijith, V. S. Reddy, *Opt. Mater. (Amst).* **2018**, *75*, 491.

[192] S. Park, H. J. Son, *J. Mater. Chem. A* **2019**, *7*, 25830.

[193] X. Xu, J. Xiao, G. Zhang, L. Wei, X. Jiao, H. L. Yip, Y. Cao, *Sci. Bull.* **2020**, *65*, 208.

[194] J. Xiao, M. Ren, G. Zhang, J. Wang, D. Zhang, L. Liu, N. Li, C. J. Brabec, H. L. Yip, Y. Cao, *Sol. RRL* **2019**, *3*, 1900077.

[195] W. Li, M. Chen, Z. Zhang, J. Cai, H. Zhang, R. S. Gurney, D. Liu, J. Yu, W. Tang, T. Wang, *Adv. Funct. Mater.* **2019**, *29*, 1807662.

[196] L. Yu, D. Qian, S. Marina, F. A. A. Nugroho, A. Sharma, S. Hultmark, A. I. Hofmann, R. Kroon, J. Benduhn, D. M. Smilgies, K. Vandewal, M. R. Andersson, C. Langhammer, J. Martín, F. Gao, C. Müller, *ACS Appl. Mater. Interfaces* **2019**, *11*, 21766.

[197] M. Ghasemi, H. Hu, Z. Peng, J. J. Rech, I. Angunawela, J. H. Carpenter, S. J. Stuard, A. Wadsworth, I. McCulloch, W. You, H. Ade, *Joule* **2019**, *3*, 1328.

[198] C. H. Peters, I. T. Sachs-Quintana, J. P. Kastrop, S. Beaupré, M. Leclerc, M. D. McGehee, *Adv. Energy Mater.* **2011**, *1*, 491.

[199] T. Heumueller, W. R. Mateker, I. T. Sachs-Quintana, K. Vandewal, J. A. Bartelt, T. M. Burke, T. Ameri, C. J. Brabec, M. D. McGehee, *Energy Environ. Sci.* **2014**, *7*, 2974.

[200] J. Kong, S. Song, M. Yoo, G. Y. Lee, O. Kwon, J. K. Park, H. Back, G. Kim, S. H. Lee, H. Suh, K. Lee, *Nat. Commun.* **2014**, *5*, 5688.

[201] S. A. Gevorgyan, M. V. Madsen, B. Roth, M. Corazza, M. Hösel, R. R. Søndergaard, M. Jørgensen, F. C. Krebs, *Adv. Energy Mater.* **2016**, *6*, 1501208.

[202] N. Gasparini, A. Wadsworth, M. Moser, D. Baran, I. McCulloch, C. J. Brabec, *Adv. Energy Mater.* **2018**, *8*, 1703298.

[203] J. Wu, J. Luke, H. K. H. Lee, P. Shakya Tuladhar, H. Cha, S. Y. Jang, W. C. Tsoi, M. Heeney, H. Kang, K. Lee, T. Kirchartz, J. S. Kim, J. R. Durrant, *Nat. Commun.* **2019**, *10*, 5159.

[204] Z. M. Beiley, E. T. Hoke, R. Noriega, J. Dacuña, G. F. Burkhard, J. A. Bartelt, A. Salleo, M. F. Toney, M. D. McGehee, *Adv. Energy Mater.* **2011**, *1*, 954.

[205] J. A. Carr, S. Chaudhary, *Energy Environ. Sci.* **2013**, *6*, 3414.

[206] M. Mainville, M. Leclerc, *ACS Energy Lett.* **2020**, *5*, 1186.

[207] M. Ylikunnari, M. Välimäki, K. L. Väisänen, T. M. Kraft, R. Sliz, G. Corso, R. Po, R. Barbieri, C. Carbonera, G. Gorni, M. Vilkman, *Flex. Print. Electron.* **2020**, *5*, 14008.

[208] S. Trost, A. Behrendt, T. Becker, A. Polywka, P. Görrn, T. Riedl, *Adv. Energy Mater.* **2015**, *5*, 1500277.

[209] J. Jeong, J. Seo, S. Nam, H. Han, H. Kim, T. D. Anthopoulos, D. D. C. Bradley, Y. Kim, *Adv. Sci.* **2016**, *3*, 1.

[210] H. Sato, W. S. Binti Azmi, Y. Onaru, K. Harafuji, *Org. Electron.* **2016**, *37*, 386.

[211] F. Fungura, W. R. Lindemann, J. Shinar, R. Shinar, *Adv. Energy Mater.* **2017**, *7*, 1601420.

[212] A. Classen, T. Heumueller, I. Wabra, J. Gerner, Y. He, L. Einsiedler, N. Li, G. J. Matt, A. Osvet, X. Du, A. Hirsch, C. J. Brabec, *Adv. Energy Mater.* **2019**, *9*, 1902124.

[213] J. B. Patel, P. Tiwana, N. Seidler, G. E. Morse, O. R. Lozman, M. B. Johnston, L. M. Herz, *ACS Appl. Mater. Interfaces* **2019**, *11*, 21543.

[214] Y. Cui, H. Yao, T. Zhang, L. Hong, B. Gao, K. Xian, J. Qin, *Adv. Mater.* **2019**, *31*, 1904512.

[215] S. Park, H. Ahn, J. Y. Kim, J. B. Park, J. Kim, S. H. Im, H. J. Son, *ACS Energy Lett.* **2020**, *5*, 170.

[216] T. S. Glen, N. W. Scarratt, H. Yi, A. Iraqi, T. Wang, J. Kingsley, A. R. Buckley, D. G. Lidzey, A. M. Donald, *J. Polym. Sci. Part B Polym. Phys.* **2016**, *54*, 216.

[217] H. Usta, C. Risko, Z. Wang, H. Huang, M. K. Deliomeroglu, A. Zhukhovitskiy, A. Facchetti, T. J. Marks, *J. Am. Chem. Soc.* **2009**, *131*, 5586.

[218] E. Y. Ko, G. E. Park, J. H. Lee, H. J. Kim, D. H. Lee, H. Ahn, M. A. Uddin, H. Y. Woo, M. J. Cho, D. H. Choi, *ACS Appl. Mater. Interfaces* **2017**, *9*, 8838.

[219] N. Y. Doumon, F. V. Houard, J. Dong, H. Yao, G. Portale, J. Hou, L. J. A. Koster, *Org. Electron.* **2019**, *69*, 255.

[220] Y. Xin, G. Zeng, J. Y. Ouyang, X. Zhao, X. Yang, *J. Mater. Chem. C* **2019**, *7*, 9513.

[221] J. Wu, J. Lee, Y.-C. Chin, H. Yao, H. Cha, J. Luke, J. Hou, J.-S. Kim, J. Durrant, *Energy Environ. Sci.* **2020**, *6*, 11.

[222] Y. Liu, Z. Zhang, S. Feng, M. Li, L. Wu, R. Hou, X. Xu, X. Chen, Z. Bo, *J. Am. Chem. Soc.* **2017**, *139*, 3356.

[223] Z. Zhang, J. Yu, X. Yin, Z. Hu, Y. Jiang, J. Sun, J. Zhou, F. Zhang, T. P. Russell, F. Liu, W. Tang, *Adv. Funct. Mater.* **2018**, *28*, 1705095.

[224] W. Zhang, Z. Mao, N. Zheng, J. Zou, L. Wang, C. Wei, J. Huang, D. Gao, G. Yu, *J. Mater. Chem. C* **2016**, *4*, 9266.

[225] K. Suwa, T. Suga, K. Oyaizu, H. Segawa, H. Nishide, *MRS Commun.* **2020**, *10*, 312.

[226] V. Turkovic, M. Prete, M. Bregnhøj, L. Inasaridze, D. Volyniuk, F. A. Obrezkov, J. V. Grazulevicius, S. Engmann, H. G. Rubahn, P. A. Troshin, P. R. Ogilby, M. Madsen, *ACS Appl. Mater. Interfaces* **2019**, *11*, 41570.

[227] V. Turkovic, S. Engmann, N. Tsierkezos, H. Hoppe, M. Madsen, H. G. Rubahn, U. Ritter, G. Gobsch, *Appl. Phys. A Mater. Sci. Process.* **2016**, *122*, 255.

[228] F. M. D. Chequer, Gisele Augusto Rodrigues de Oliveira, E. R. A. Ferraz, J. C. Cardoso, M. V. B. Zanoni, D. P. de Oliveira, *Intech* **2013**, *i*, 13.

[229] H. Mohammadian-Sarcheshmeh, M. Mazloum-Ardakani, M. Rameez, S. shahbazi, E. W.-G. Diau, *J. Alloys Compd.* **2020**, 156351.

[230] H. Ban, Q. Sun, T. Zhang, H. Li, Y. Shen, M. Wang, *Sol. RRL* **2020**, *4*, 1900457.

[231] X. Xu, C. C. Chueh, Z. Yang, A. Rajagopal, J. Xu, S. B. Jo, A. K. Y. Jen, *Nano Energy* **2017**, *34*, 392.

[232] V. Turkovic, S. Engmann, N. Tsierkezos, H. Hoppe, U. Ritter, G. Gobsch, *ACS Appl. Mater. Interfaces* **2014**, *6*, 18525.

[233] M. Salvador, N. Gasparini, J. D. Perea, S. H. Paleti, A. Distler, L. N. Inasaridze, P. A. Troshin, L. Lüer, H. J. Egelhaaf, C. Brabec, *Energy Environ. Sci.* **2017**, *10*, 2005.

[234] H. J. Heller, H. R. Blattmann, *Pure Appl. Chem.* **1973**, *36*, 141.

[235] E. Park, J. Seo, H. Han, H. Kim, Y. Kim, *Adv. Sci.* **2018**, *5*, 1800331.

[236] H. Liu, Z. X. Liu, S. Wang, J. Huang, H. Ju, Q. Chen, J. Yu, H. Chen, C. Z. Li, *Adv. Energy Mater.* **2019**, *9*, 1.

[237] A. Soultati, A. Fakharuddin, E. Polydorou, C. Drivas, A. Kaltzoglou, M. I. Haider, F. Kournoutas, M. Fakis, L. C. Palilis, S. Kennou, D. Davazoglou, P. Falaras, P. Argitis, S. Gardelis, A. Kordatos, A. Chroneos, L. Schmidt-Mende, M. Vasilopoulou, *ACS Appl. Energy Mater.* **2019**, *2*, 1663.

[238] J. Cameron, P. J. Skabara, *Mater. Horizons* **2020**, *7*, 1759.

[239] M. Jørgensen, K. Norrman, S. A. Gevorgyan, T. Tromholt, B. Andreasen, F. C. Krebs, *Adv. Mater.* **2012**, *24*, 580.

[240] G. Williams, Q. Wang, H. Aziz, *Adv. Funct. Mater.* **2013**, *23*, 2239.

[241] X. Jia, Z. Jiang, X. Chen, J. Zhou, L. Pan, F. Zhu, Z. Sun, S. Huang, *ACS Appl. Mater. Interfaces* **2016**, *8*, 3792.

[242] J. M. Bjuggren, A. Sharma, D. Gedefaw, S. Elmas, C. Pan, B. Kirk, X. Zhao, G. Andersson, M. R. Andersson, *ACS Appl. Energy Mater.* **2018**, *1*, 7130.

[243] Z. Huai, L. Wang, Y. Sun, R. Fan, S. Huang, X. Zhao, X. Li, G. Fu, S. Yang, *ACS Appl. Mater. Interfaces* **2018**, *10*, 5682.

[244] J. G. Sánchez, V. S. Balderrama, M. Estrada, E. Osorio, J. Ferré-Borrull, L. F. Marsal, J. Pallarès, *Sol. Energy* **2017**, *150*, 147.

[245] J. Seo, S. Nam, H. Kim, D. D. C. Bradley, Y. Kim, *Nanoscale Horizons* **2019**, *4*, 472.

[246] D. Kim, J. Seo, C. Lee, S. Lee, H. Kim, Y. Kim, *Sol. RRL* **2019**, *3*, 1900101.

[247] L. Duan, A. Uddin, *Adv. Sci.* **2020**, *7*, 1903259.

[248] X. Du, T. Heumueller, W. Gruber, O. Almora, A. Classen, J. Qu, F. He, T. Unruh, N. Li, C. J. Brabec, *Adv. Mater.* **2020**, *32*, 1908305.

[249] X. Yang, M. Niu, P. Bi, Z. Chen, J. Liu, X. Hao, *J. Phys. Chem. C* **2018**, *122*, 9843.

[250] M. B. Upama, N. K. Elumalai, M. A. Mahmud, M. Wright, D. Wang, C. Xu, A. Uddin, *Sol. Energy Mater. Sol. Cells* **2018**, *176*, 109.

[251] B. J. Tremolet De Villers, K. A. O'Hara, D. P. Ostrowski, P. H. Biddle, S. E. Shaheen, M. L. Chabinyc, D. C. Olson, N. Kopidakis, *Chem. Mater.* **2016**, *28*, 876.

[252] L. Ye, Y. Jing, X. Guo, H. Sun, S. Zhang, M. Zhang, L. Huo, J. Hou, *J. Phys. Chem. C* **2013**, *117*, 14920.

[253] R. Yu, H. Yao, L. Hong, Y. Qin, J. Zhu, Y. Cui, S. Li, J. Hou, *Nat. Commun.* **2018**, *9*, 4645.

[254] L. Duan, N. K. Elumalai, Y. Zhang, A. Uddin, *Sol. Energy Mater. Sol. Cells* **2019**, *193*, 22.

[255] J. Han, F. Bao, D. Huang, X. Wang, C. Yang, R. Yang, X. Jian, J. Wang, X. Bao, J. Chu, *Adv. Funct. Mater.* **2020**, 2003654.

[256] J. Oh, S. Jung, M. Jeong, B. Lee, J. Lee, Y. Cho, S. M. Lee, S. Chen, Z. G. Zhang, Y. Li, C. Yang, *J. Mater. Chem. C* **2019**, *7*, 4716.

[257] H. Yin, K. L. Chiu, P. Bi, G. Li, C. Yan, H. Tang, C. Zhang, Y. Xiao, H. Zhang, W. Yu, H. Hu, X. Lu, X. Hao, S. K. So, *Adv. Electron. Mater.* **2019**, *5*, 1900497.

[258] N. Zheng, K. Mahmood, W. Zhong, F. Liu, P. Zhu, Z. Wang, B. Xie, Z. Chen, K. Zhang, L. Ying, F. Huang, Y. Cao, *Nano Energy* **2019**, *58*, 724.

[259] M. Shi, R. Sun, T. Wang, Z. Luo, J. Guo, J. Guo, C. Yang, J. Min, *Org. Electron.* **2020**, *85*, 105880.

[260] N. Gasparini, S. H. K. Paleti, J. Bertrandie, G. Cai, G. Zhang, A. Wadsworth, X. Lu, H.-L. Yip, I. McCulloch, D. Baran, *ACS Energy Lett.* **2020**, *51*, 1371.

[261] W. Huang, Z. Jiang, K. Fukuda, X. Jiao, C. R. McNeill, T. Yokota, T. Someya, *Joule* **2020**, *4*, 128.

[262] Z. Chen, Z. Hu, Y. Liang, C. Zhou, J. Xiao, G. Zhang, F. Huang, *Org. Electron.* **2020**, *85*, 105874.

[263] X. Li, K. Weng, H. S. Ryu, J. Guo, X. Zhang, T. Xia, H. Fu, D. Wei, J. Min, Y. Zhang, H. Y. Woo, Y. Sun, *Adv. Funct. Mater.* **2020**, *30*, 1906809.

[264] M. O. Reese, S. A. Gevorgyan, M. Jørgensen, E. Bundgaard, S. R. Kurtz, D. S. Ginley, D. C. Olson, M. T. Lloyd, P. Morvillo, E. A. Katz, A. Elschner, O. Haillant, T. R. Currier, V. Shrotriya, M. Hermenau, M. Riede, K. R. Kirov, G. Trimmel, T. Rath, O.

Inganäs, F. Zhang, M. Andersson, K. Tvingstedt, M. Lira-Cantu, D. Laird, C. McGuiness, S. Gowrisanker, M. Pannone, M. Xiao, J. Hauch, R. Steim, D. M. Delongchamp, R. Rösch, H. Hoppe, N. Espinosa, A. Urbina, G. Yaman-Uzunoglu, J. B. Bonekamp, A. J. J. M. Van Breemen, C. Girotto, E. Voroshazi, F. C. Krebs, *Sol. Energy Mater. Sol. Cells* **2011**, *95*, 1253.

[265] N. Y. Doumon, M. V. Dryzhov, F. V. Houard, V. M. Le Corre, A. Rahimi Chatri, P. Christodoulis, L. J. A. Koster, *ACS Appl. Mater. Interfaces* **2019**, *11*, 8310.

[266] W. Greenbank, N. Djeddaoui, E. Destouesse, J. Lamminaho, M. Prete, L. Boukezzi, T. Ebel, L. Bessissa, H.-G. Rubahn, V. Turkovic, M. Madsen, *Energy Technol.* **2020**, 2000295.

[267] Y. Zhang, I. D. W. Samuel, T. Wang, D. G. Lidzey, *Adv. Sci.* **2018**, *5*, 1800434.

[268] S. A. Gevorgyan, M. Corazza, M. V. Madsen, G. Bardizza, A. Pozza, H. Müllejans, J. C. Blakesley, G. F. A. Dibb, F. A. Castro, J. F. Trigo, C. M. Guillén, J. R. Herrero, P. Morvillo, M. G. Maglione, C. Minarini, F. Roca, S. Cros, C. Seraine, C. H. Law, P. S. Tuladhar, J. R. Durrant, F. C. Krebs, *Polym. Degrad. Stab.* **2014**, *109*, 162.

[269] J. Kettle, V. Stoichkov, D. Kumar, M. Corazza, S. A. Gevorgyan, F. C. Krebs, *Sol. Energy Mater. Sol. Cells* **2017**, *167*, 53.

[270] E. A. Katz, A. Mescheloff, I. Visoly-Fisher, Y. Galagan, *Sol. Energy Mater. Sol. Cells* **2016**, *144*, 273.

[271] B. Ray, A. G. Baradwaj, M. R. Khan, B. W. Boudouris, M. A. Alam, *Proc. Natl. Acad. Sci. U. S. A.* **2015**, *112*, 11193.

[272] G. Li, R. Zhu, Y. Yang, *Nat. Photonics* **2012**, *6*, 153.

[273] M. S. Vezie, S. Few, I. Meager, G. Pieridou, B. Dörling, R. S. Ashraf, A. R. Goñi, H. Bronstein, I. McCulloch, S. C. Hayes, M. Campoy-Quiles, J. Nelson, *Nat. Mater.* **2016**, *15*, 746.

[274] A. Köhler, H. Bässler, *Electronic Processes in Organic Semiconductors*, Wiley-VCH Verlag GmbH & Co. KGaA, Weinheim, Germany, **2015**.

[275] F. C. Spano, C. Silva, *Annu. Rev. Phys. Chem.* **2014**, *65*, 477.

[276] R. A. Marcus, *J. Chem. Phys.* **1956**, *24*, 966.

[277] J. Benduhn, K. Tvingstedt, F. Piersimoni, S. Ullbrich, Y. Fan, M. Tropiano, K. A. McGarry, O. Zeika, M. K. Riede, C. J. Douglas, S. Barlow, S. R. Marder, D. Neher, D. Spoltore, K. Vandewal, *Nat. Energy* **2017**, *2*, 17053.

[278] M. Azzouzi, J. Yan, T. Kirchartz, K. Liu, J. Wang, H. Wu, J. Nelson, *Phys. Rev. X* **2018**, *8*, 31055.

[279] F. D. Eisner, M. Azzouzi, Z. Fei, X. Hou, T. D. Anthopoulos, T. J. S. Dennis, M. Heeney, J. Nelson, *J. Am. Chem. Soc.* **2019**, *141*, 6362.

[280] S. Athanasopoulos, H. Bässler, A. Köhler, *J. Phys. Chem. Lett.* **2019**, *10*, 7107.

[281] J. Nelson, J. J. Kwiatkowski, J. Kirkpatrick, J. M. Frost, *Acc. Chem. Res.* **2009**, *42*, 1768.

[282] R. C. I. MacKenzie, T. Kirchartz, G. F. A. Dibb, J. Nelson, *J. Phys. Chem. C* **2011**, *115*, 9806.

[283] B. Xiao, P. Calado, R. C. I. MacKenzie, T. Kirchartz, J. Yan, J. Nelson, *Phys. Rev. Appl.* **2020**, *14*, 024034.

[284] O. J. Sandberg, M. Nyman, R. Österbacka, *Phys. Rev. Appl.* **2014**, *1*, 024003.

[285] H. Bristow, K. J. Thorley, A. J. P. White, A. Wadsworth, M. Babics, Z. Hamid, W. Zhang, A. F. Paterson, J. Kosco, J. Panidi, T. D. Anthopoulos, I. McCulloch, *Adv. Electron. Mater.* **2019**, *5*, 1900344.

[286] Y. Q. Pan, G. Y. Sun, *ChemSusChem* **2019**, *12*, 4570.

[287] M. U. Khan, M. Khalid, M. N. Arshad, M. N. Khan, M. Usman, A. Ali, B. Saifullah, *ACS Omega* **2020**, *5*, 23039.

[288] Q. He, M. Shahid, J. Panidi, A. V. Marsh, W. Huang, M. Daboczi, J. S. Kim, Z. Fei, T. D. Anthopoulos, M. Heeney, *J. Mater. Chem. C* **2019**, *7*, 6622.

[289] Y. Liu, J. Zhao, Z. Li, C. Mu, W. Ma, H. Hu, K. Jiang, H. Lin, H. Ade, H. Yan, *Nat. Commun.* **2014**, *5*, 1.

[290] J. Yao, T. Kirchartz, M. S. Vezie, M. A. Faist, W. Gong, H. Wu, J. Troughton, T. Watson, J. Nelson, *Phys. Rev. Appl.* **2015**, *4*, 014020.

[291] J. Yuan, T. Huang, P. Cheng, Y. Zou, H. Zhang, J. L. Yang, S.-Y. Chang, Z. Zhang, W. Huang, R. Wang, D. Meng, F. Gao, Y. Yang, *Nat. Commun.* **2019**, *10*, 570.

[292] J. Yuan, Y. Zhang, L. Zhou, G. Zhang, H.-L. Yip, T.-K. Lau, X. Lu, C. Zhu, H. Peng, P. A. Johnson, M. Leclerc, Y. Cao, J. Ulanski, Y. Li, Y. Zou, *Joule* **2019**, *3*, 1140.

[293] L. Ma, S. Zhang, J. Wang, Y. Xu, J. Hou, *Chem. Commun.* **2020**, DOI 10.1039/d0cc05528j.

[294] C. J. Brabec, A. Distler, X. Du, H. J. Egelhaaf, J. Hauch, T. Heumueller, N. Li, *Adv. Energy Mater.* **2020**, 2001864.

[295] L. Lu, M. A. Kelly, W. You, L. Yu, *Nat. Photonics* **2015**, *9*, 491.

[296] S. M. Menke, N. A. Ran, G. C. Bazan, R. H. Friend, *Joule* **2018**, *2*, 25.

[297] J. Zhang, H. S. Tan, X. Guo, A. Facchetti, H. Yan, *Nat. Energy* **2018**, *3*, 720.

Figures

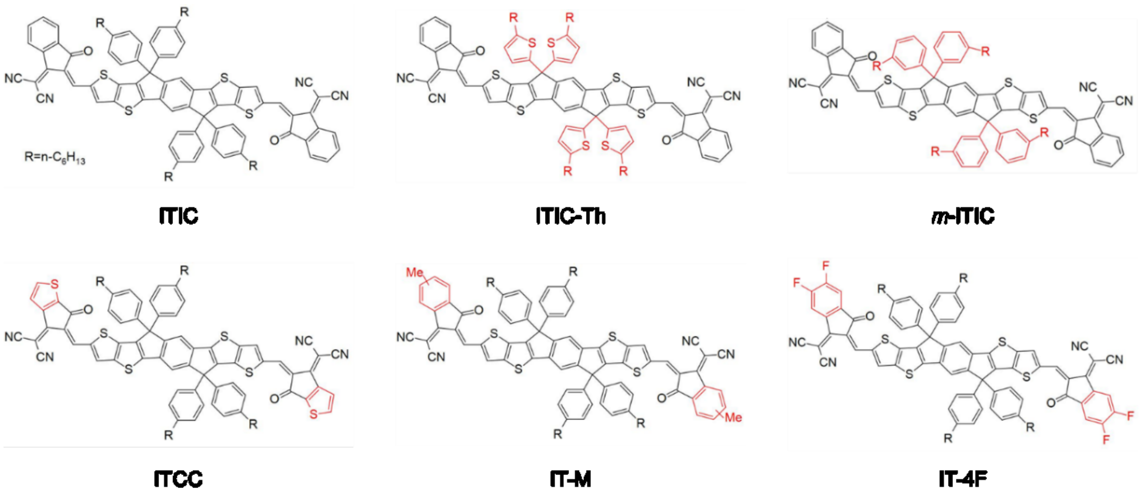

ITIC ITIC-Th *m*-ITIC

ITCC IT-M IT-4F

Figure 1. Chemical structures of ITIC-family NFA.

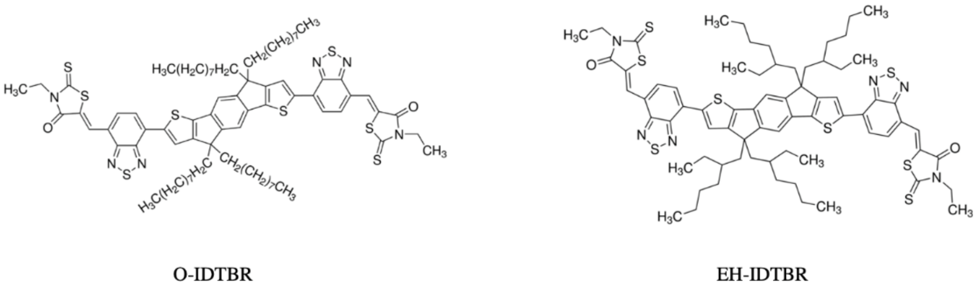

O-IDTBR EH-IDTBR

Figure 2. Chemical structures of IDTBR-family NFA (Sigma-Aldrich)

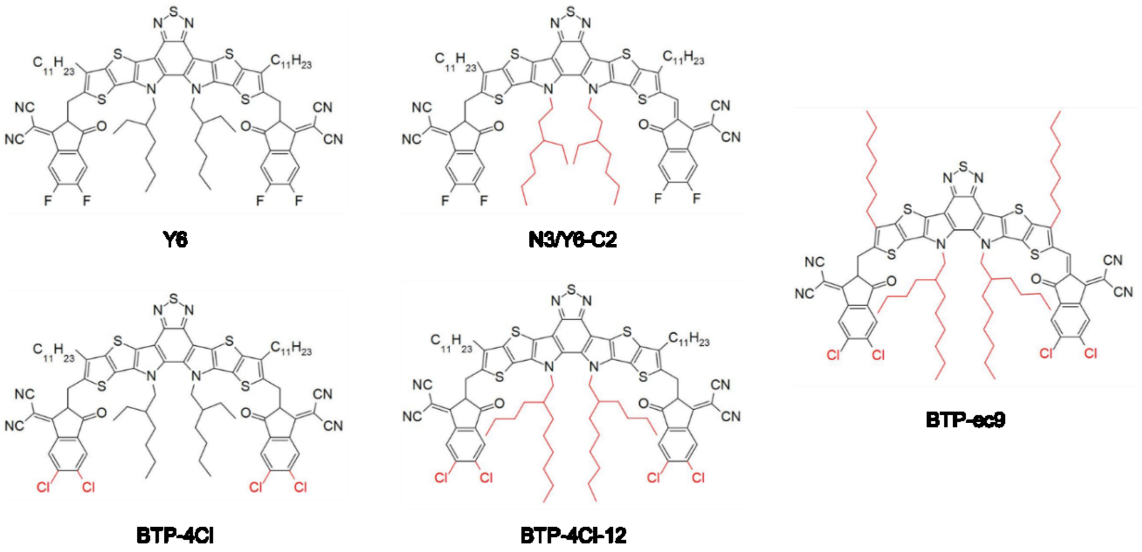
Y6

N3/Y6-C2

BTP-ec9

BTP-4Cl

BTP-4Cl-12

Figure 3. Chemical structures of Y6-family NFA.

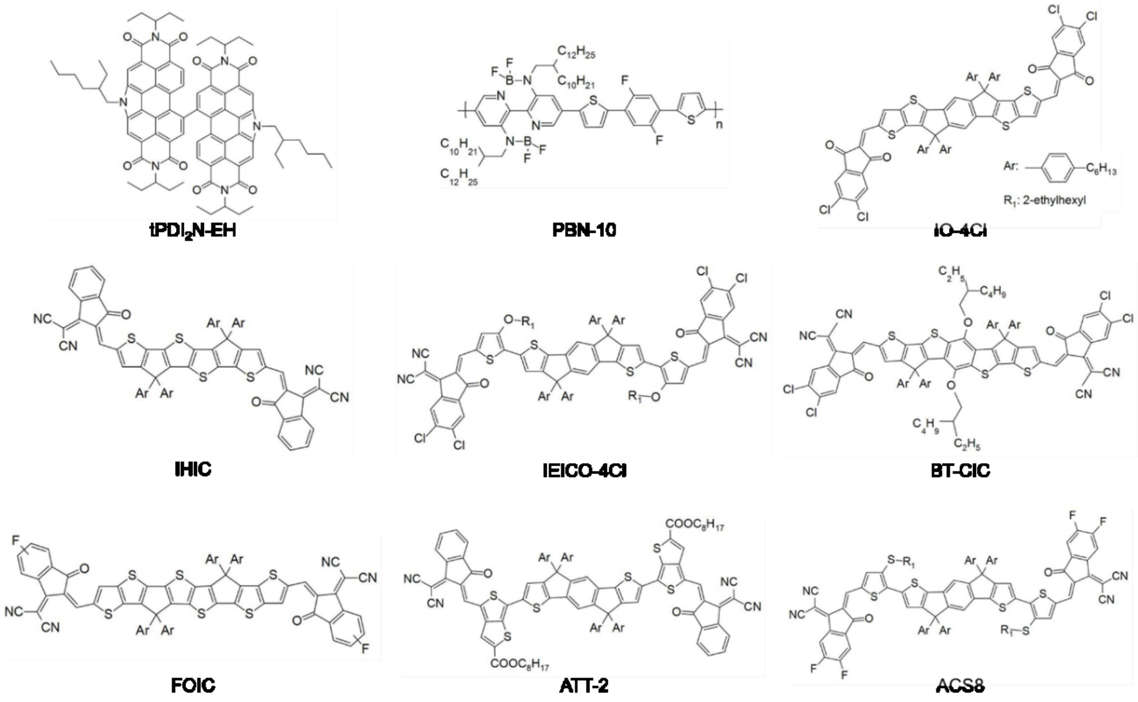
tPDI$_2$N-EH

PBN-10

IO-4Cl

IHIC

IEICO-4Cl

BT-CIC

FOIC

ATT-2

ACS8

Figure 4. Chemical structures of NFA for indoor and semitransparent applications.

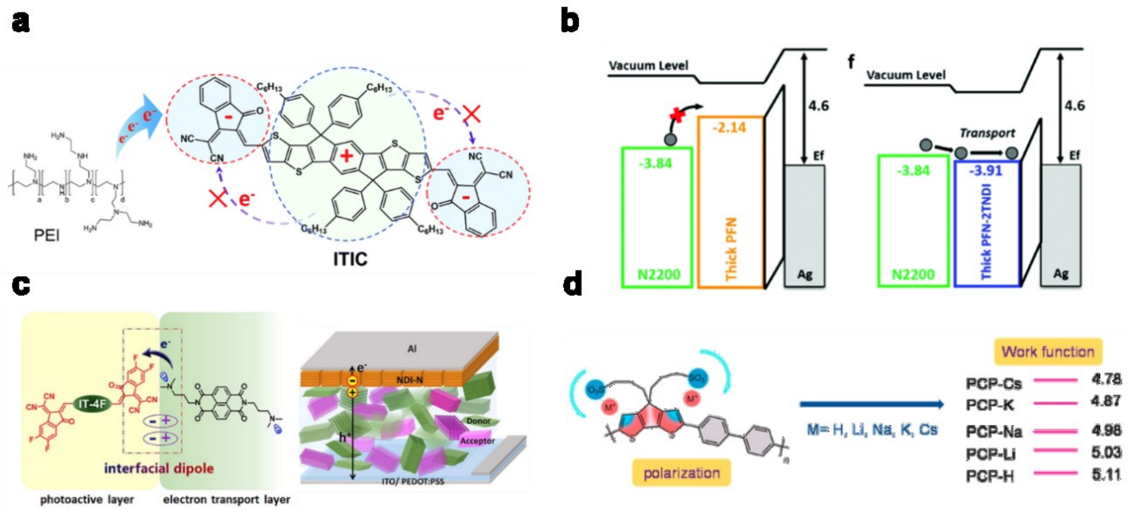

Figure 5. Polyelectrolytes for NFA OSCs. a) Schematic illustration depicting the chemical interaction between PEI and ITIC. Reproduced with permission.[67] Copyright 2018, Royal Society of Chemistry. b) Comparison of energy levels of PFN and PFN-2TNDI and their charge transport mechanisms. Reproduced with permission.[76] Copyright 2017, Royal Society of Chemistry. c) Interfacial dipole formation and exciton dissociation at the BHJ/NDI-N interface. Adapted with permission.[77] Copyright 2019, Elsevier. d) Schematic illustration representing self-doping effect. Reproduced with permission.[98] Copyright 2018, American Chemical Society.

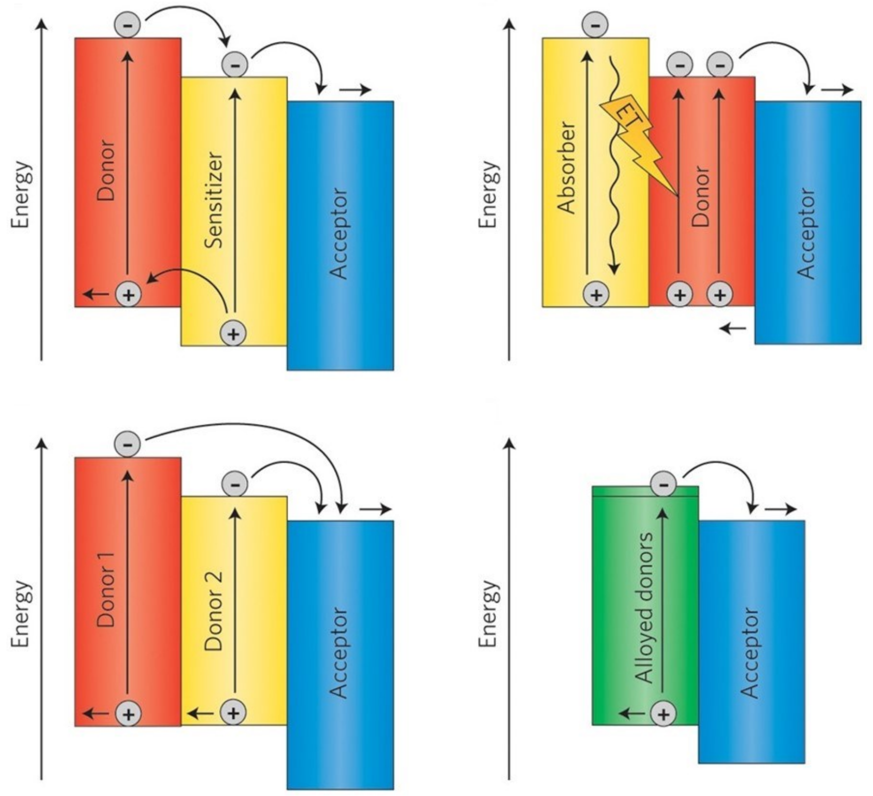

Figure 6. Operating mechanism of ternary blend OSCs: charge transfer mechanism (top left), energy transfer mechanism (top right), parallel-linkage model (bottom left), and alloy-like model (bottom right). Reproduced with permission.[295] Copyright 2015, Springer Nature.

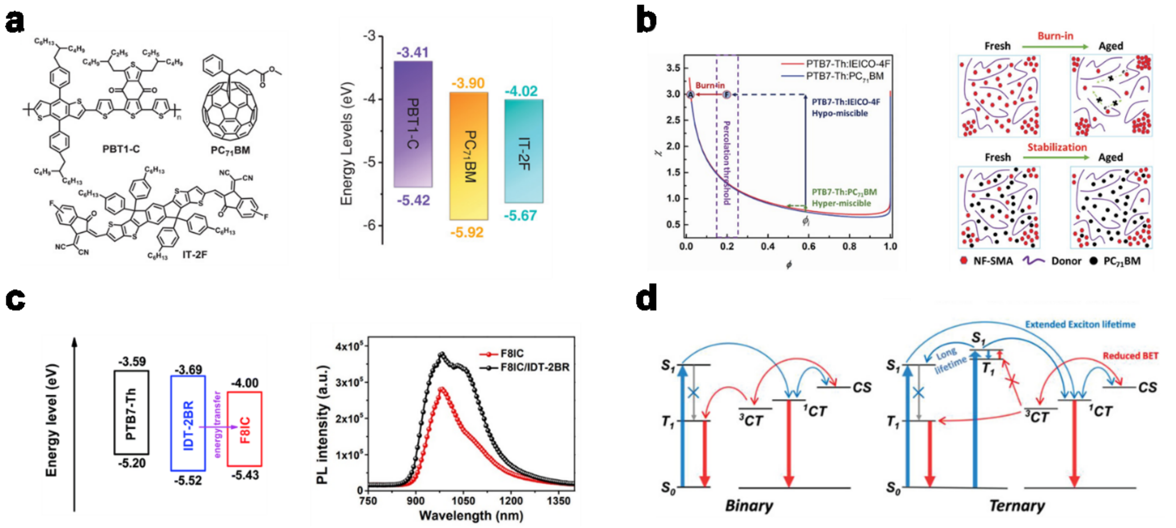

Figure 7. Ternary and quaternary OSCs. a) Chemical structures of the materials (left) and corresponding energy level diagram (right) used in ternary blend. a) Adapted with permission.[110] Copyright 2019, WILEY-VCH. b) Phase diagram for the hypomiscible and hypermiscible blends (left) and comparative schematics of morphology evolution between binary and ternary blends (right). Reproduced with permission.[112] Copyright 2019, WILEY-VCH. c) Energy transfer between two NFA in ternary blend. d) UV-vis absorption and PL spectra (left) and charge transfer mechanism in parallel-alloy quaternary blend. Adapted with permission.[104] Copyright 2018, Royal Society of Chemistry. d) Operational mechanism diagram of the ternary blend OSCs. Reproduced with permission.[105] Copyright 2020, WILEY-VCH.

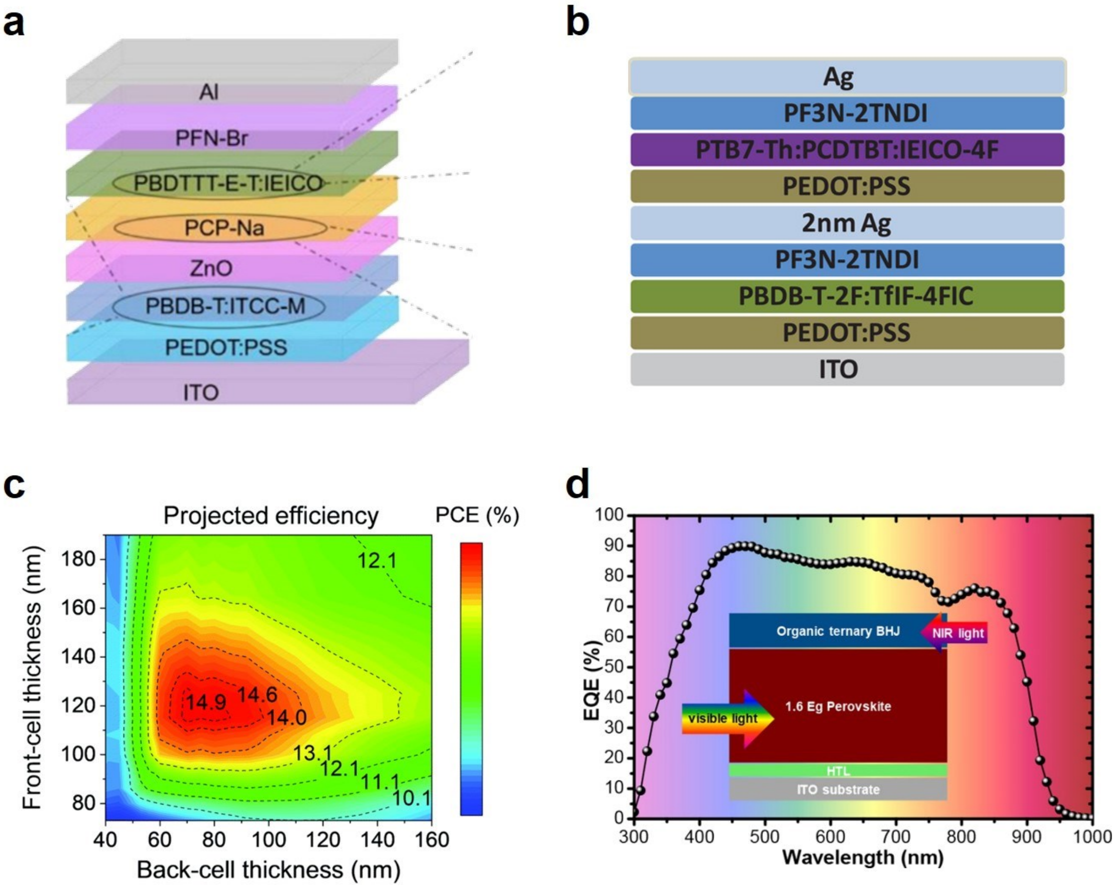

Figure 8. Tandem OSCs and perovskite/BHJ integrated solar cells. a,b) Device structure of tandem OSCs. a) Adapted with permission.[133] Copyright 2017, American Chemical Society. b) Reproduced with permission. [135] Copyright 2019, WILEY-VCH. c) Prediction of PCE of tandem OSCs based on optical-electrical modeling. Adapted with permission.[136] Copyright 2020, Royal Society of Chemistry. d) Device structure of perovskite/BHJ integrated solar cells and corresponding EQE spectrum. Reproduced with permission.[148] Copyright 2019, American Chemical Society.

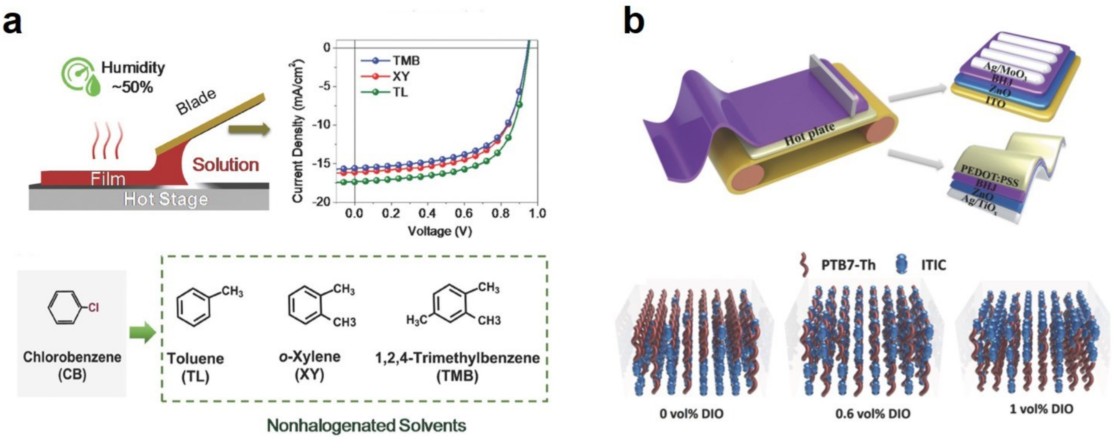

Figure 9. Printed large-area NFA OSCs. a) Effect of processing solvent on OSC performance fabricated by scalable blade-coating method. Adapted with permission.[162] Copyright 2018, WILEY-VCH. b) Effect of processing additive on the morphology of printed BHJ film. Adapted with permission.[163] Copyright 2018, WILEY-VCH.

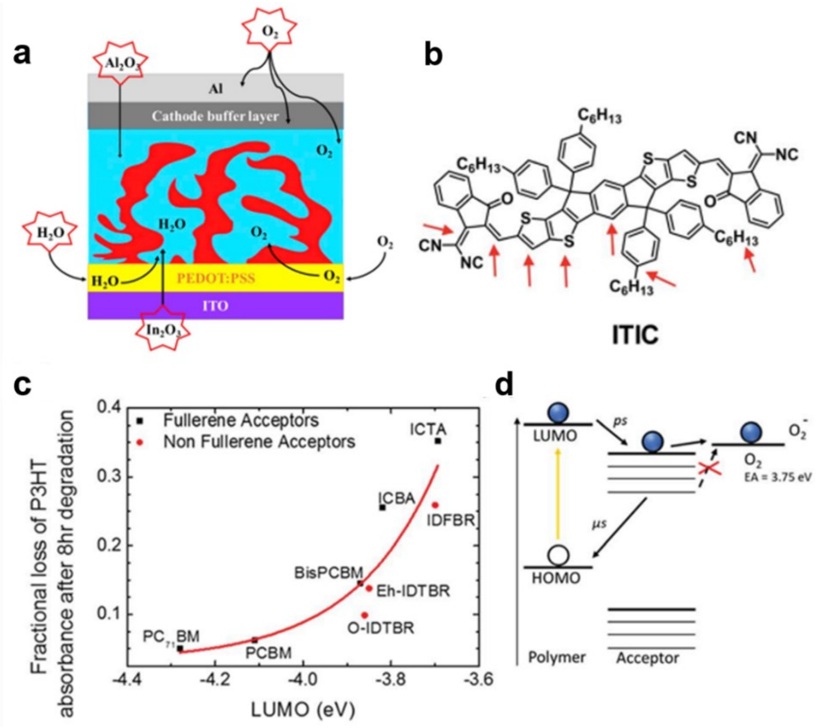

Figure 10. a) Schematic illustration of oxidative and water induced degradation pathways. Reproduced with permission.[172] Copyright 2020, Elsevier. b) Primary photooxidation reaction sites in ITIC. Adapted with permission.[175] Copyright 2019, Royal Society of Chemistry. c) Fractional losses of the P3HT absorbance peaks in blend films after 8 h of exposure under AM1.5G illumination in dry air (RH < 40%) as a function of the measured LUMO level of the acceptors, fitted with exponential growth function $y = y_0 + Ae^{((x-x0)/t)}$. d) proposed degradation mechanism, namely, the photodegradation of P3HT caused by the formation of superoxide (O_2^-) via electron transfer from the LUMO levels of the acceptors to molecular oxygen (O_2), which has an electron affinity (EA) of 3.75 eV. Reproduced with permission.[181] Copyright 2019, American Chemical Society.

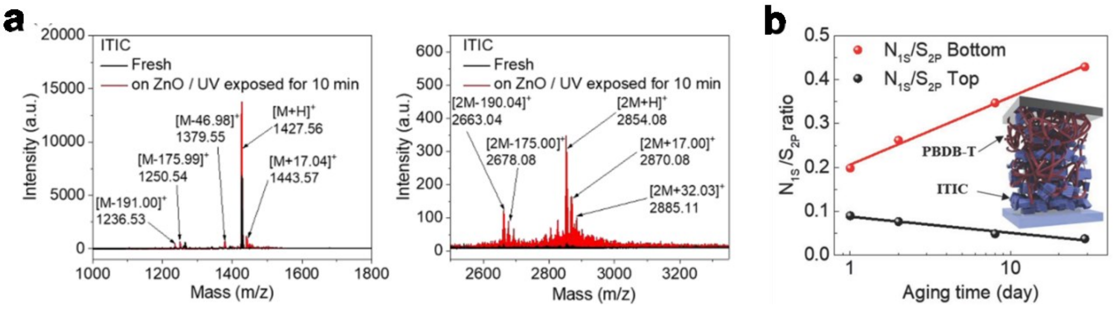

Figure 11. a) MALDI-TOF mass spectra of ITIC and 10 min UV treated ITIC on ZnO. Reproduced with permission.[192] Copyright 2019, Royal Society of Chemistry. b) The evolution of the N_{1S}/S_{2P} ratios, obtained for the bottom and top surfaces of the PBDB-T:ITIC blend layer, as function of the aging time. Inset illustrates the presence of a PBDB-T-rich upper surface and an ITIC-rich bottom surface in the binary blend PBDB-T:ITIC layer. Reproduced with permission.[68] Copyright 2019, WILEY-VCH.

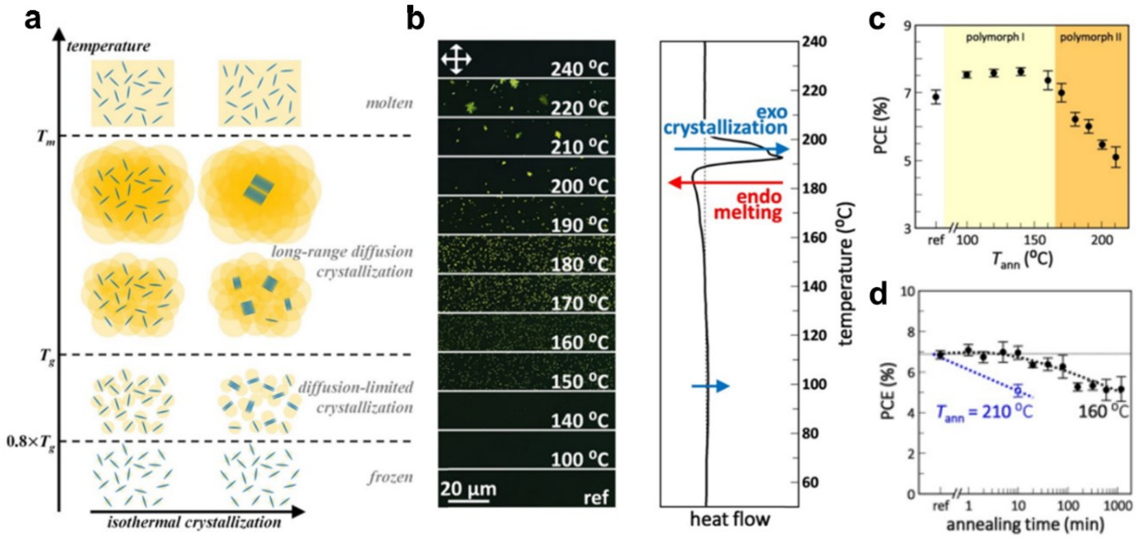

Figure 12. a) Schematic illustrating isothermal crystallization of ITIC molecules (blue) within a matrix at various temperatures, with concentric yellow circles illustrating the accessible volume. b) Polarized optical microscopy images and DSC heating thermogram of PBDB-T:ITIC blend annealed at 100 to 240 °C for 10 min. c) PCE of the PBDB-T:ITIC solar cells with active layers annealed for 10 min at temperatures up to 210 °C. d) PCE evolution with annealing time at 160 °C or 210 °C for the PBDB-T:ITIC solar cells. Adapted with permission.[196] Copyright 2019, American Chemical Society.

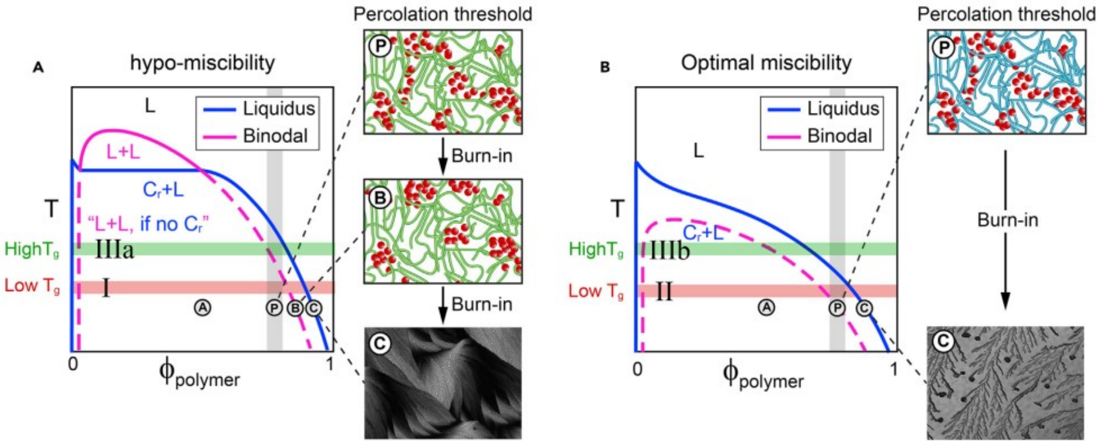

Figure 13. Motivational illustrations of the phase diagrams and schematic and observed morphologies of an upper critical solution temperature polymer:NFA Blend. Adapted with permission.[197] Copyright 2019, Elsevier.

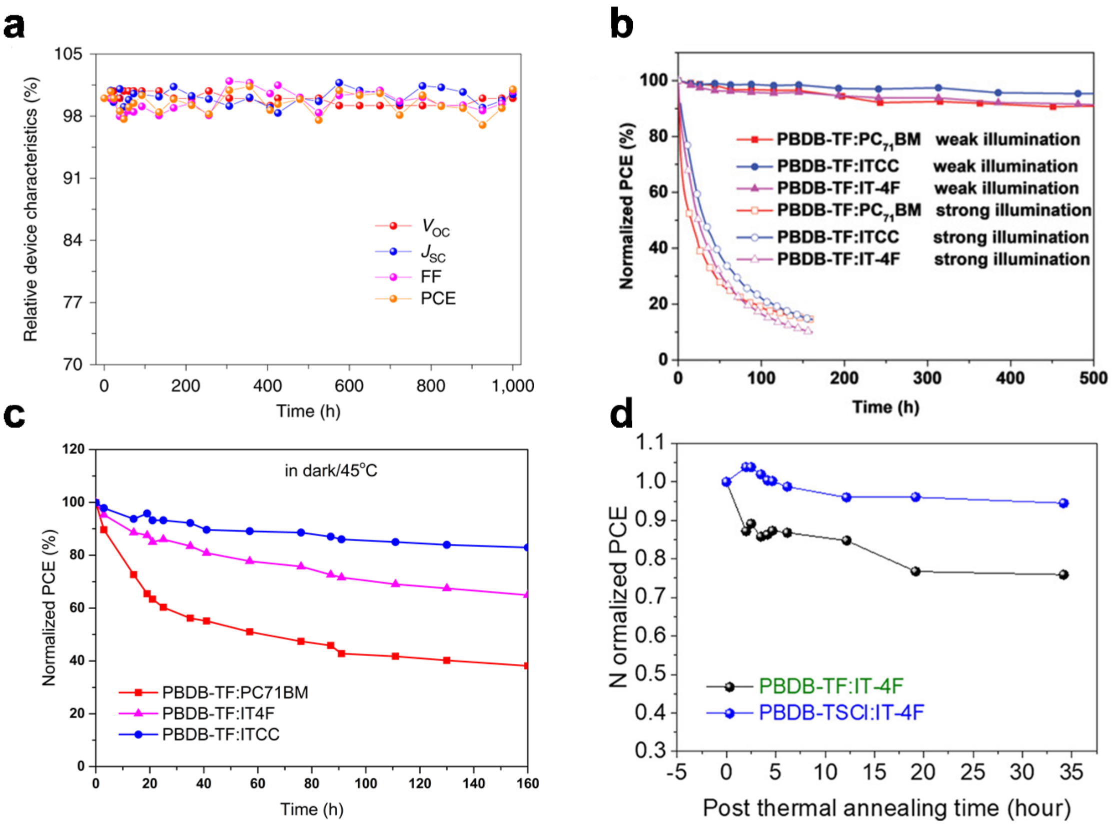

Figure 14. a) Photovoltaic characteristics of encapsulated PM6:IO-4Cl organic photovoltaics as a function of time under continuous indoor light illumination. Reproduced with permission.[11] Copyright 2019, Springer Nature. b)The stability of three encapsulated organic photovoltaics under continuous weak and strong illumination,[214] and c) the thermal stability under 45ºC in dark.[214] Reproduced with permission.[214] Copyright 2019, WILEY-VCH. d) The thermal stability at 100 ºC under an inert atmosphere. Reproduced with permission.[215] Copyright 2020, American Chemical Society.

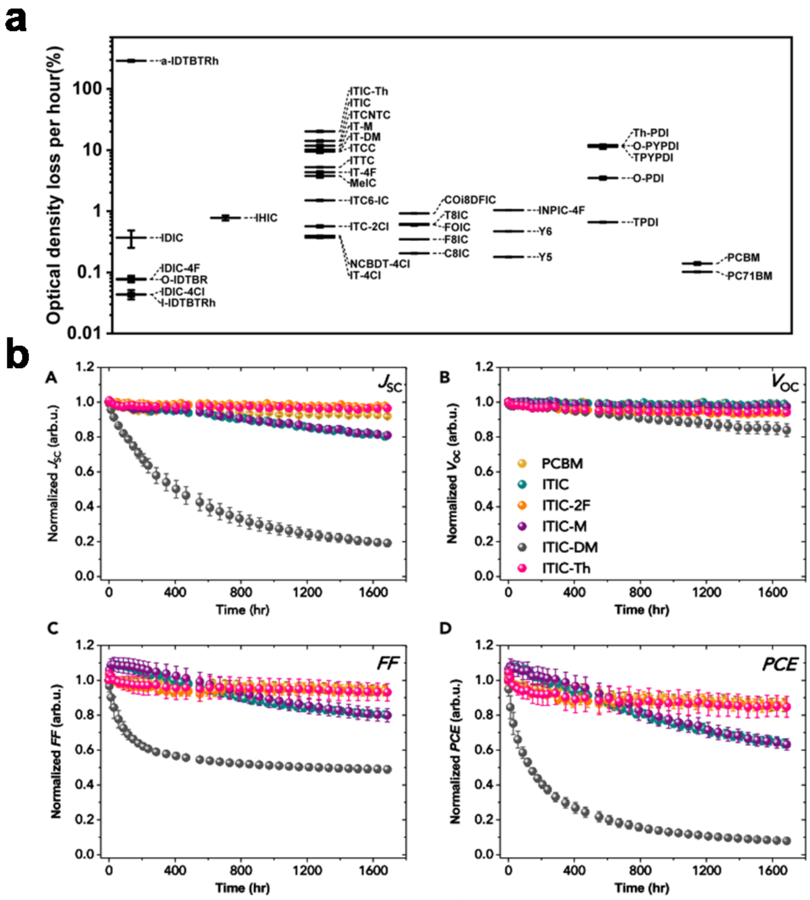

Figure 15. a) Photo-bleaching rate of acceptor materials, including nonfullerene acceptors and fullerene derivatives. Reproduced with permission.[175] Copyright 2019, Royal Society of Chemistry. b) The device stability under continuous illumination in a dry nitrogen atmosphere (A–D) J_{SC} (A), V_{OC} (B), FF (C), and PCE (D).[184] It can be seen that fluorination and thienyl side chains provide the highest stability, while dimethylation gives the shortest lifetime with strong burn-in. Adapted with permission.[184] Copyright 2019, Elsevier.

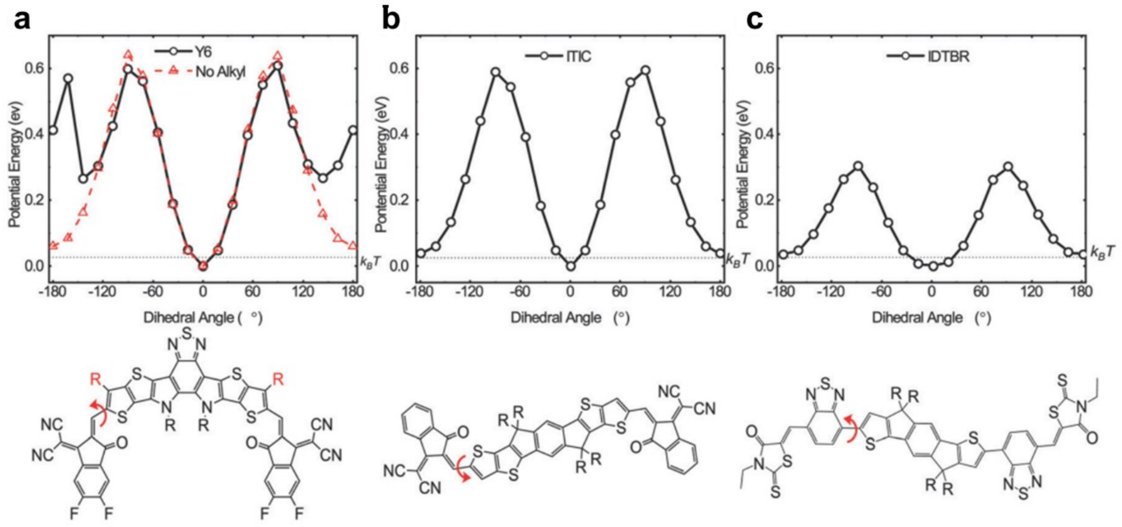

Figure 16. Potential energy scans as a function of dihedral angle (red arrow) of a) Y6, b) ITIC and c) IDTBR NFA, calculated using DFT at the B3LYP level of theory with a basis set of 6-31G(d,p). Reproduced with permission.[221] Copyright 2020, Royal Society of Chemistry.

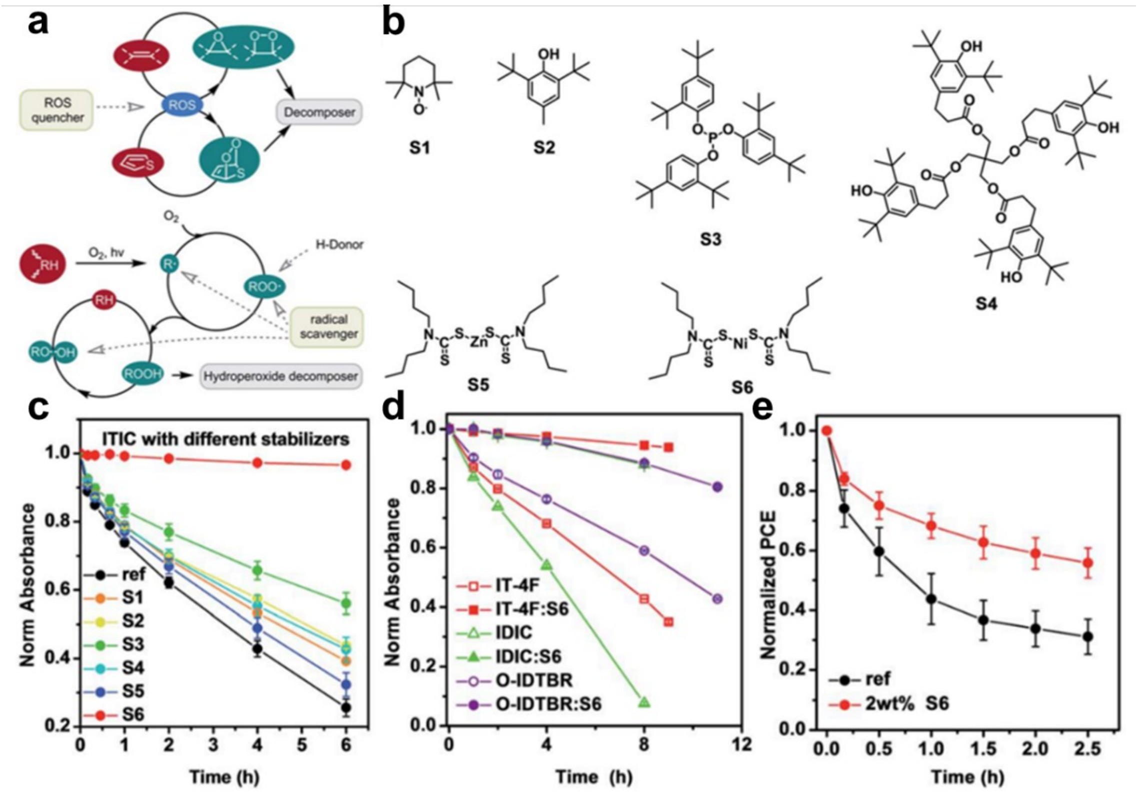

Figure 17. Suppressing photo-oxidation of NFA and their blends as well as relevant devices through stabilizers. a) Autoxidation cycle of NFA and their primary reactive sites as well as the points of attack of stabilizing additives. b) The chemical structures of several stabilizers. c) Degradation kinetics of light-soaked ITIC pristine films in air without and with the 2wt%

stabilizers. d) Degradation kinetics of NFA IDIC, IT-4F and O-IDTBR without and with 2 wt% S6 in air under illumination with a solar simulator. e) Depiction of the temporal evolution of PCE of unencapsulated devices with a device structure of ITO/ZnO/J71:ITIC/MoO_3/Ag which were continuously light soaked in dry air using a solar simulator. Reproduced with permission.[175] Copyright 2019, Royal Society of Chemistry.

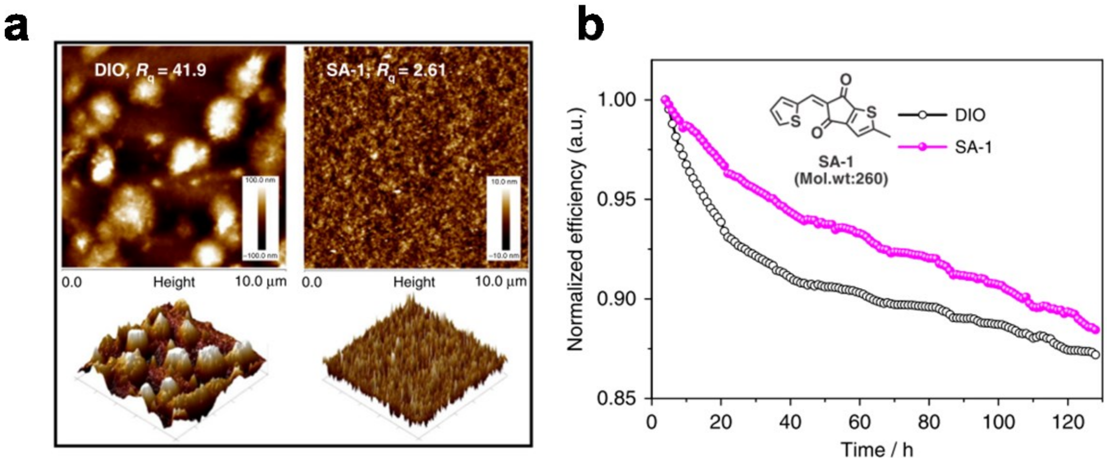

Figure 18. a) AFM height image and 3D images of PM6:IT-4F films with DIO or SA-1, for which the casted active layer was annealed after 24 h standing. The DIO processed film exhibits large aggregations with high surface roughness of 41.9 nm. The aged film with SA-1 still exhibits smooth and uniform morphology. b) Photo-stability of PM6:IT-4F-based devices with DIO or SA-1 (encapsulated in air, AM 1.5 radiation to illumination of 100 mW/cm^2 for 130 h). The inset displays the molecular structure of SA-1. Reproduced with permission.[253] Copyright 2018, Springer Nature.

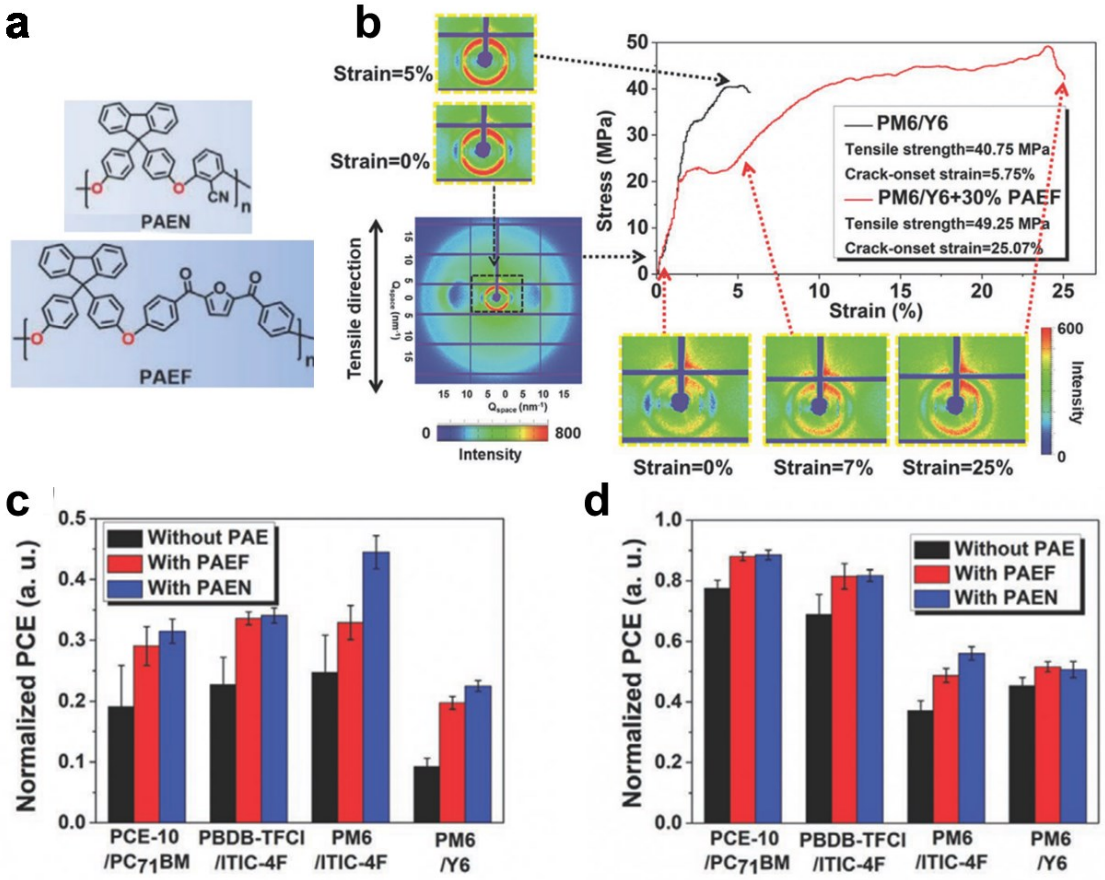

Figure 19. a) Molecular structures of PAEN and PAEF regins. b) Stress-strain curves and selected WAXS patterns during tensile deformation. c-d) Normalized PCE values of different OSCs with/without 5 wt% PAE resin after stored at 85 °C for 100 h and room temperature for 24 days in glovebox. Adapted with permission.[255] Copyright 2020, WILEY-VCH.

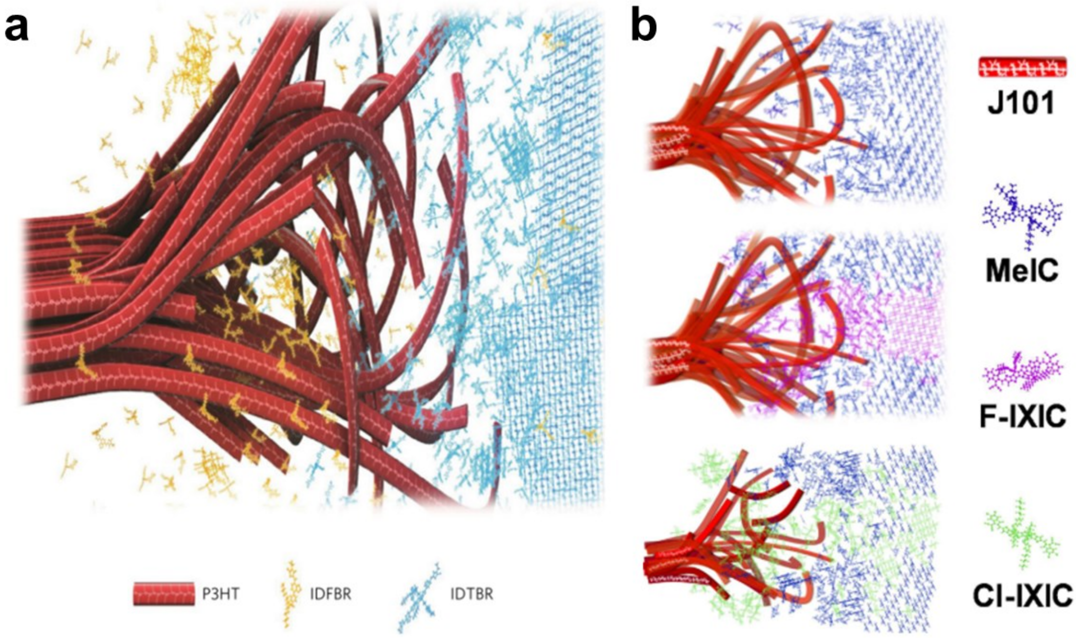

Figure 20. Morphologies of different ternary BHJs. a) P3HT:IDTBR blend with IDFBR third component forming mixed regions with both donor and acceptor as well as small-scale aggregates. Reproduced with permission.[102] Copyright 2017, Springer Nature. b) J101:MeIC morphology modified by addition of F-IXIC or Cl-IXIC acceptors. The former is able to segregate at interfaces and create pure domains, while the latter is finely intermixed in the binary host. Reproduced with permission.[259] Copyright 2020, Elsevier.

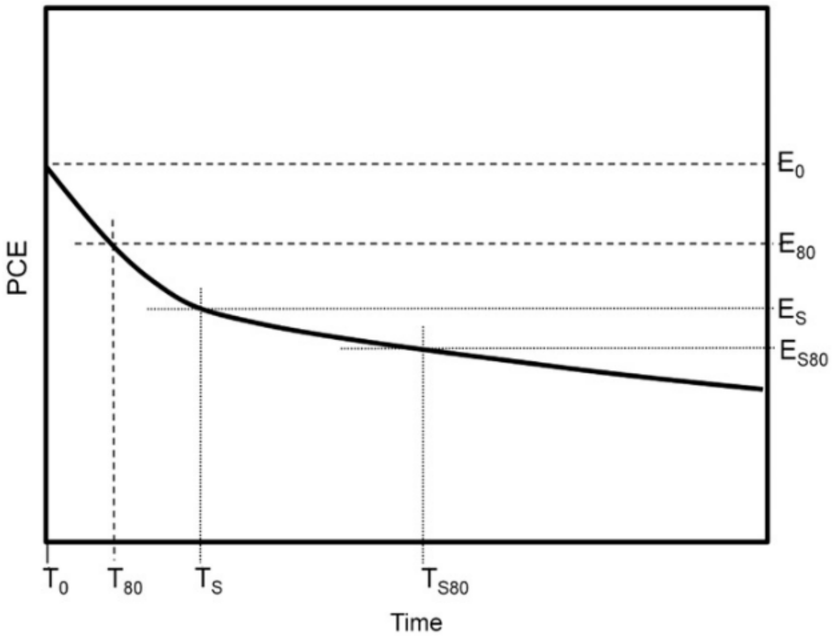

Figure 21. Schematic of the time evolution of PCE during any stability test, with the indication of the relevant times and efficiencies to report according to ISOS suggestions. Reproduced with permission.[264] Copyright 2011, Elsevier.

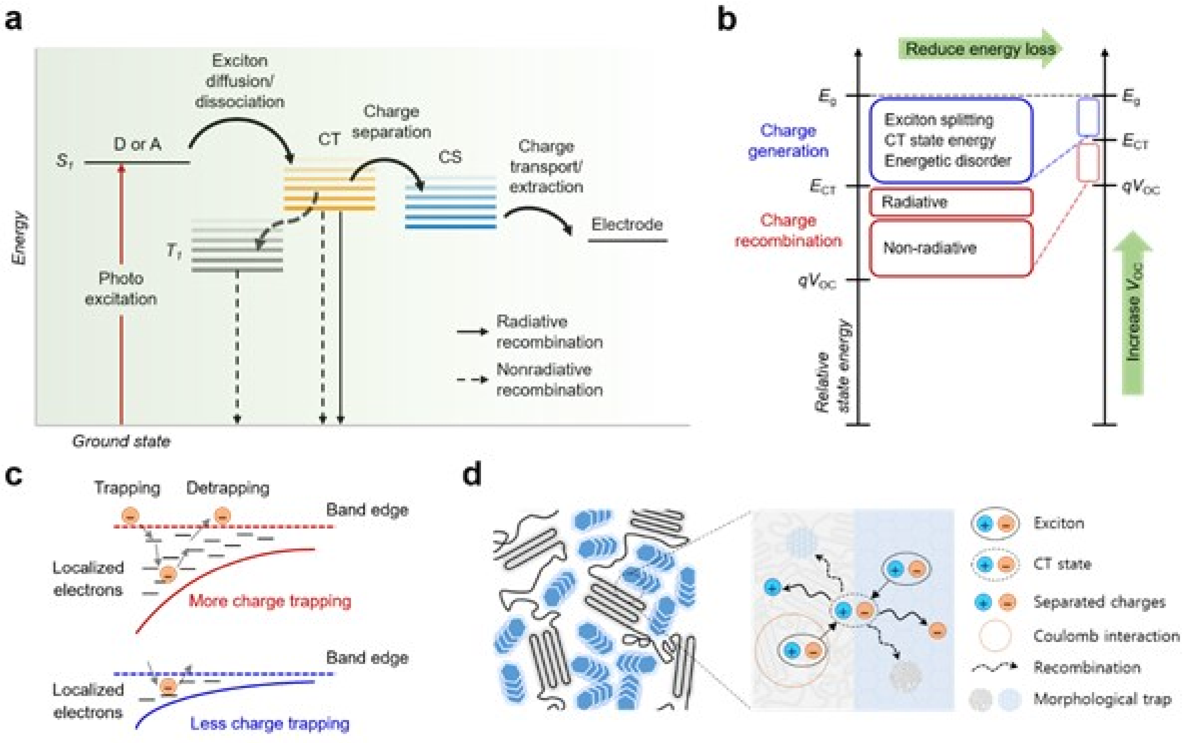

Figure 22. Photovoltaic processes in OSCs. a) Exciton and charge generation processes. b) Possible origins of energy loss and their impacts on the V_{OC}. Adapted with permission.[296] Copyright 2017, Elsevier. c) Charge trapping/detrapping processes under different trap state density and distribution conditions. Reproduced with permission.[221] Copyright 2020, Royal Society of Chemistry. d) Schematic of CT state formation and recombination.[297]

Table 1. Detailed photovoltaic parameters of OSCs based on ITIC and NFA derived from ITIC.

Blend system	PCE	J_{SC}	V_{OC}	FF
	(%)	(mA/cm^2)	(V)	(%)
PTB7-Th:ITIC	6.58	14.21	0.81	59.1
J51:ITIC	9.07	16.33	0.81	68
PDCBT:ITIC	10.05	16.50	0.94	65.57
PBDB-T:ITIC	10.68	16.73	0.90	70.8
J71:ITIC	11.2	17.40	0.94	68.09

PBDTS-TDZ:ITIC	12.8	17.78	1.10	65.4
PTB7-Th:ITIC-Th	8.5	15.95	0.80	68.0
PDBT-T1:ITIC-Th	9.3	16.17	0.88	67.1
J61:m-ITIC	11.49	18.31	0.90	69.55
PBDB-T:ITCC	11.0	15.2	1.01	71
PBDB-T:IT-M	11.48	11.48	0.94	73.5
PM6:IT-4F	13.3	20.39	0.87	75

Table 2. Detailed photovoltaic parameters of OSCs based on IDTBR NFA.

Blend system	PCE (%)	J_{SC} (mA/cm^2)	V_{OC} (V)	FF (%)
P3HT:O-IDTBR	7.1	12.91	0.73	75.09
P3HT:EH-IDTBR	6.0	12.1	0.76	62
BDT3TR:O-IDTBR	7.09	12.1	1.06	55
PffBT4T-2OD:EH-IDTBR	9.5	14.65	1.08	60
PTB7-Th:O-IDTBR	11.36	18.77	1.02	59.88

Table 3. Detailed photovoltaic parameters of OSCs based on Y6 and NFA derived from Y6.

Blend system	PCE (%)	J_{SC} (mA/cm^2)	V_{OC} (V)	FF (%)
PM6:Y6	15.6	25.3	0.83	74.8
PM6:N3	15.79	25.64	0.85	73.9
PM6:BTP-4Cl	16.1	25.2	0.87	73.7
PM6:BTP-4Cl-12	16.6	25.6	0.86	77.6
PM6:BTP-eC9	17.4	25.9	0.84	81.1
D18:Y6	17.67	27.31	0.97	75.5

Table 4. Maximum exciton generation rate (G_{max}) and exciton dissociation probability (P(E,T)) for the studied devices before and after 500 h of photoaging. Parameters of a and b in the fits ($y = ax + bx^2$) of melting point depression versus volume fraction and the Flory–Huggins interaction parameters for the PTB7-Th:ITIC, PTB7-Th:IDIC and PTB7-Th:EH-IDT blends determined by DSC measurement. Adapted with permission.[194] Copyright 2019, WILEY-VCH.

D/A	G_{max}[× 10^{21} $cm^{-3}s^{-1}$]		P (E, T)		Flory-Huggins Interaction Parameters		
	Fresh	Aged	Fresh	Aged	a [× 10^{-4}]	b [× 10^{-4}]	$\chi_{donor,acceptor}$
PTB7-Th:ITIC	9.75	9.18	90.2%	68.3%	-1.400	-2.533	1.81
PTB7-Th:IDIC	9.40	9.00	85.4%	81.6%	1.367	1.239	0.90
PTB7-Th:EH-IDT	10.22	9.91	90.2%	89.9%	0.672	0.248	0.37

Table 5. Summary of the main experimental techniques utilized for stability assessment and investigation of degradation mechanisms in OSC devices and thin films.

Technique	Probe	Probed system	Information (before/after or during degradation)
J-V scan	Electrical	Device	Evolution of photovoltaic parameters (J_{SC}, V_{OC}, FF, PCE). The dependency of $J_{ph} = J_l - J_d$ (difference between J in light and dark) on $V_{eff} = V_0 - V$ (difference between V(J_{ph}=0) and applied V) gives information on charge generation rate G
EQE	Light	Device	Changes in photon-to-electron conversion efficiency in specific spectral ranges identifies the species mostly involved in degradation by processes such as chromophore bleaching
Light intensity (I) dependent J_{SC}/V_{OC}	Electrical	Device	$J_{SC} \propto I^{\alpha}$, with α<1 indicative of bimolecular recombination; $V_{OC} \propto \log(I)$ with slope nkT/q, where n=1 is typical of ideal bimolecular recombination and n=2 indicates trap-assisted recombination. The evolution of α and n allows to study the recombination and trapping upon aging
TPV	Electrical	Device	Charge carrier lifetime dependency on V_{OC} at different illumination, in combination with CE allows to calculate recombination order (due to energetic disorder, morphological defects and traps)
Charge extraction	Electrical	Device	Charge carrier density dependency on V_{OC} at different illumination, in combination with TPV allows to calculate recombination order (due to energetic disorder, morphological defects and traps)
SCLC	Electrical	Electron/Hole-only device	Evolution of μ and μ_h/μ_e balance
Photo-CELIV	Electrical	Device	Evolution of μ and μ_h/μ_e balance, bimolecular recombination coefficient β, presence of dispersive transport
Impedance spectroscopy	Electrical	Device	Changes in resistive and capacitive behavior (series, transport, recombination resistances; chemical and dielectric capacitances). Carrier diffusivity and mobility can be extracted. Evolution upon aging reveals change in transport and recombination regimes

Electroluminescence	Electrical	Device	Evolution of emissive species allows to investigate CT states, phase separation, presence of traps
Photoluminescence	Light (laser)	Film bulk	PL evolution monitors phase separation in blends, energy transfer, molecular distortion and fragmentation
Time resolved-PL	Light (laser)	Film bulk	Evolution of carrier lifetime informs on changes in recombination mechanisms and presence of traps. Study of interfacial traps in layered samples also possible
Absorption	Light (UV-Vis)	Film bulk	Evolution of absorption properties reveals chromophore bleaching or changes in morphology such as directional rearrangement
TAS	Light	Film bulk	Evolution of excitonic/polaronic species and their lifetime, recombination mechanisms, information about traps, aggregation, morphology
Raman spectroscopy	Light (laser)	Film bulk	Changes in vibrational modes reveal evolution of molecular conformation, aggregation, charge distribution over molecule and processes like molecular distortion, conjugation loss, fragmentation and oxidation
FTIR	Light	Film bulk	Evolution of vibrational modes reveals changes in molecular conformation, morphology, conjugation and processes like oxidation and distortion
GIWAXS/GISAXS	Light (X-rays)	Film surface	Crystallinity, π-π stacking, molecular assembly, aggregation size
AFM	Tip (Van der Waals interactions)	Film surface	Changes in surface morphology and texture, nanoscale aggregation
APS/UPS	Light (UV)	Film surface	Changes in surface and interfacial energetics by oxidation, conjugation loss, distortion… Tail state density evolution related to changes in energetic disorder and trap density
CV	Electrochemical	Film bulk	Changes in energetics by oxidation, molecular distortion, conjugation loss…
MALDI-TOF/NMR	Electric/Magnetic field	Film bulk	Evolution of chemical composition, fragmentation, appearance of degradation products, chemical reactions such as oxidation
DSC/FSC	Thermal	Film bulk	State transitions (melting, crystallization, glass), changes in crystallinity, transitions between polymorphs, aggregation, phase segregation in blends

ToC Figure

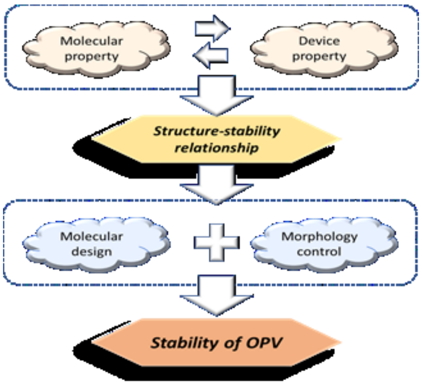

The stability of organic solar cells is an issue we need to resolve based on knowledge from both molecular and device physics to deliver a structure-stability relationship helping on molecular design, yet, the current status is far from realised. In this review, we discuss recent progresses and challenges towards stable organic solar cells.